Dipole excitations below the neutron separation threshold in neutron-rich Tin isotopes.

Zanetti, Lorenzo

(2020)

DOI (TUprints): https://doi.org/10.25534/tuprints-00013483

Publikationstyp: Ph.D. Thesis

Fachbereich: 05 Department of Physics

Quelle des Originals: https://tuprints.ulb.tu-darmstadt.de/13483

Kernreaktionen
GSI Helmholtzzentrum für
Schwerionenforschung GmbH

TECHNISCHE
UNIVERSITÄT
DARMSTADT

Physik

Dipole excitations below the neutron separation threshold in neutron-rich Tin isotopes.

Vom Fachbereich Physik
der Technischen Universität Darmstadt

zur Erlangung des Grades
eines Doktors der Naturwissenschaften (Dr. rer. nat.)

genehmigte Dissertation von
M. Sc. Lorenzo Zanetti
aus Mailand

Darmstadt 2019

D17

Dipole excitations below the neutron separation threshold in neutron-rich Tin isotopes.

Referent: Prof. Dr. Thomas Aumann
Korreferent: Prof. Dr. Joachim Enders

Tag der Einreichung: 19.11.2019
Tag der mündlichen Prüfung: 11.12.2019

Zanetti, Lorenzo: Dipole excitations below the neutron separation threshold in neutron-rich Tin isotopes.
Darmstadt, Technische Universität Darmstadt,
Year thesis published in TUprints: 2020
Date of the viva voce: 11.12.2019

To the 2^+ state of Tin-132

Abstract

Among the many ways to describe and predict the behaviour of a nucleus, we find the nuclear equation of state (EoS). This expression aims to account for the properties of nuclear matter from common run-off-the-mill nuclei, such as those found in nature, to neutron stars and nuclei far from stability synthesized in laboratories.

Around the density nuclear matter would assume if it were infinite and constituted in equal parts by neutrons and protons, the nuclear equation of state can be expanded in a Taylor series: the first terms of this series define the behaviour of the equation of state. Of particular interest is the second order term, known as the symmetry energy. Because it is not experimentally accessible, though, a direct measurement cannot be performed and other observables have to be individuated.

One of these observables is the *dipole polarizability*, indicated with α_D of the nucleus; this quantity correlates with the thickness of the neutron skin that forms around nuclei with a marked excess of neutrons and, thus, has the potential to put a constraint on the first order coefficient of symmetry energy's Taylor series expansion around the saturation density. This term is known as the "slope" and indicated with the letter L.

The dipole polarizability can be obtained by integrating the strength of the nuclear response on all energies; this integral, though, is weighted by the energy: the response at lower energies plays, proportionally, a bigger role than that at higher ones. The aim of this work is to obtain a strength distribution for a neutron-rich isotope of Tin, ^{132}Sn, and thus measure the dipole polarizability.

To accomplish this, the data acquired at the GSI facility by the R^{3}B collaboration, in Darmstadt, have been used and a novel method for profiling the strength of the dipole response of a nucleus from a noisy spectrum has been demonstrated to be promising and, furthermore, it is expected to be portable to other isotopes and experiments where a gamma array detector is used.

Zusammenfassung

Unter den zahlreichen Möglichkeiten, das Verhalten eines Atomkerns zu beschreiben und vorherzusagen, befindet sich die nukleare Zustandsgleichung (EoS). Die EoS zielt darauf ab, die Eigenschaften von Kernmaterie zu erklären, welche von gewöhnlichen Kernen, wie sie in der Natur vorkommen, bis zu Neutronensternen und Kernen, welche in Laboratorien synthetisiert werden und weit von der Stabilität entfernt sind, reichen.

Wenn bei einer bestimmten Dichte der Kernmaterie angenommen wird, dass sie unendlich wäre und zu gleichen Teilen aus Neutronen und Protonen besteht, dann kann die nukleare Zustandsgleichung in einer Taylor-Reihe erweitert werden: Die ersten Terme dieser Reihe definieren das Verhalten der Zustandsgleichung. Von besonderem Interesse ist der Term zweiter Stufe, der als Symmetrieenergie bekannt ist. Da dieser Term jedoch nicht experimentell zugänglich ist, kann keine direkte Messung durchgeführt werden und andere Observablen müssen individualisiert werden.

Eine dieser Observablen ist die Dipolpolarisierbarkeit des Kerns, angegeben mit α_D. Diese Größe korreliert mit der Dicke der Neutronenhaut, die sich um die Kerne mit einem deutlichen Überschuss an Neutronen bildet. α_D besitzt die Möglichkeit, eine Einschränkung für die Taylorreihenausdehnung des Koeffizienten erster Ordnung der Symmetrieenergie um die Sättigungsdichte zu setzen. Dieser Term wrid als “Steigung” und mit der Variablen L bezeichnet.

Die Dipolpolarisierbarkeit kann erhalten werden, indem die Stärke der Dipolantwort des Kernes auf alle Energien integriert wird. Dieses Integral wird jedoch mit der Energie gewichtet: Die Reaktion bei niedrigeren Energien spielt proportional eine größere Rolle als die bei höheren. Ziel dieser Arbeit ist es, eine Dipolstäverteilung für ein neutronenreiches Isotop von Zinn, ^{132}Sn, zu erhalten und damit die *dipole polarizability* zu messen.

Zu diesem Zweck wurden die an der GSI bei R^{3}B in Darmstadt gewonnenen Daten verwendet, um zu zeigen, dass eine neuartige Methode zur Ermittlung der Stärke der Dipolreaktion eines Kerns aus einem verrauschten Spektrum vielversprechend ist. Diese Methode kann auf andere Isotope und Experimente, bei denen ein Gamma-Array-Detektor verwendet wird, übertragen werden.

Contents

Chapter 1

Introduction

In this work, I'll attempt to extract the dipole polarizability of ^{132}Sn from its Coulomb excitation.
Because this quantity is proportional to an integral inversely weighted by the excitation energy, I will concentrate on the region from zero[1] to the (first) neutron separation threshold, S_n.

1.1 Motivation

Among the many ways to describe and predict the behaviour of a nucleus, we find the nuclear equation of state (EoS). This expression aims to account for the properties of nuclear matter from common run-off-the-mill nuclei, such as those found in nature, to neutron stars and nuclei synthesized in laboratories far from stability.
As we will see in the following, more detailed sections, the nuclear equation of state is not an observable in itself[2], but several observables have been individuated that relate to some parameters present in the equation of state.
Traditionally, the first of these observables which was considered is the neutron skin thickness: measures [KrAk04] have shown that, in neutron-rich nuclei, the excess neutrons arrange into an envelope around the balanced core. The thickness of this "skin" relates to the symmetry energy (in particular with its "slope" parameter) of the nuclear equation of state and a measurement of the first can be used to constrain the value of the last [WaCe12].
As shown by Roca-Maza et. al. [RoBr13], the neutron skin thickness is related to the (static) dipole polarizability of nuclei, multiplied by the J parameter[3].
The dipole polarizability α_D can be given as an integral on all energies of the photoabsorption cross section σ_γ, which in turn can be deduced by the Coulomb excitation cross section, and the excitation energy. This latter quantity is found at the denominator, therefore the larger contribution to the integral comes from the lower energy part of the spectrum. Hence, the interest into wading a sea of atomic background to perform the integral.

---

[1] Or, rather, as low an energy as it is made possible by our sensitivity.

[2] Yet. In the future, maybe, an experiment will be devised that can probe it directly, but in 2019 we seem to be still far from such an achievement.

[3] This parameter denotes the value the "symmetry energy" for nuclear matter at saturation density. Please see the section "L and J parameters" for more details.

1.2 Theoretical overview

1.2.1 The nuclear equation of state

The nuclear equation of state, sometimes indicated as EoS for brevity, appears in the context of the liquid droplet model, where the nucleus is pictured as an incompressible fluid constituted by the nucleons. Being understood as a fluid, thus, the concept of "equation of state" is borrowed from thermodynamics, where the state of a complex system is given in terms of a few quantities and, furthermore, a unique state is associated with an unique set of said variables.
In the context of nuclear matter, which in first approximation is assumed to be infinite[1], the nuclear equation of state expresses the binding energy of a nucleon in function of the nuclear matter density ρ and the nuclear matter (a)symmetry δ; namely $E_{binding} = E(\rho, \delta)$. The nuclear matter density is the sum of the proton and neutron density; $\rho = \rho_p + \rho_n$; from these two terms we derive the asymmetry term $\delta = (\rho_n - \rho_p)/\rho$. The dependence of the nuclear equation of state from the nuclear matter density is of great interest for all branches of nuclear physics, because it is linked to the behaviour of very diverse systems such as atomic nuclei in their ground or excited states and neutron stars [Hor01, Ste05, Lat07].

1.2.2 L and J parameters

The nuclear equation of state does not have an analytical form; thus, to study its dependence from the nuclear matter density, one may expand it in a Taylor series around $\delta = 0$ as follows:

$$E(\rho, \delta) = E(\rho, 0) + S(\rho)\delta^2 + \dots \tag{1.1}$$

This expansion, up to the second order, lacks the first order term in the asymmetry δ because of the isospin symmetry[2]. The first term is the binding energy of a nucleon in symmetric, infinite nuclear matter whereas the second term is called "symmetry energy" and represents the difference in energy between pure neutron[3] and perfectly symmetric nuclear matter[4]. This term also plays an important role in Isovector properties of the nuclei, such as the Giant Dipole Resonance [RM13].

---

[1] This simplification can reasonably hold for nucleons well inside the nucleus, whereas surface effects may happen when outer nucleons are considered.

[2] Protons and neutrons are a singlet state of the isospin, a spin-like property used to describe the nucleons; for more information, see for example [Krane87].

[3] If the first order term was omitted because of isospin symmetry, why pure "neutron" and not just "maximally asymmetric" nuclear matter matter? Because the proton is a charged particle, therefore you'd quickly have to contend with a massive, repulsive electric field if we were to consider pure proton matter, complicating the discourse.

[4] i.e. same densities for neutrons and protons.

The symmetry energy can in turn be expanded in a taylor series, given in the following equation up to the first order:

$$S(\rho) = J + \left.\frac{\partial S}{\partial \rho}\right|_{\rho_0} (\rho - \rho_0) + \dots \tag{1.2}$$

and calculated around ρ_0, known as "saturation density" [Ton86]: the density the nuclear matter would have if it occupied all the space and were symmetric, that is to say for every neutron there would be a proton.
The first component of the expanded symmetry energy is its value at saturation density: the second is usually defined as $L \equiv 3\rho_0 \frac{\partial S}{\partial \rho}$ and it is a slope term, describing the dependence of the symmetry energy from the density. At this point, the approximate expression for S becomes:

$$S(\rho) = J - L\epsilon + \dots \tag{1.3}$$

where $\epsilon = \frac{\rho_0 - \rho}{3\rho_0}$.
With this, the dependence of the equation of state from the density of infinite nuclear matter has been encapsulated in the J and L components of the symmetry energy. To probe these experimentally, we need observables that relate to these two parameters (since J and L themselves are not directly accessible in experiments).

1.2.3 Relationship with α_D, the static dipole polarizability

As Reinhard and Nazarewicz note in their paper [Rei10]:

> "Nuclei communicate with us through a great variety of observables."

One of these observables is the *neutron skin thickness*, which is the difference between the radius that encompasses the charge of the nucleus (the proton radius, r_p) and the radius that encompasses the whole nucleus –or, more precisely, the neutrons, r_n. In neutron rich nuclei, $r_n > r_p$, thus it is understood that there is a region of the nucleus, towards its outers, that is mostly populated by neutrons. This region is the neutron skin, and $\Delta r_{pn} = r_n - r_p$ is its thickness.
The neutron skin thickness can be used as a proxy for the parameter L, as discussed in the previous section. Although this relationship is model dependent and models are all but scarce in nuclear structure theory, in general a linear correlation between the prediction of L and Δr_{np} can be observed, as shown in figure 1.1.

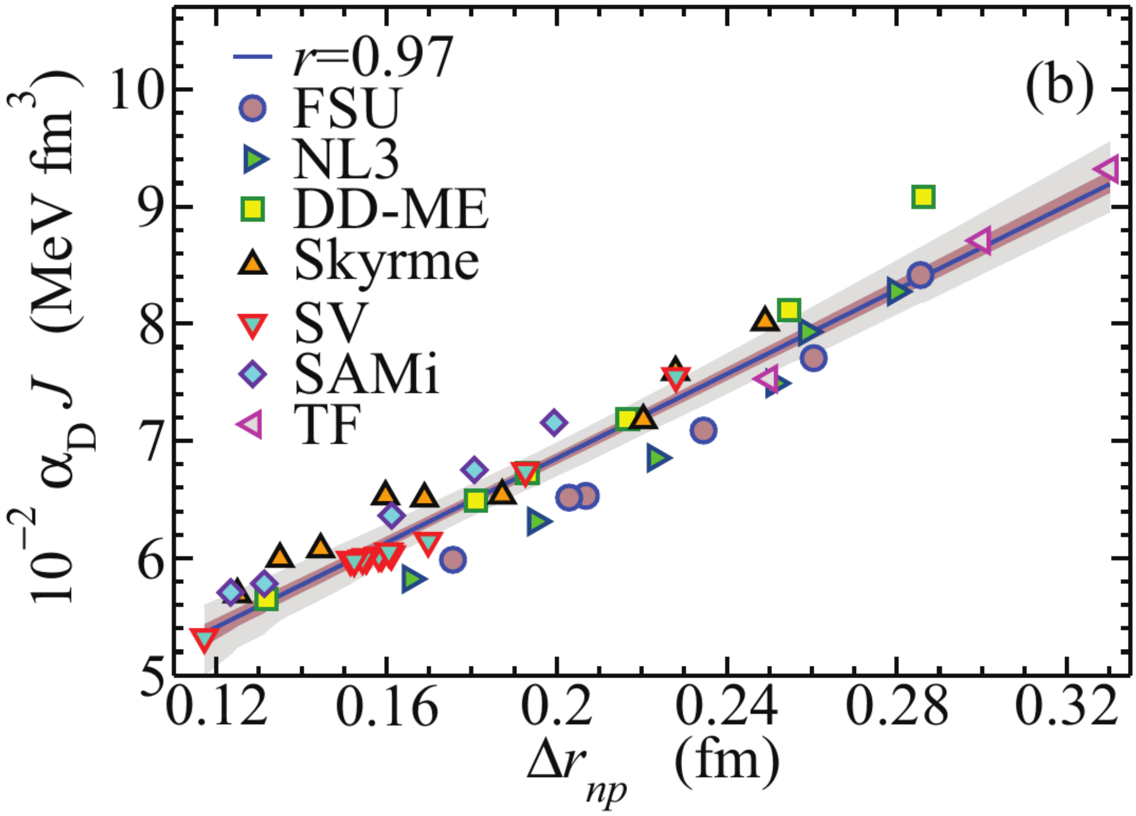

Figure 1.1: This plot illustrates the correlation between the neutron skin thickness Δr_{np} and the dipole polarizability α_D, multiplied by the symmetry energy at saturation density J, in various theoretical models. This plot is taken from [RoBr13] and illustrates the opportunity of constraining one quantity by measuring the other.

Because the neutron skin thickness is just becoming available as an observable in experiments for selected nuclei, ^{208}Pb in the case of PREX [Abr12], it becomes even more interesting to have an experimental measurement of a quantity strongly related to it, such as the *dipole polarizabilty*, denoted bt α_D.

As the aforementioned authors investigate in details[1], one way to get hold of the neutron skin thickness and thus obtain information on the symmetry energy "slope" parameter L is to measure the dipole polarizabiliy, which strongly correlate to Δr_{np}, see figure 1.2. This quantity describes how the nucleus reacts to the dipole component (E1) of an electric field which is applied to it[2], such as when a heavy ion flies by it.

---

[1] For ^{208}Pb, but the discourse on the correlation of observables applies to any nucleus, including ^{132}Sn.

[2] Also, there are two kinds of dipole polarizabilities: static and dynamic. In what follows, if not otherwise specified, I am going to talk about the *static* dipole polarizability.

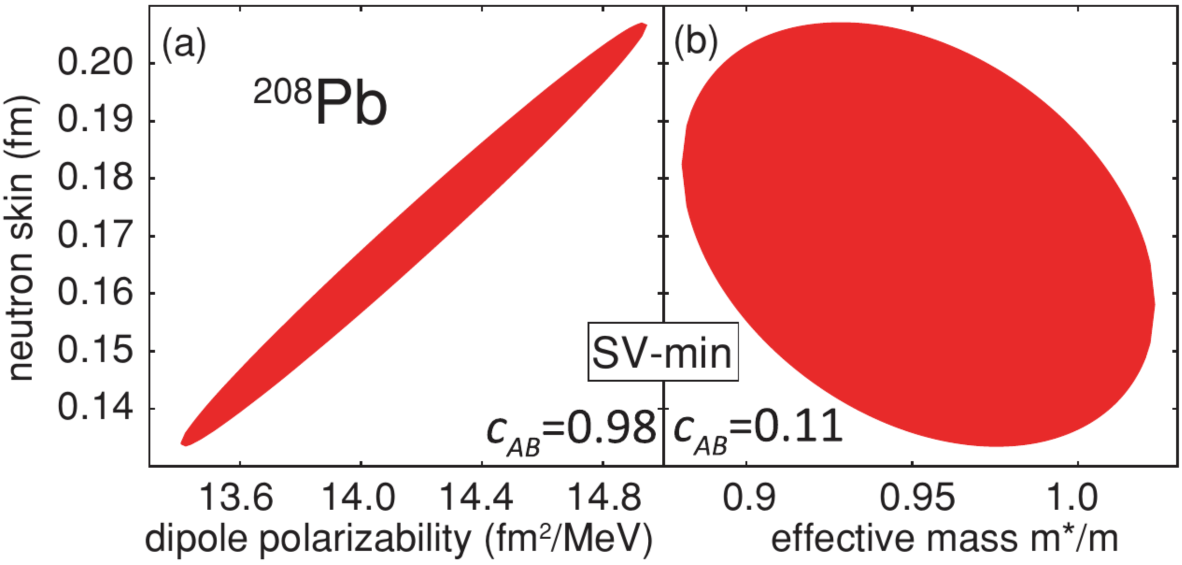

Figure 1.2: The correlation between the dipole polarizability and the neutron skin thickness in ^{208}Pb, as found in [Rei10], on the left side of the plot. On the right side the illustration that another observable is really not quite as good.

The dipole polarizability is defined as

$$\alpha_D = 2\sum_n \frac{|\langle\Phi_n|\hat{D}|\Phi_0\rangle|^2}{E_n} \tag{1.4}$$

where the index n denotes all the accessible final states, for example those calculated with the RPA approximation. With some considerable manipulation [Ber85], it is possible to obtain an expression for the dipole polarizability in function of the photo absorption cross section[1].

$$\alpha_D = \frac{\hbar c}{2\pi^2}\int_0^\infty \frac{\sigma_\gamma(E)}{E^2}dE \tag{1.5}$$

This last quantity is directly accessible for stable nuclei, provided a source of photons with the right energy range can be produced and shot at the nucleus to excite it. In case of ^{132}Sn, the nucleus is not stable and would not be at all easy to set up an experiment achieving direct excitation with photons: manufacturing a target would be impossible (and unspeakably dangerous) and in-flight excitation of fast ions has its own challenges; fortunately, an alternative technique called Coulomb excitation is available and this has been used in the S412 experiment.

1.2.4 Coulomb excitation

When two nuclei fly by each other at relativistic velocity but do not "hit" each other, i.e. when the distance of closest approach is larger than the sum of the two atomic radii, the interaction

---

[1] It's the cross section presented to photons by the nucleus.

is mediated by the electromagnetic field of the nuclei.

in what follows I am going to assume that there is one nucleus at rest, the target, and one at high speed, the projectile –not incidentally, this is also the case during the experiments performed in Cave C, where the beam impinges on a target rather than on itself like, for example, what happens in colliders such as the LHC.

Due to relativistic contraction, the projectile electromagnetic field is seen as compressed by the target along the direction of travel. This also means that, from this perspective, it can be treated as an incoming plane wave pulse [Ber85]. Most notably, this last fact allows to describe the interaction as an exchange of virtual photons. This way, the cross section and the oscillator strength for the different states can be linked with *the number of virtual photons exchanged*, which is a function of the excitation energy[1] and the masses of the two nuclei.

1.2.5 Coulomb cross section and photo absorption cross section

The key to link the photo absorption cross section with the observed Coulomb excitation cross is the virtual photon exchange mentioned in the previous section: because the passage of the projectile's electromagnetic field can be seen as a broad spectrum of photon energies illuminating the target, this gives a way to investigate the distribution of the photo absorption cross section.

The details of the derivation have been presented by Bertulani and Baur in [Ber85], but the final relationship they find is:

$$\sigma_C(E) = \sum_{\pi\lambda} N_{\pi\lambda}(E)\sigma_\gamma^{\pi\lambda}(E) \tag{1.6}$$

where π represents the *kind* of interaction, electric or magnetic, λ indicates the multipolarity order thereof (for example, 1 stands for dipolar, 2 for quadrupolar) and E is the excitation energy to be considered.

In the aforementioned paper the authors also explain a method for calculating the number of virtual photon exchanged for a given triplet of the parameters listed above: the result of their procedure will be illustrated in the Analysis chapter, when the machinery is used.

1.2.6 What about the oscillator strength?

The photo absorption cross section has a sister observable, which is the oscillator strength for a given mode, usually indicated as $B(\pi\lambda)$. This quantity expresses the transition probability

---

[1] The energy that goes to excite the nucleus which is currently examined. Usually, this is the light projectile whereas the target nucleus provides a strong EM field. If the nuclei are close in mass, though, they can excite each other.

from a state to another and, in the scope of the Coulomb excitation process, can be defined as [Ber85]:

$$B(\pi\lambda) = \frac{1}{2I_i + 1} \sum_{M_i, M_f} \| \langle I_f M_f | \, \mathcal{M} \, | I_i M_i \rangle \|^2 \tag{1.7}$$

Where $|IM\rangle$ is an eigenstate of the nucleus' Hamiltonian for electric moment I and magnetic moment M and $\mathcal{M}$ is an electromagnet multipole operator, defined in expressions 2.15a and 2.15b of [Ber85].

From the oscillator strength, it is also possible to calculate the expected Coulomb cross section and, also, it is possible to predict what the strength distribution for a nucleus, for given mode, is.

1.3 Experimental setup

The data upon which this work is based were taken in 2013 during the experiment designated with "S412" at the GSI[1], in Darmstadt. It was located in Cave C, the experimental hall dedicated to the R^{3}B collaboration and featured important detectors such as LAND, the large area neutron detector, and the Darmstadt-Heidelberg Crystal Ball; the layout is depicted in figure 1.3.

As it can be expected after the discussion in the pages before, this experiment was a Coulomb Excitation experiment: various heavy isotopes of Tin, obtained from a Uranium primary beam, were sent to a Lead target; after the reaction, all the fragment and photons coming from the nucleus were detected in order to provide full calorimetric and kinematic information about the reaction.

---

[1] The GSI acronym referred to "Gesellschaft für Schwerionenforschung", now GSI Helmholtzzentrum für Schwerionenforschung GmbH.

1.3.1 Beam

The beam was provided by GSI. A schematic drawing of the GSI facility, as it was before the FAIR[1] [FAIRweb] upgrade, can be seen in figure 1.4.

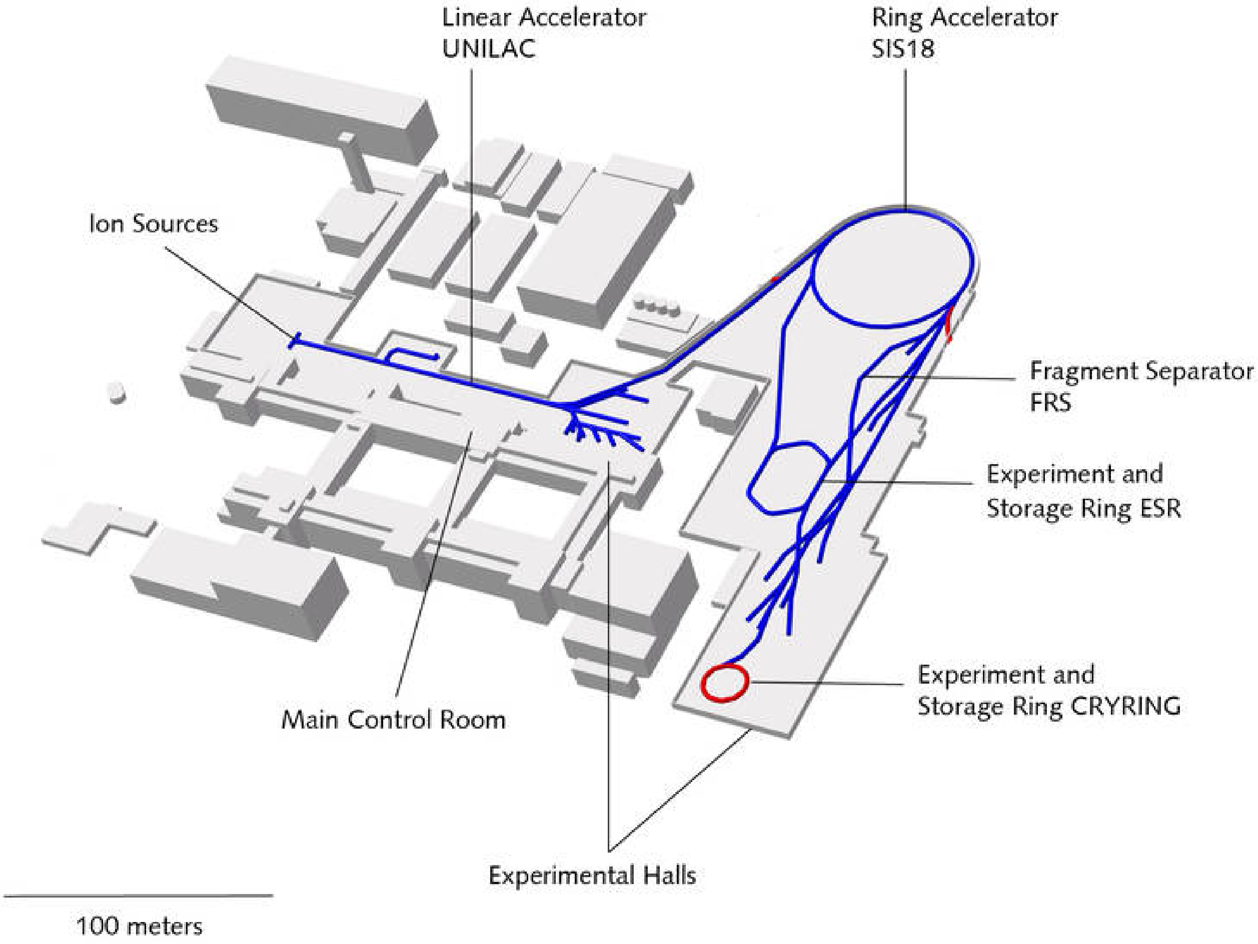

Figure 1.4: A schematics of the GSI facility. Source: the GSI website, www.gsi.de

Primary beam

The primary beam is a stable, intense beam that is sent to a target, the "primary target", where it reacts; then the products are selected according to the experimentalists' needs. At the GSI facility, the primary beam is first accelerated by Unilac, the linear accelerator fed by the ion sources, then fed into the SIS18 ring accelerator.

In the case of the experiment S412, ^{136}Xe and ^{238}U were used as primary beam and sent through a Beryllium target to produce, respectively, the lighter Tin isotopes (atomic weight from 124 to 128) and heavier ones (from 131 to 134).

---

[1] Facility for Antiproton and Ion Research in Europe.

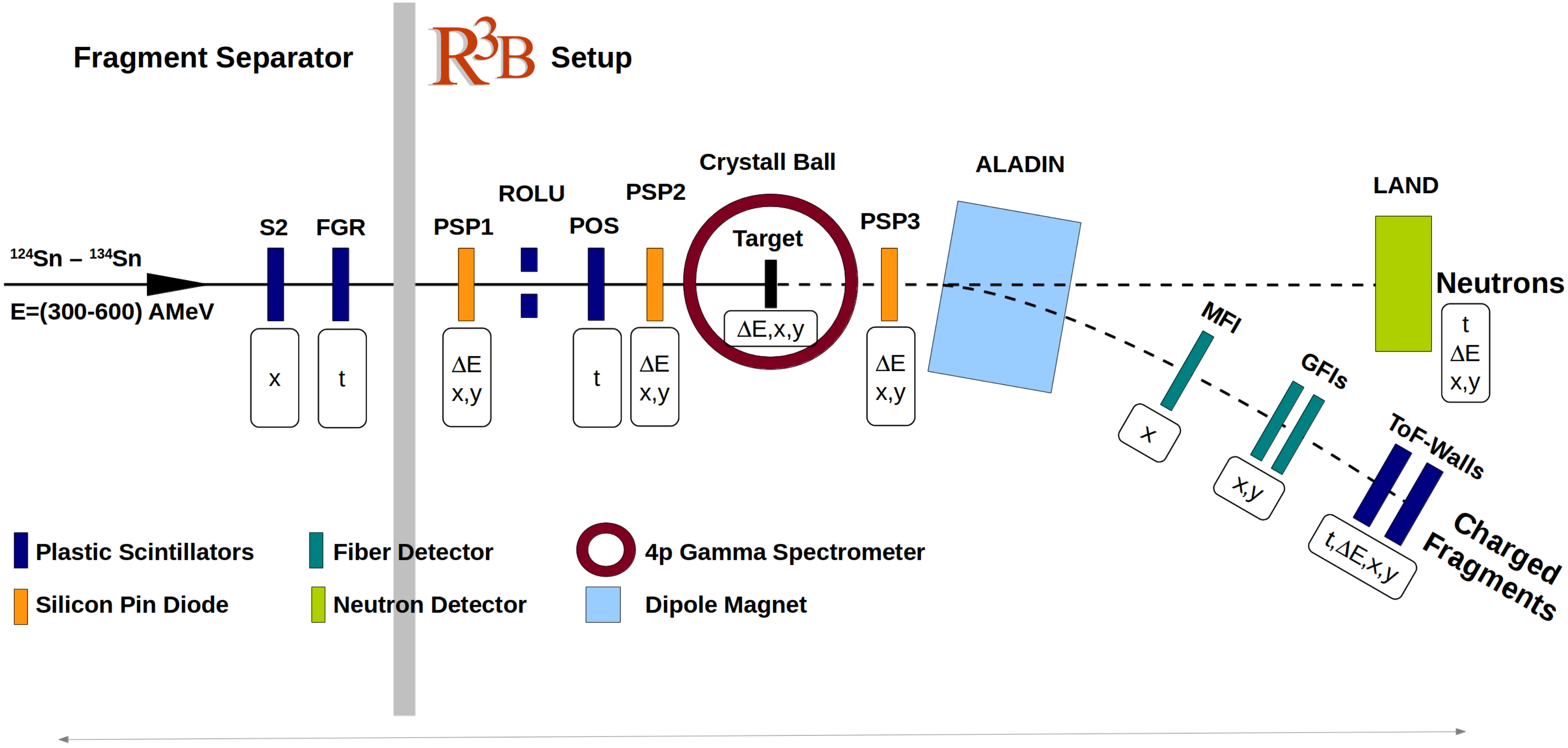

Figure 1.3: This is a schematics of the experimental setup for the S412 experiment. Credit: F. Schneider [Sch17].

Production (secondary) beam

After the production target, at which many elements and isotopes are produced, the beam passes through the fragment separator, the FRS device at the GSI, where the ion of interest is selected and sent to “Cave C”, the region dedicated to R^{3}B in the large experimental hall at GSI. In the illustration of the GSI facility seen in figure 1.4, Cave C corresponds to the last branch to the right, as seen in the figure, before the storage ring CRYRING, in red.
For an exhaustive and quantitative description of the FRS device itself and its operation, one may look up [Gei91]; qualitatively, the apparatus employs four dipole magnets to finely differentiate isotopes on their magnetic rigidity: a simplified depiction of the machine can be seen in figure 1.5. In order to do that, it relays on the different bending radius for ions with different mass-to-charge ratio with the same kinetic energy *and* the different amount of energy loss of elements with the same mass-to-charge ratio but different charges when they fly through matter –a process which depends on Z^2 and is described by the Bethe formula [Bet53].

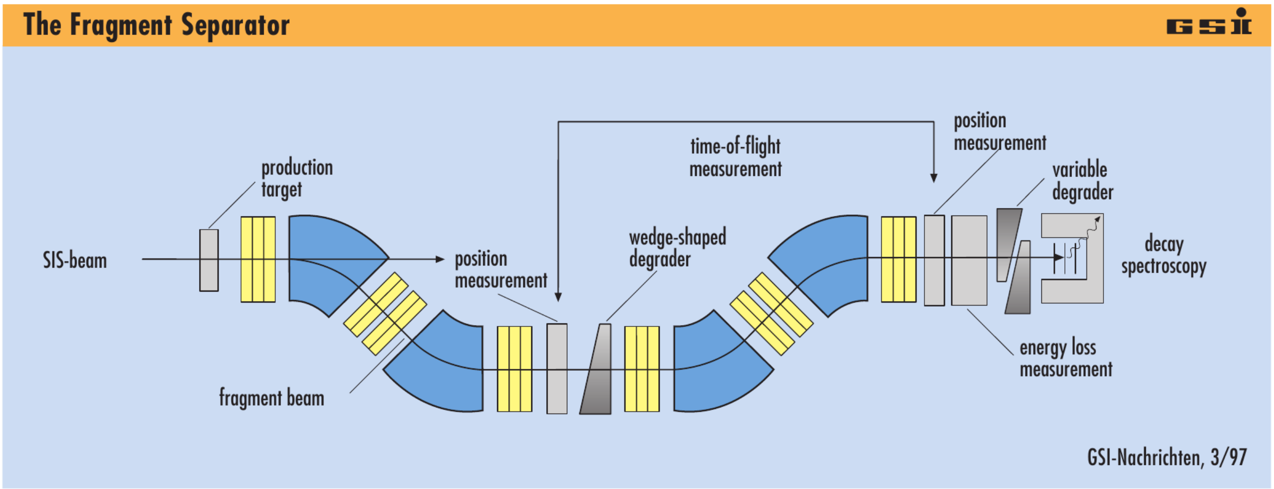

Figure 1.5: A simple depiction of the FRS. Source: [Gsi Nachrichten 97]. Although the apparatus is able to accept degraders (as labelled in the picture), during the S412 experiment none were installed; also the beam proceeded to Cave C, not to a spectroscope just after the machine.

1.3.2 Pre target tracking

The detectors positioned before the target allow to measure the momentum of the incoming ion as well as isotope identification.
This tracking solution consists of four detectors; in order:

1. PSP/Pixel one
2. ROLU

3. POS

4. PSP/Pixel two

PSPs

The PSP/Pixel detectors are silicon detectors capable of relaying the position where the ion flew through and its charge. More details about the operation and calibration of these detectors, alongside the challenges they pose, can be found in the previous doctoral theses utilizing data from the S412 experiment, such as [Sch15, Sch17, Lin18].
Qualitatively, they work as follows: when a charged particle passes through the detector a number of electron-hole pairs are created. These charge carriers can be collected by applying an electric field to the silicon slab. In order to collect the position information, four electrodes at the four corners of the active element are connected and read out: from a weighted average of these readings, the position of the interaction is calculated.

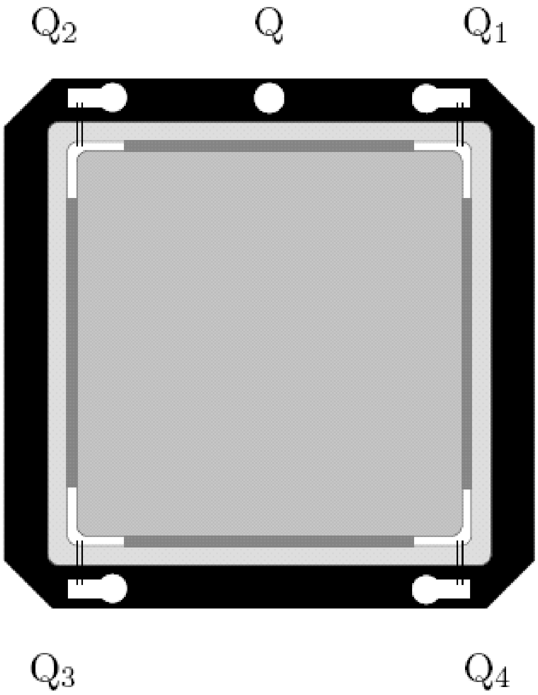

Figure 1.6: This graphic represents a PSP/Pixel Silicon detector. The letter Q's indicate the charge collection points. Q is where the total charge is read out, whereas Q_{1-4} are partial charge collection points: from the difference between the charge detected at the four corners, it is possible to locate the interaction point in the detector. Credit: internal documentation.

ROLU

The ROLU detector has a variable aperture through which the beam passes; this is defined by four scintillator paddles that can be moved and thus adjusting the (rectangular) window of the detector in the plane perpendicular to the beam axis. This detector is used as a veto and does not normally provide energy or timing information.

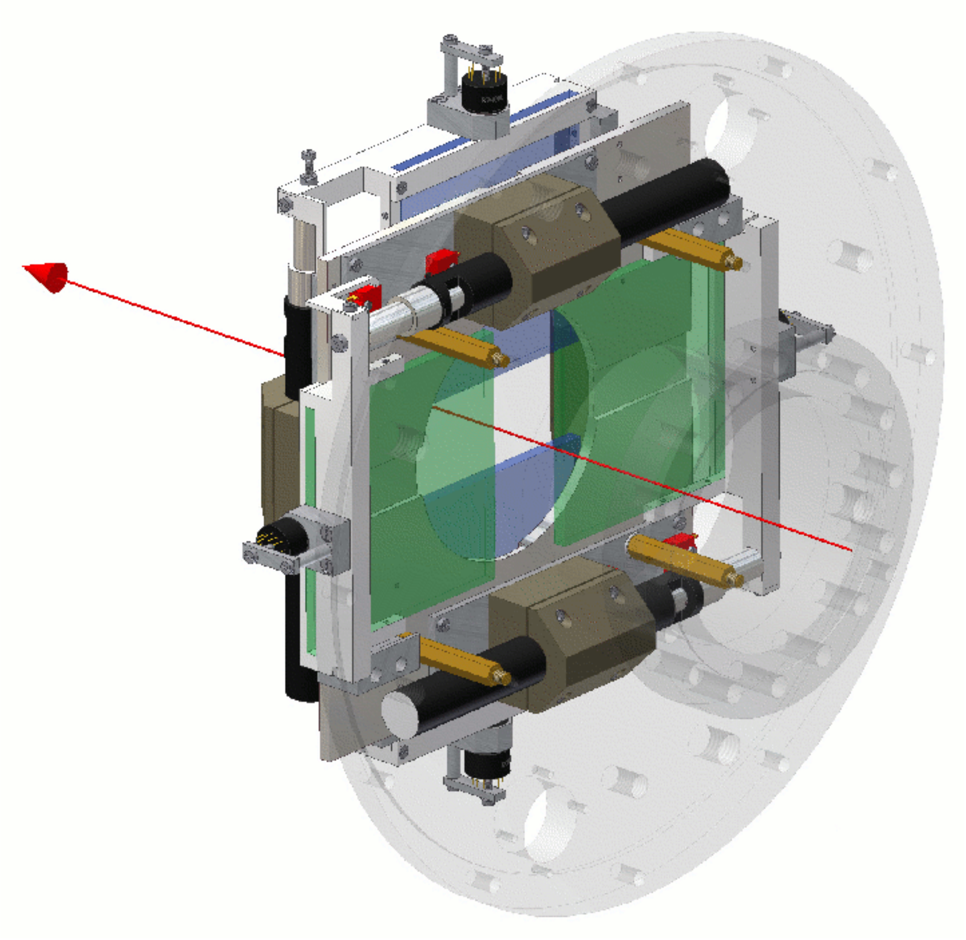

Figure 1.7: This is a CAD rendering of the ROLU detector. The red arrow is the beam axis and direction, in green and blue the scintillating panels are highlighted. The rest of the solidly colored structure is the support and drive mechanism, whereas the mounting flange is rendered as transparent, and is in front of the detector assembly. Credit: internal documentation.

POS

This detector provides crucial timing information for the time of flight measurements both in front and after the target –in the first application it is considered together with one of the scintillators present in the FRS itself to define the incoming beam momentum (and thus beta), whereas it also provides the reference for the ToF detectors after the target site.
The detector itself is a square sheet of plastic scintillator, five and a half centimetres by side,

and it is observed by four PMTs[1]. Although this arrangement would allow for positioning of the interaction point (and the name of the detector would hint to that use), in the S412 experiment this information was gathered using the silicon PSP detectors.

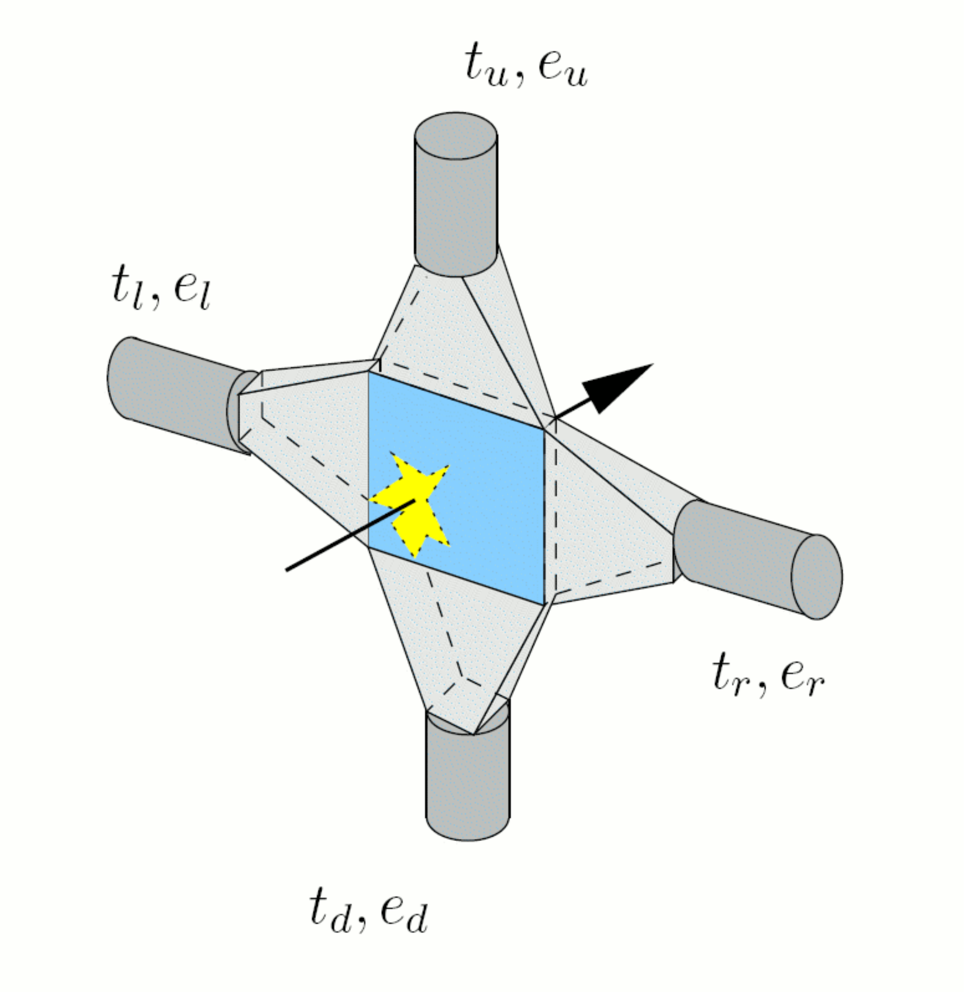

Figure 1.8: This drawing shows the structure of the POS detector: in blue at the centre of the device there's a scintillating panel, which is optically coupled to four light guides in the shape of a frustum. These collect the light from the active material and deliver it to four PMTs, which provides accurate timing information while still retaining the linearity in the response, thus also allowing an energy measurement. The detector can provide also positional information, by observing the relative intensities and the timing from the four PMTs. Credit: internal documentation.

1.3.3 The Darmstadt-Heidelberg Crystal Ball

The target is surrounded by the Darmstadt-Heidelberg Crystal Ball[2] [Met82], a 4π gamma spectrometer consisting of 162 Sodium Iodide (NaI) crystals. The crystals in this detector are

---

[1] Photomultiplier tubes.

[2] In what follows, it may be shortened to Crystal Ball, CB or XB: these all indicate the same device.

frustums, 25 cm high, arranged in a spherical shell with inner radius of 20 cm. In this cavity is located the target chamber, with the target wheel and the targets mounted on it.

Because the detector has been designed such that each crystal covers the same solid angle (around 77 msr), the bases of the frustums are of four kinds: regular pentagon and three kinds of irregular hexagons. These shapes are obtained with the following algorithm, as described by the authors in [Met82]:

> “Starting from a dodecahedron the pentagonal surfaces are divided into triangles, and the resulting triangles into even smaller ones. In contrast to the design of the plastic ball[1] the triangles are again recombined to pentagons and hexagons.”

This algorithm, in picture, can be seen in figure 1.10. More details about the design procedure can be found in a research paper about a segmented, spherical gamma array with active elements covering the same solid angle [Hab79]; this paper appears to have been the precursor of the Crystal Ball’s design. Although neither manuscript gives a mathematical proof that this procedure really leads to regions which subtend the same solid angle[2], this condition can be verified with a Monte Carlo simulation of an isotropic illumination of the Crystal Ball, which leads to the same number of counts in each crystal (within the uncertainties, that can be made small by using very large number of simulated events).

---

[1] The authors are probably referring to a then existing, smaller plastic scintillator detector.

[2] The second (earlier) one implies that this result is achieved by construction.

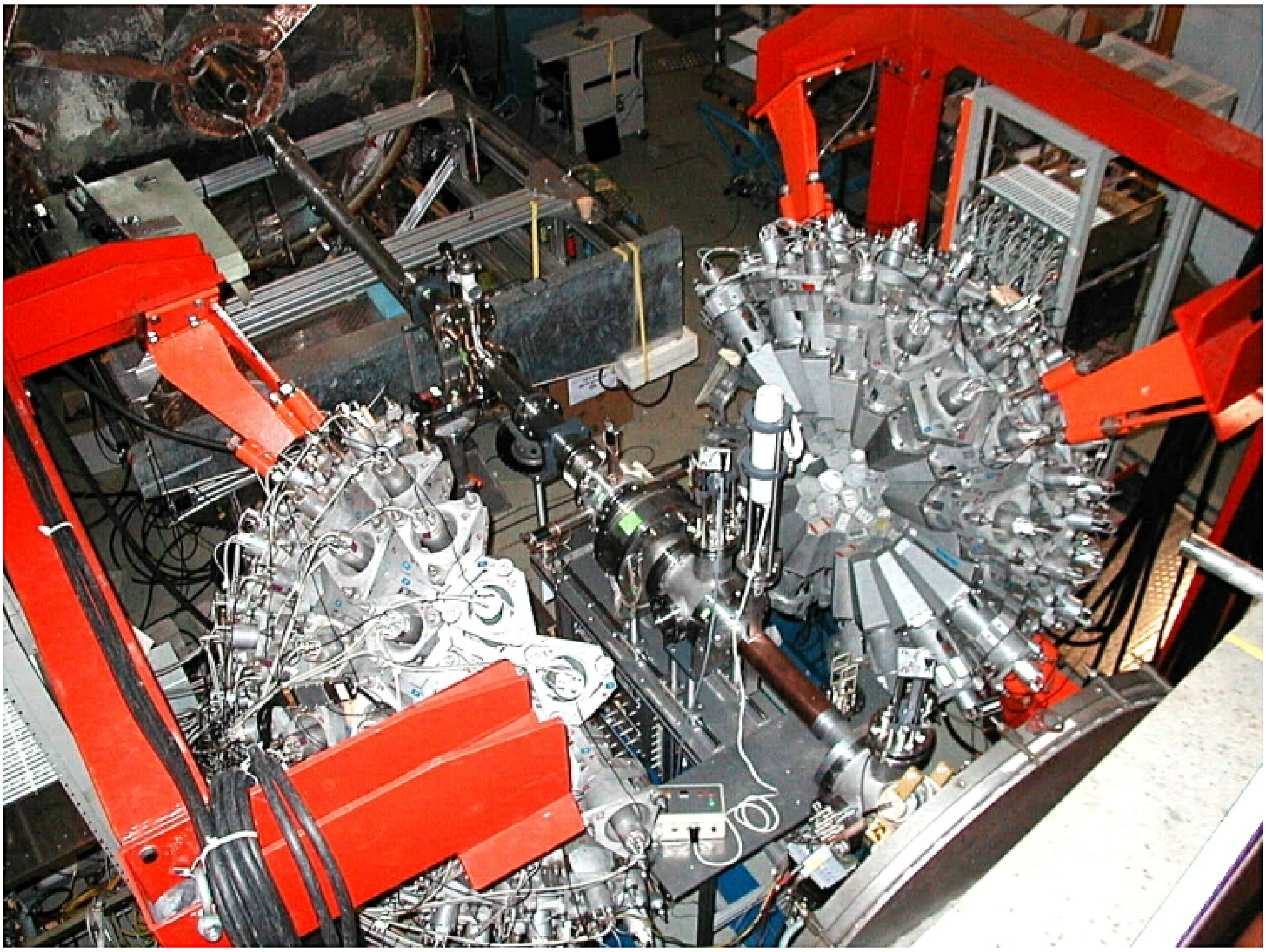

Figure 1.9: A picture of the Crystal Ball as it looked like in 2000, while open for access to the target chamber. Credit: internal documentation.

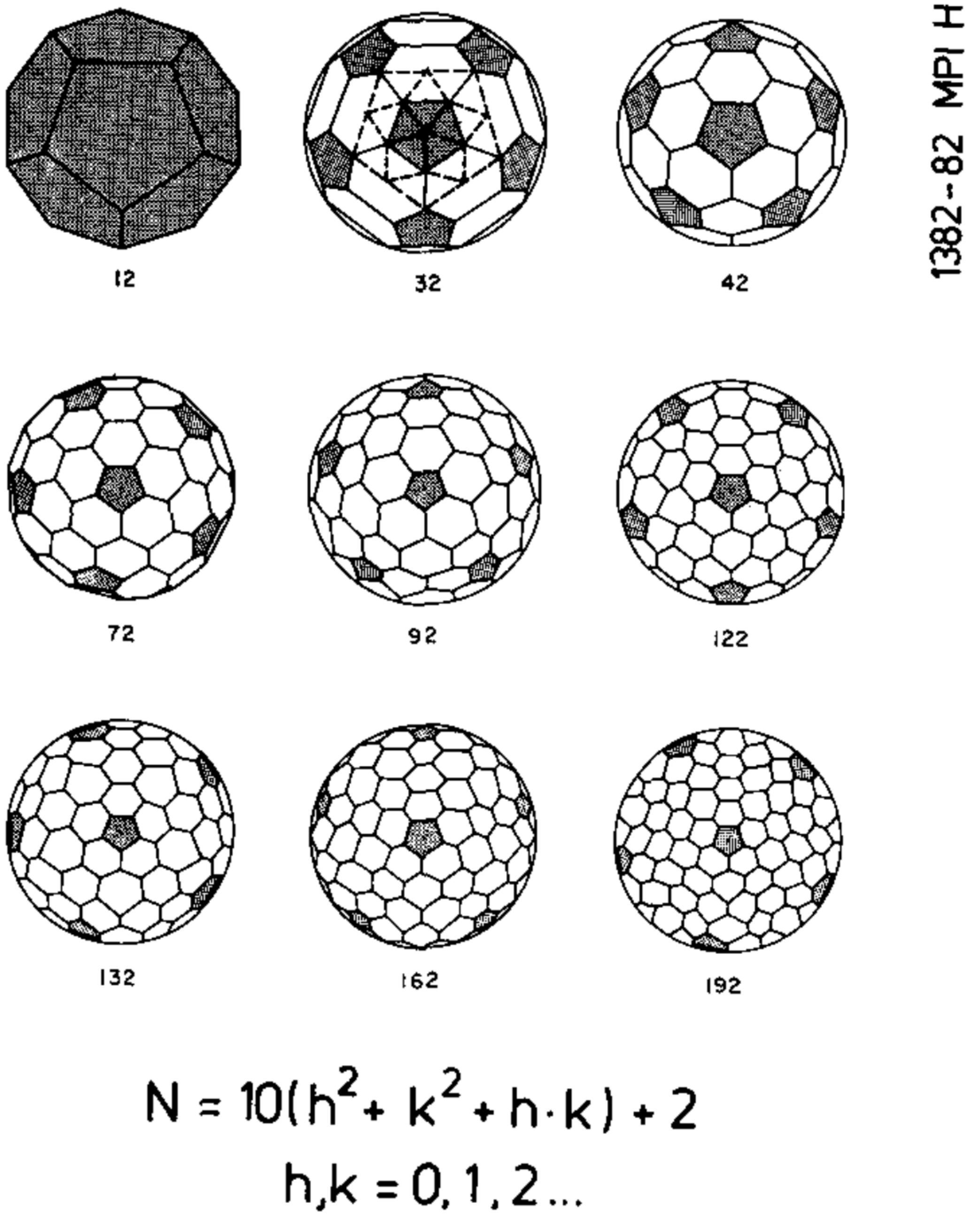

Figure 1.10: This figure, taken from [Met82], illustrates the derivation process of the Crystal Ball's segmentation. Considerable research on how these shapes can be useful and optimized for a 4π gamma array is found in [Hab79].

Verifying that the solid angle covered by each active element is equal

First of all, a large number of photons has to be produced. In theory it should not matter if they are in the same event or each in its own event; that said, in practice putting a single photon per event has the advantage of weeding out scattering processes that could be put in by GEANT[1], so I settled for a five million events simulation of photons of 200 keV. The relatively low energy should help keeping the interaction in one single crystal, otherwise it has no interest in this exercise.

Random angular distribution. Obtaining a quality (θ, ϕ) random distribution is easy, but not trivial, therefore it is not advisable to just assume that the distribution will look right even if it should given the theory.
To check that the photons were actually sent in every direction without preference, a random selection of 10^5,[2] events out of the five millions has been isolated, the momenta of the photons normalized[3], and then used to compile a three dimensional scatter plot. The expected result would be to see a sphere of unit radius appear, delineated by just points. These points should not cluster in any way, nor exhibit any salient feature whatsoever except a perceived density increase towards the “edges” of the sphere[4].
This procedure has been repeated a number of times, the result has always been like the one shown in figure 1.11.

---

[1] One could also set the software to not simulate that, but the question remains whether it is able to correctly handle one million or more primary particles. Some other technicalities can be considered, such as memory requirements, that push in favour of a many event approach.

[2] Limiting the number of events is just for technical ease: it’s faster to render fewer points.

[3] As explained a few lines above, the actual energy of the photons here is irrelevant past being low enough not to create too much Compton scattering or other processes that might interfere.

[4] It is easy to justify why this should happen. Asking an astronomer is a great way to do so.

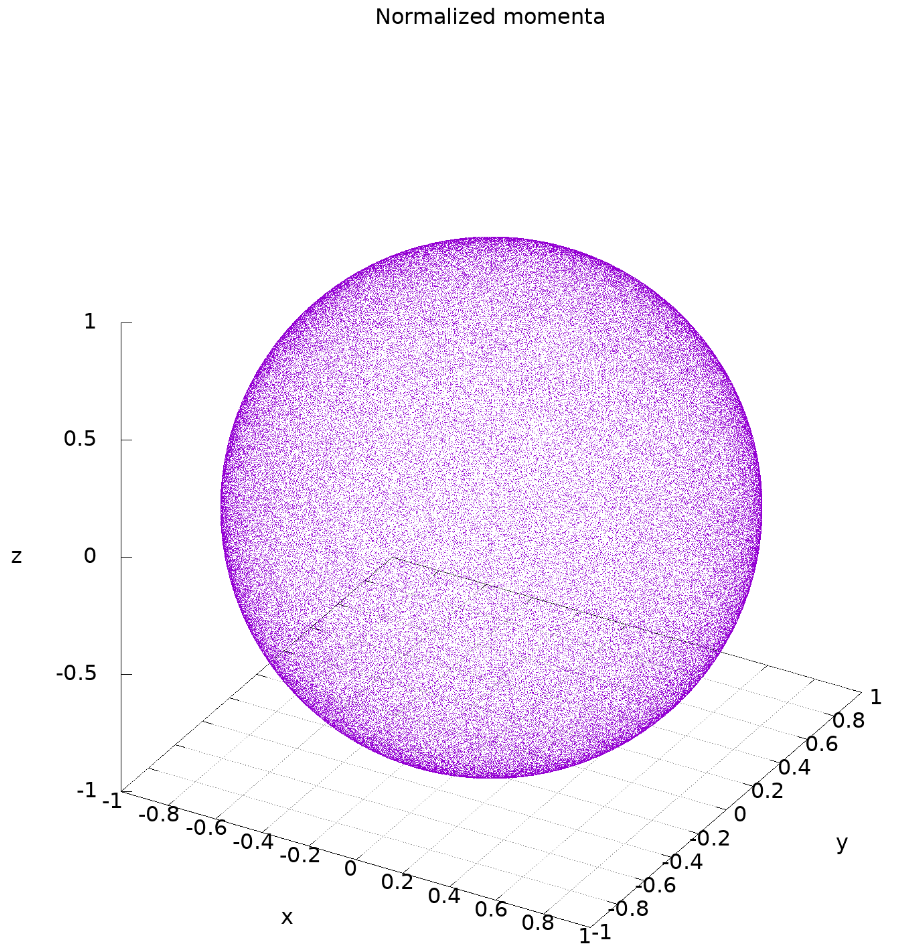

Figure 1.11: An example of a random distribution of points on a unit sphere. The points represent the three-momenta of the photons as they come out of the event generator (a GNU Octave script that I developed for this purpose). As can be seen, there are no discernible feature in the distribution of the momenta that would indicate a failure in the pseudo-randomness in the angular distribution.

Hit distribution. Once the event set has been generated and validated, it is time to feed it in the simulator program. For this simulation, clearly, taking the shielding into consideration is wrong: I deactivated it in the configuration file for this simulation; so I did for Compton scattering. After the simulation run, I selected the events that had exactly one hit in them: out of $5 \cdot 10^6$ generated, $4.6 \cdot 10^6$ complied with this condition. Also, for obvious reason, I did not apply any threshold to the crystals (nor one is implemented in the digitisation classes in R3BRoot).

Because the photons are isotropically emitted, one would expect $\frac{1}{162}$th of the full solid angle to contain $\frac{\text{\# of photons}}{162}$ on average, with an uncertainty on this quote equal to the square root of it. Because three of the 162 crystals are not counting and I am selecting on events with exactly 1 interaction in them, the denominator has to be 159 instead of 162 to obtain the correct estimate.

The resulting spectrum is in figure 1.12.

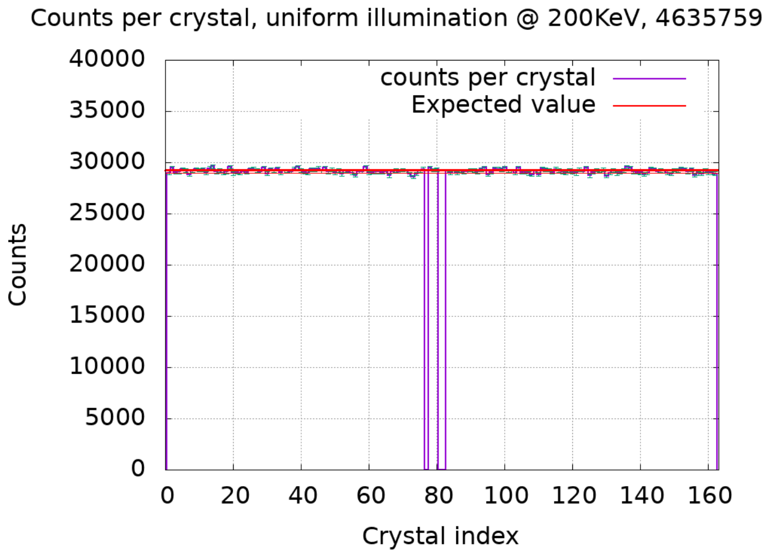

Figure 1.12: This spectrum shows the count number for every (active) crystal. As can be easily seen, the hypothesis of each of them observing the same solid angle is in good agreement with this simulation.

Granularity

A great advantage of a gamma array consisting of many detectors is the accuracy with which it can measure the angle of incidence of the photons with respect to the beam line: in fact, this angle determines how much blue or red shifted the photon is. This information is fundamental to correct the observed energy and obtain a spectrum without (too much) distortion and a decent energy resolution.

As it has been designed, the Crystal Ball offers 13 angular divisions for an elevation from 0 to π with respect to the beam direction, each of which is in the same ball park –there might be a degree or two of difference from one or the other, depending on the shape of the crystal, but this is not dominant.

Since it is not possible, from the data recorded by the DAQ[1], to obtain any more details about the photon's interaction point than in which crystal it is, each deposit is assigned the angular elevation from the beam axis that the axis of the crystal where the interaction happened has. This also means that the uncertainty on the angle of incidence vastly dominates the energy resolution of the detector for photons whose source was not at rest in the laboratory frame of

---

[1] It *might* be possible to infer the distance of the interaction point from the central axis of the crystal by observing the signal shape directly from the PMTs but, given the recording speed that could be achieved by the experiment and the amount of data from other detectors, this was not possible.

reference.

Modularity

The Crystal Ball has been designed to be highly modular: each crystal can be removed to allow, for example, a port for the beam, or supports for the target assembly. During the experiment S412, N crystals are missing:

- Crystal 81 and 82, respectively for beam out and beam in[1].
- Crystal 77 is missing to allow the support of the target chamber to reach down. This crystal is found at the bottom most position.
- Crystal 101 and 103 are also not counting[2], a possible cause for this is a beam which is rather wide on the XZ plane. These two crystals are in the immediate neighbourhood of the beam-in port (crystal 82) and, as it will be illustrated in the following, very few photons originating from the ions are expected to be found there.

These absences reduce the acceptance of the detector as it does not cover the full 4π solid angle but $(1 - \frac{N}{162})4\pi$, where N is the number of missing crystals.

Electronics and data acquisition

For each of its crystal, the Crystal Ball delivers both timing and energy information. To achieve this, the signal of each PMT is split in two and sent to the energy branch and the timing one.

The energy branch. In this branch the PMT signal, reportedly having a rise time of around 34 ns and a fall time in the order of 1 μs, is delayed by 500 ns to allow enough time for the trigger decision and then sent to a QDC[3] for acquisition. This module also performs shaping and integration of the signal.

The timing branch. The signal in this branch passes through a TFA[4] and a linear amplifier before reaching a constant fraction discriminator. This fans out a NIM signal to:

---

[1] The crystals are numbered in two spirals: one starting from the right, crystal one, and the other ending at the leftmost crystal, 162. The point of discontinuity is between crystal 81 and 82, which are of course antipodal. This provides an intuitive way to divide in two halves the Crystal Ball and relates to how it's mounted and wired up.

[2] As shown in figure 1.12, the simulator thinks these crystals are counting. This is somewhat annoying, but not a problem, because this work will concentrate on the other half of the Crystal Ball.

[3] Charge to digital converter.

[4] Timing Filter Amplifier.

- A TDC[1] behind a 500 ns delay for eventual acquisition, after the trigger decision.
- The scaler, for counting.
- The global OR and the trigger logic, which generate the gate to record the signals from the timing and the energy branch.

The TDC and the QDC are read out by the DAQ if a valid gate is generated (and the global trigger condition is met; more on this can be found in other theses about R^{3}B experiments, most notably [Jon06]).

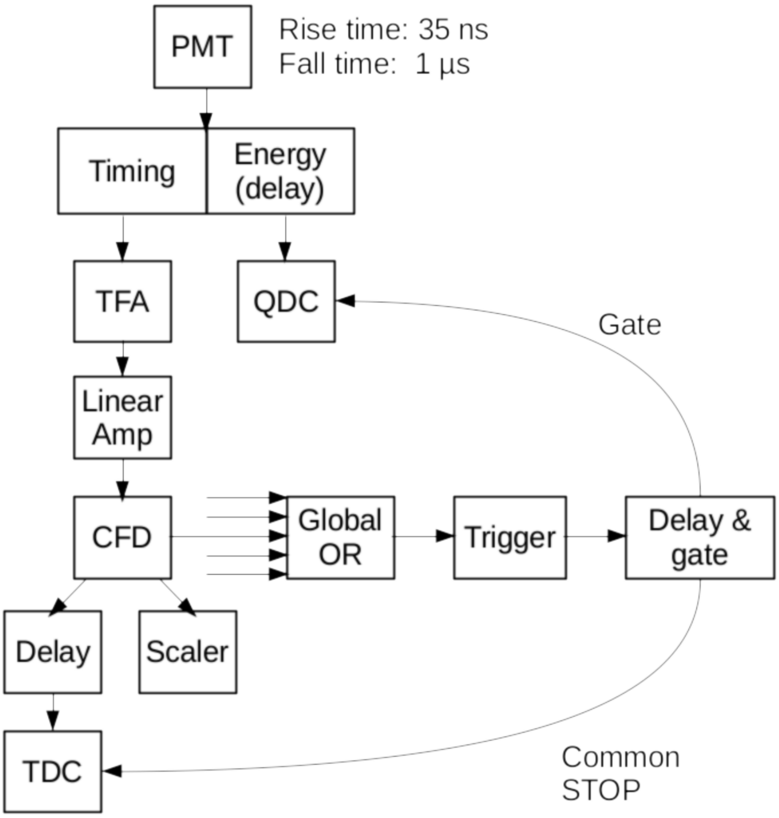

Figure 1.13: This drawing illustrates how the Crystal Ball was wired up –until 2009, says the source of the specification I used to produce it, which is internal to the GSI/R^{3}B collaboration.

Compton scattering, clustering and Doppler correction

The relatively high granularity of this detector allows for minimal losses due to photons that Compton-scatter and may leave one crystal, because they are likely to be intercepted by its neighbour –note that, due to the construction of the Crystal Ball, every crystal is completely surrounded by other crystals which are active and ready, unless one has been removed to create

---

[1] Time to digital converter.

a port.

Although the complete surrounding by detectors of every crystal can be used to clean up the spectrum significantly, as suggested by [Met82], if the Crystal Ball is used as a Compton-suppressed array, in the case of this experiment that would reduce the statistics too much to be useful. Thus the need to add-back, or cluster, the single hits to reconstruct the original energy of the photon arises. To that end, a specialized tool has been developed, see appendix B or the next chapter for a more detailed description.

The most useful feature of having a highly granular detector, though, is the possibility of accurately Doppler-correct the energy deposited by the photons: because they are coming from the ions[1], these photons are strongly Doppler shifted towards the blue and must be corrected; this correction is very sensitive to the angle with respect to the beam line (and the energy of the ion), thus the smaller the detectors and the more they are, the less uncertainty in the energy the Doppler correction will introduce –in fact, even with 162 crystals, the 7 degrees of uncertainty on the angle completely dominates the energy resolution of the Crystal Ball[2].

1.3.4 Reaction fragment tracking

After the target there are several detectors to intercept and measure charge, energy and time of flight of the fragments generated at the reaction site.

The charged fragments' trajectories are bent by the magnet, named ALADIN[3]: these fragments are tracked using two fibre detectors and two ToF[4] walls. Neutrons, though, do not deviate in a magnetic field because they don't have a net charge: they travel broadly along the same direction the beam was and are observed by R^3B's neutron detector, LAND.

LAND

LAND stands for "Large Area Neutron Detector" and it is a multi-plane neutron detector. It is constituted by 10 planes with a frontal area of 2×2 m^2, each consisting of 20 bars measuring $10 \times 10 \times 200$ cm^3. These bars are arranged horizontally and vertically, switching each plane, and contain iron and a plastic scintillator interleaved; 19 of these sheets are 5 mm in depth, scintillator and iron alike, while the first and last sheets are half the thickness, 2.5 mm, and are made out of iron –bringing the total to 21 sheets for 100 mm depth.

---

[1] At least, the ones we are interested in; as it will be discussed in the following, a great amount of background is generated and it is at rest in the laboratory frame of reference.

[2] For more details, please see the dedicated sections in Analysis: refdoppler-corr-section

[3] A LArge DIpole magNet, because ALDM just was not good enough. A description of the device can be found in section 1.3.5.

[4] Time of Flight.

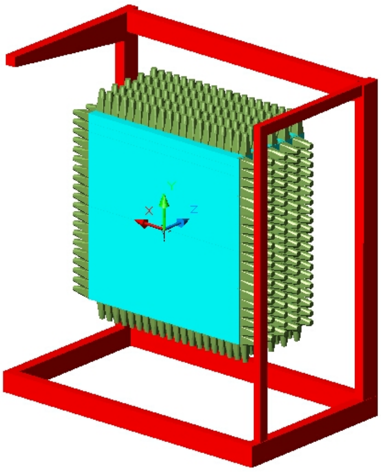

Figure 1.14: This rendering shows the structure of the LAND detector. The active elements are shown in light blue, the yellow components are the light collector structures (see figure 1.15) that convey light to the PMTs and in red the steel frame is shown. Credit: internal documentation.

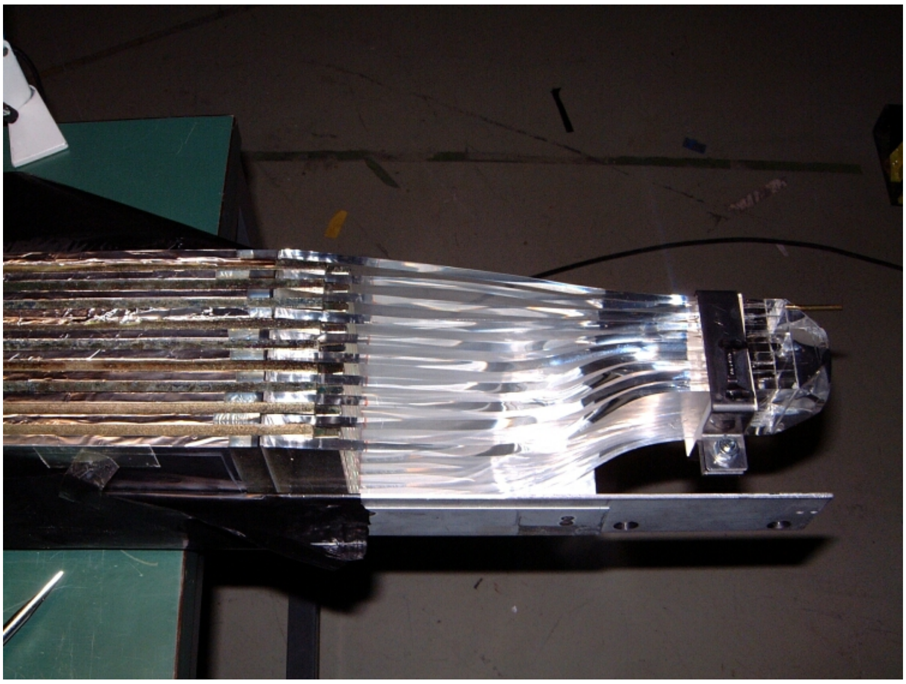

Figure 1.15: This picture shows the structure of a LAND paddle, and the collection structure that conveys the light to the PMT –which in this case is not installed, but would observe the scintillator strata from the right side. Credit: internal documentation.

The detector, which delivers time of flight (ToF), energy and interaction position for neutrons with energies greater than 150 MeV, works on the conversion principle: incoming neutrons are offered a large cross section for proton conversion reactions and, then, those protons are detected in the scintillator[1]. For the scope of this work, which focusses on the energy region *below* the neutron separation threshold, LAND is used as a veto. For more information about this detector capabilities and its construction, the reader can consult [BlEl91].

Fibre detectors

A "fibre detector" is a scintillator counter where the active material is arranged in thin fibres. These fibres can also conduct the light they emit, thanks to total internal reflection, and deliver it to light sensors for measurement. Because of their high granularity, they offer very good angular resolution even at shorter distances from the target.
The experiment S412 employs three detectors of this kind; in order to fully determine the trajectory followed by a fragment in the magnetic field and thus have access to is mass-to-charge ratio, it is necessary to have at least three points belonging to it –although redundancy is added value. The fibre detectors are part of the tracking solution and report the position of the fragments once they flew through the magnetic field.
One, new, fibre detector was developed at the time and placed at a short distance, 2.7 m, behind the centre of the magnet, the second and third, older, ones are respectively 12.0 and 12.4 m from the centre of the magnet and stand closely in front of the two ToF walls.
These two latter ones share the same construction: 50×50 cm^2 area filled with 1 mm wide scintillating fibres. To distinguish which fibre fired alongside collecting the light that has been emitted, on one side the fibres are observed by a position sensitive PMT, a photomultiplier tube whose anode is segmented and can relay information about where the light was collected. These detectors are described in further detail in [Cub98, Mah09].
The other, new fibre detector is constituted by 1024 fibres with a square cross section measuring 250×250 μm^2 of active material, plus 15 μm cladding. The detector's area is 30 cm by 20 cm width and height respectively. This detector is placed inside the vacuum chamber behind the magnet and provides the first tracking point.
The development of this detector has been part of the doctoral work of Dr. Philipp Schrock [Sch15] from the R^{3}B collaboration, and the reader is encouraged to consult his thesis for the whole details.

ToF walls

A "ToF wall" is a detector primarily conceived to provide accurate timing –hence the "time of flight" part of its name; energy and charge are also usually provided. The "wall" moniker comes from the detector arrangement: they are usually one or two relatively thin layers of

---

[1] This because neutrons have no net electric charge and, thus, interact extremely weakly with the scintillator's electrons and therefore give off no light.

scintillating material[1]. The detectors used in this experiment are also constituted of paddles, thus providing some degree of spatial information as well.
This experiment can count on two ToF walls, positioned one after the other: the NTF[2] and the TFW[3]. This solution has been chosen because both detector were old at the time of S412 and had aalready seen a considerable amount of beam and fragments, this led to significant radiation damage and non uniformity[4]; by employing two detectors, the hope was to combine the data from the two or ”simply” choose the best output.

Figure 1.16: A picture of the TFW, one of the ToF walls used in this experiment. The Time of Flight walls all share the same basic structure: one or two paddled planes observed by PMTs. The electronics for the readout is geared to give the most precise timing information possible. Credit: internal documentation.

The NTF comprises 8 paddles of plastic scintillator with an active volume of $48 \times 5 \times 0.5$ cm^{3}[5], whereas the TFW counts on two layers of large paddles, 18 vertical and 14 horizontal, with an

---

[1] With some mental bending, one can also call LAND a ToF wall, for neutrons. This definition is almost never used in the R^{3}B collaboration, because of the much enhanced capabilities of the LAND detector with respect to a run-off-the-mill ToF wall.

[2] New ToF wall.

[3] Time of Flight Wall.

[4] For a more extensive description of the procedure needed to interpret the NTF’s output, please see Dr. Andrea Horvat’s thesis [Hor19].

[5] Height by width by depth.

active volume of 189 × 10 × 0.5 cm^3 and 147 × 10 × 0.5 cm^3. In both cases, each end of the paddle is observed by a PMT.

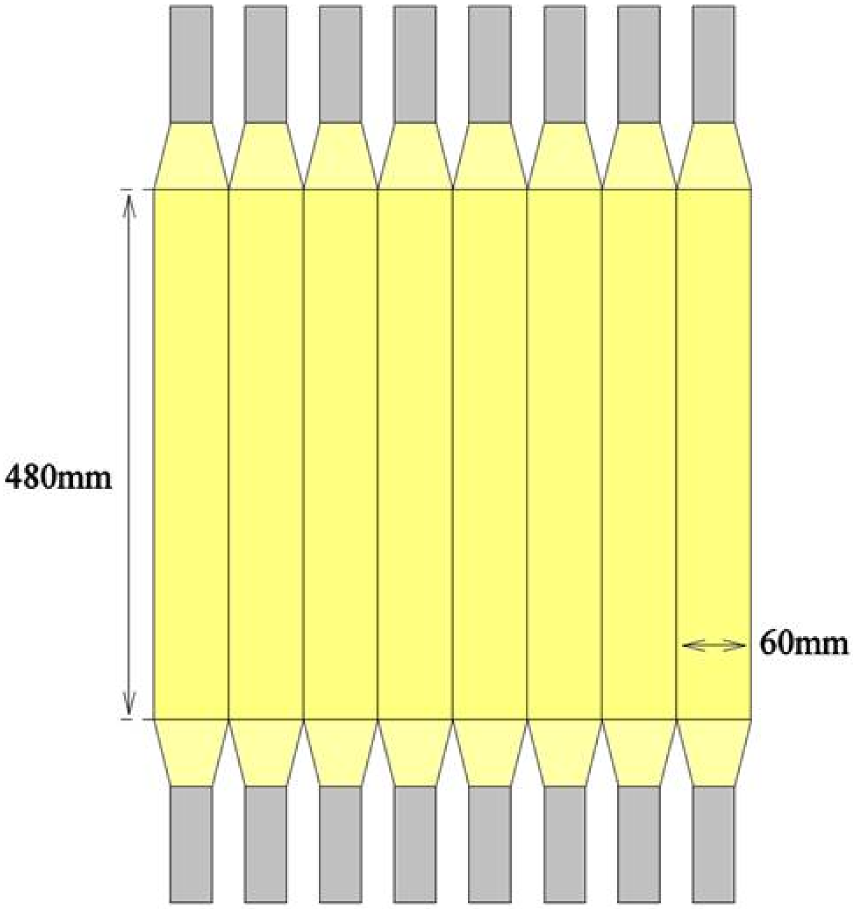

Figure 1.17: This drawing illustrates how one plane of the NTF is structured. The active material is in yellow, the light collectors at the end of the paddles are in gray. These parts allow for optimal coupling between the paddles and the PMTs' photocatodes. Credit: internal documentation.

1.3.5 Magnet assembly

Separating charged particles by passing them through a large and uniform magnetic field is a solid and very well established technique: particles with different mass-to-charge ratios will follow different trajectories in the magnetic field.

Because the ability to identify particles is critical, so is the design of the large dipole magnet that is going to produce the magnetic field and function as spectrometer. In S412, this role has been fulfilled by the ALADIN[1] device.

---

[1] A LArge DIpole magNet, because ALDM just was not good enough.

Figure 1.18: A picture of the ALADIN magnet outside Cave C; the magnet has been replaced since the experiment S412. Source: [FAIRweb].

Vacuum chamber and pipe

In order to avoid straggling of the fragment due to interaction with the air, a large evacuated volume (the vacuum chamber) follows the magnet. From this, a pipe, also under vacuum, extends until where the two ToF walls and two of the three fibre detector stands. This also reduces straggling due to atmospheric interaction.

1.3.6 Targets and beams

A fundamental part of the experimental setup are, of course, the targets. During this experiment a number of carbon, CH_2, Lead and Titanium targets have been used with beams spanning several neutron rich Tin isotopes.
This work focusses mostly on ^{132}Sn impinging on a ^{nat}Pb target with a thickness of
$1.132\ \mathrm{mg} \cdot \mathrm{cm}^2$. When target and beam are mentioned and nothing else is specified, I am referring to this couple.

Chapter 2

Analysis

What is written in this chapter This chapter contains a detailed description of the procedures and methods used during the analysis of the data from the S412 experiment.

What is not written in this chapter Many detectors have been already calibrated and characterized in previous works, for example [Wam11, Sch15, Sch17, Hor19]. In general these calibrations is supposed to be accurate and has been accepted for this work also.

2.1 Instruments

Because the experiment was long over when I began this analysis, the complete work has been performed in a computer[1]. The major software tools that allowed this work are Land02, a package originally developed by Dr. Håkan Jonasson at GSI, and a toolkit to handle the Crystal Ball data developed by me.

2.1.1 Land02

This software component is known as the unpacker. An unpacker, in the context of a GSI experiment, is a program that takes the data written by the DAQ[2] and, optionally at the user's wish, it can perform some operation and corrections to each single detector's data.
The DAQ saves data in the LMD format, which is described in [Jon06]; from there, Land02, with its program `paw-ntuple`, offers several "levels" of unpacking:

RAW The data is just translated from LMD to a specified format (usually, a CERN's ROOT file format).

TCAL At this level, the internal detector units for the timing are converted into nanoseconds and the pedestals are subtracted from the energy channels –although the values representing the energy are left in internal detector units.
The conversion factors and the information about the pedestals are calculated (sometimes:

---

[1] Not literally one, but no single screw has been turned.

[2] Data acquisition: this name indicates the hardware and software that reads out the detectors and saves the data to disk.

retrieved) by other programs in the suite. Once these are known, they are hard coded into the program[1].

SYNC The various detector modules are synchronized in time and the energy calibration is performed at this level: this includes correcting for offsets and non uniformities. In general, at this level a detector system is supposed to be confrontable with itself.
Of course, because detectors may use very different electronics and detection principles, the details to calibrate each one are specific and cannot, in general, be ported from a system to another. This means that each detector requires its own code domain for its calibration.

DHIT At this level, the detector information obtained in SYNC are aggregate to calculate quantities such as the coordinates of an interaction in the detector's own units.

HIT This level translates the detector coordinates (and units) into global ones: for example an interaction that happened in the NTF will be located with respect of the target coordinate system in SI units.

TRACK The information of every detector, now comparable with all others, are aggregated at this level. This allows for the calculation of the incoming relativistic beta[2], charge and mass-to-charge ratio.

While most detector could count on all unpack levels, the Crystal Ball could not and it stops at SYNC level[3]. This prompted the development of "The Toolkit", also known as `xb_progs`. This is a collection of programs aimed at the first part of the data analysis.

2.1.2 The Toolkit

Before they can be used to do some Physics, the Crystal Ball data have to be aggregated and Doppler-corrected[4].

Clustering

One of the fundamental ways photons interact with matter is by means of the Compton scattering: energetic photons scatter on the electron of the material, which although bound are

---

[1] An approach that requires the programs to be recompiled for each experiment, which may bring some speed ups on repeated execution but is not the most practical.

[2] $\beta = v/c$

[3] Some internal documentation hinted to the possibility of obtaining also a DHIT level, which as we will see soon enough means clustering for the CB, but this functionality wasn't available to me or the colleagues I had access to.

[4] In the previous chapter I reported on the design goals of the Crystal Ball and one of them was to have a detector granular enough to allow for a satisfactory doppler correction of the photon's energy.

effectively quasi-free compared with the energy of the incoming radiation. When this happens, only some of the energy of the photon is deposited in the detector and the outgoing radiation goes on, occasionally escaping completely but mostly interacting in neighbouring crystals. Therefore, to get an accurate calorimetry, it is often necessary to sum more single hits in the detector.

Although granular, the Crystal Ball consists “only” of 162[1] and only a few of them (typically in the order of 10 or 20 crystals) register a hit every event; for this reason advanced clustering algorithm such as K-means are not necessary. Indeed, the approach followed until this point has been to locate the largest energy deposit in the event, sum all the energy left in the neighbourhood[2] and do so until every energy deposit in the event was associated to its own cluster [Sch15].

This approach has been deemed sufficient above the neutron separation threshold because, although one would expect lower energy photons in general and thus be even more affected by the presence of the atomic background[3], these photons would have represented a lesser fraction of the total excitation energy, because most of E^* is carried away by neutrons. In the case of this work, the energy is completely carried away by photons, thus distortions such as those visible in figure 2.1 become even more dominant. To overcome this difficulty, a slightly more nuanced approach has been developed under an assumption and an observation:

- Firstly, we can reasonably assume that the incoming photons don’t leak from one detector module to multiple others in the immediate neighbourhood: if the photon scatters after a Compton interaction, it’s the photon itself[4] that exits the detector, whereas the electron upon which the photon scattered should deposit all its energy in the active volume (and thus be seen) or, in the worst case, be stopped in the alluminium wrapping of the segment (in which case the energy is lost, but there is no way around it). Also in the case of a pair creation, a double escape is less likely than a single escape event.

  Given all this, it is reasonable to assume that if a photon is not stopped in the crystal of first arrival, the interaction will continue in a single other crystal instead of all the neighbourhood.

- Secondly, simulations show that the number of scatterings a photon goes through can be put in relation with the energy of the first interaction. This was first observed in [Lin13]

---

[1] A few less, as discussed before, to have a free beam line and allow for mounting struts.

[2] Typically, two orders of neighbourhood. Keeping in mind how the CB is structured, it is possible to define concentric rings of detectors around each single crystal. In this work, “order of neighbourhood” indicates one of these rings, first being the innermost and moving outside with increasing index.

[3] Please refer to the section dedicated to this phenomenon for more information.

[4] Although when studying the interaction of radiation with matter it is customary to consider a scattering photon as removed from the beam [Krane87], in this case I am interested in reconstructing the total energy of the original photon, thus I conceptually follow it.

and the study was repeated for this work, in order to tune the algorithm.

Given these two points, the new clustering has been developed and tested against the old one.

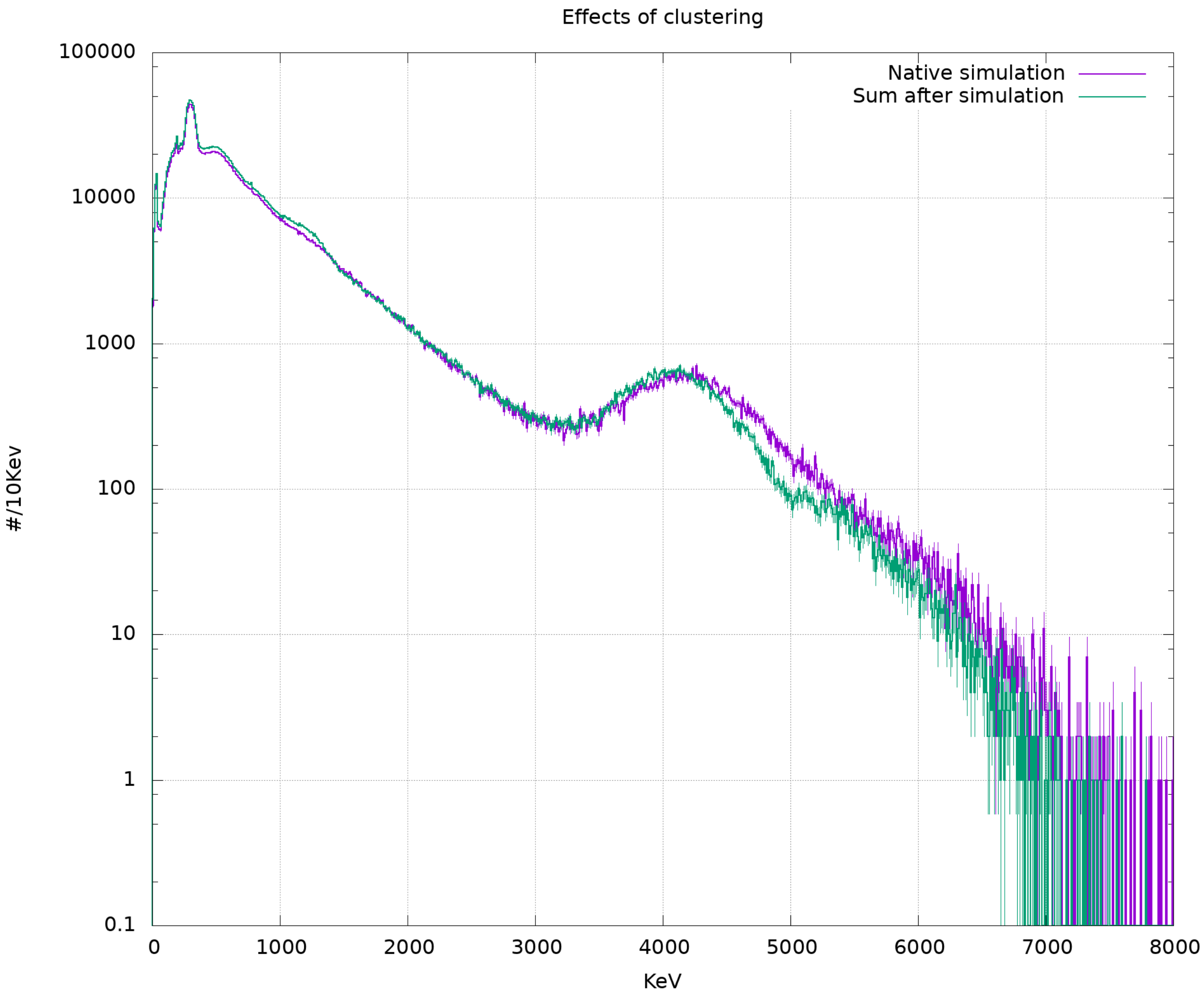

Figure 2.1: A comparison between summing a signal to a big background before and after the simulation. The plots are obtained from a 100 kiloevent simulation containing two peaks, one at around 1.2 and the other at around 4 MeV (energies that were randomly chosen to be very close to the 2^+ state of ^{124}Sn and ^{132}Sn). The violet line represent the system response of the Crystal Ball clustered to the second nearest neighbour, whereas the green line shows the same set of events, simulated and analysed separately *and then* summed as spectra. It is very apparent that the second to nearest neighbour clustering algorithm introduces a shift toward the higher energies for the 4 MeV peak, and almost completely misses the lower energy ones, whereas if the events are simulated separately and then the spectra summed, the spectrum is much more clear.

Resolution and sensitivity comparison The comparison ran as follows: first of all, 10^4 dichromatic events have been generated: each event contained two photons at 1 MeV and 4 MeV[1], which were then emitted isotropically and then Doppler shifted along the beam line at an energy close to that of the experiment. As a first step, the set of events has been simulated as it was: completely without background.

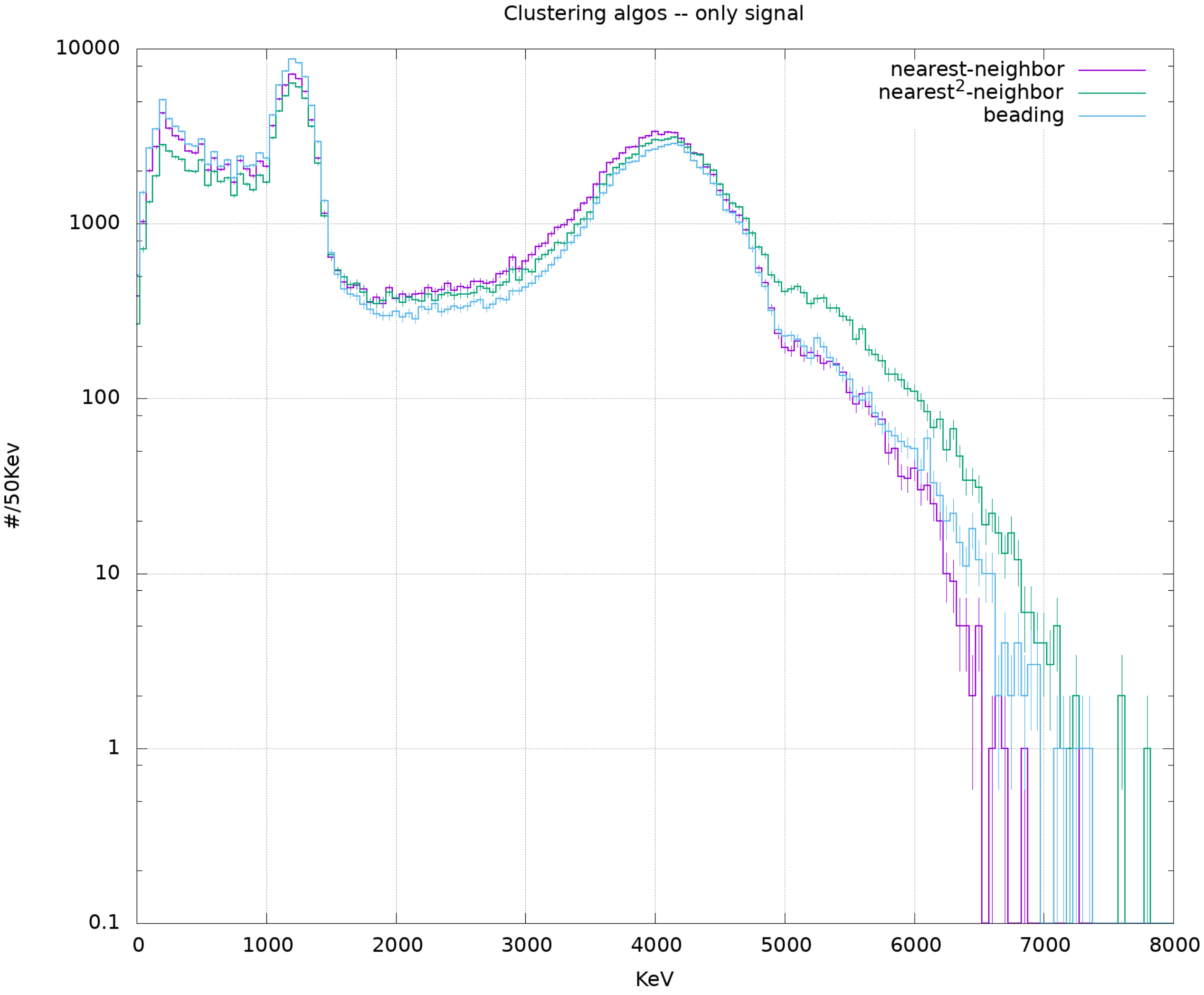

Figure 2.2: A comparison of nearest, second to nearest and beading clustering algorithms on 100 kiloevents, without background. While the nearest-neighbour (violet line) and the beading (blue line) are quite close, the second to nearest neighbour already shows its propensity to overestimate the energy of the deposits. Furthermore, the beading algorithm is slightly outperforming the nearest-neighbour one, introducing a smaller tail of the 4 MeV peak towards the lower energies.

The main result of this comparison is that the new algorithm, in ideal conditions, behaves very

---

[1] These energies have not been selected totally at random: they are close to landmark states for ^{124}Sn and ^{132}Sn, which had the hope to be visible despite the prominence of the background.

closely as the old, proven and accepted one[1].

Multiplicity vs. Energy To study the dependence of the hit multiplicity from the energy of the photon, I have generated a number of event sets spanning from 500 keV to 30 MeV, with a 1 MeV stepping: each set contains 10^5 events constituted by a single photon of a given energy, emitted isotropically. Of course, no background has been added and also the shielding around the target and other target chamber furniture have not been included.

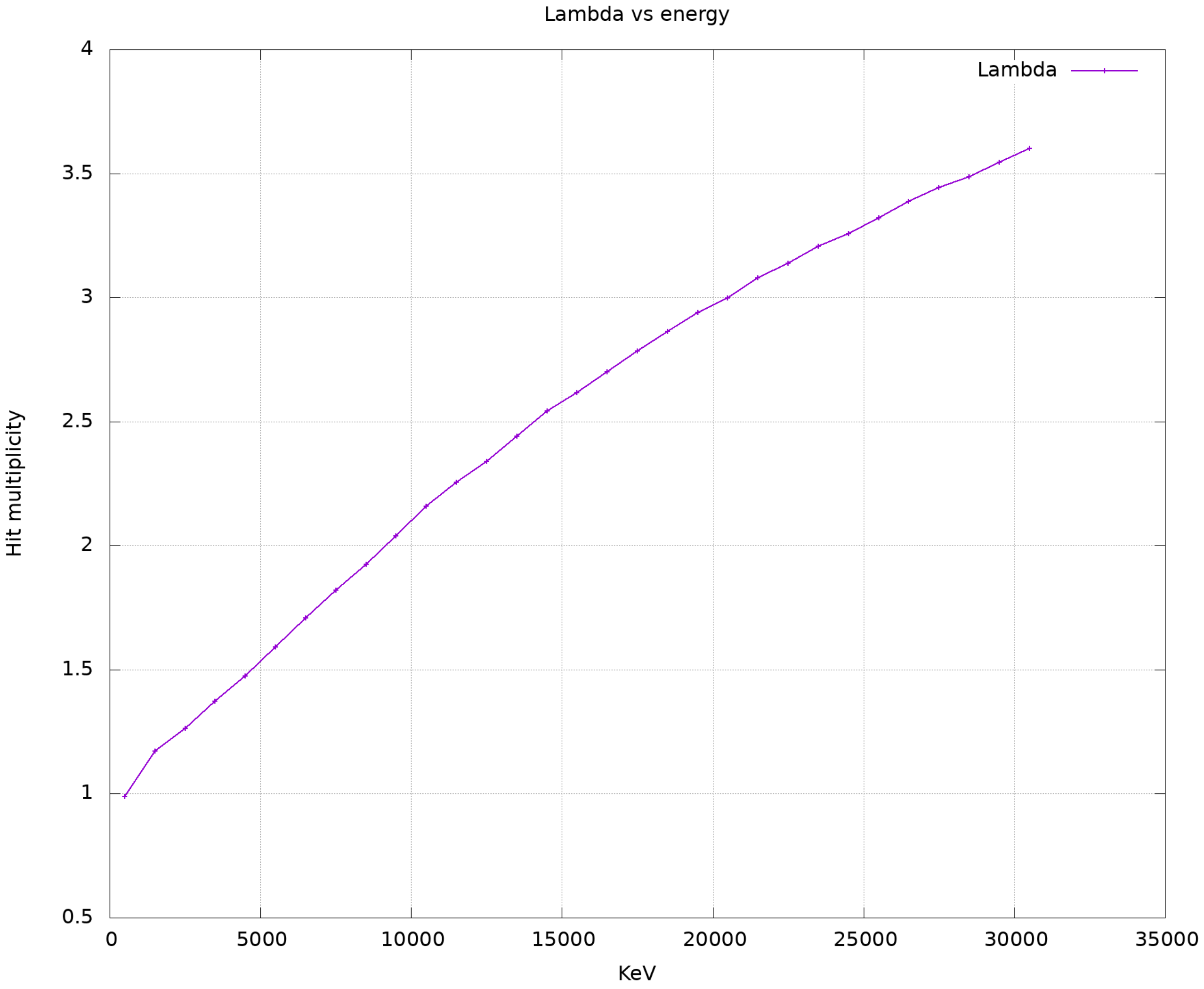

Figure 2.3: The evolution of the λ value of the distribution of the hit multiplicity, varying the energy. Note that the abscissa i the total energy of the photon (and the event), not the one of the first interaction.

In this case it is also not necessary to Doppler shift the photons in the direction of the beam

---

[1] In fact, the differences between the two spectra, since the simulation is the same, are *entirely* due to the different behaviour of the two algorithms. Alas, repeating the simulation, in this case, would not have created a different dataset, because of the concept of repeatability coded in GEANT.

because the interest is in the dependence from the energy of the multiplicity.

These event sets are then simulated with the Crystal Ball in place[1] and the hit multiplicity in the detector is then examined -because only one photon is present for each event, all the hits should come from that.

Unsurprisingly, the hit multiplicity at a given energy distributes according to a Poisson statistics: the energy dependence, then, is carried by the distribution's parameter. In figure 2.3, the dependence of the distribution parameter λ from the energy is shown.

The plot in figure 2.3 illustrates an expected trend, but the λ parameter is not the best choice to instruct the clustering algorithm: a better one is to utilize the 90% quantile of the fitted distribution. As a reference, the following table shows the expected multiplicity for the 70% quantile and the 90% quantile:

---

[1] In the virtual environment

Energy (keV)	**70% quantile**	**90% quantile**
500	1	2
1500	2	3
2500	2	3
3500	2	3
4500	2	3
5500	2	3
6500	2	3
7500	2	4
8500	3	4
9500	3	4
10500	3	4
11500	3	4
12500	3	4
13500	3	5
14500	3	5
15500	3	5
16500	3	5
17500	4	5
18500	4	5
19500	4	5
20500	4	5
21500	4	5
22500	4	5
23500	4	6
24500	4	6
25500	4	6
26500	4	6
27500	4	6
28500	4	6
29500	4	6
30500	4	6

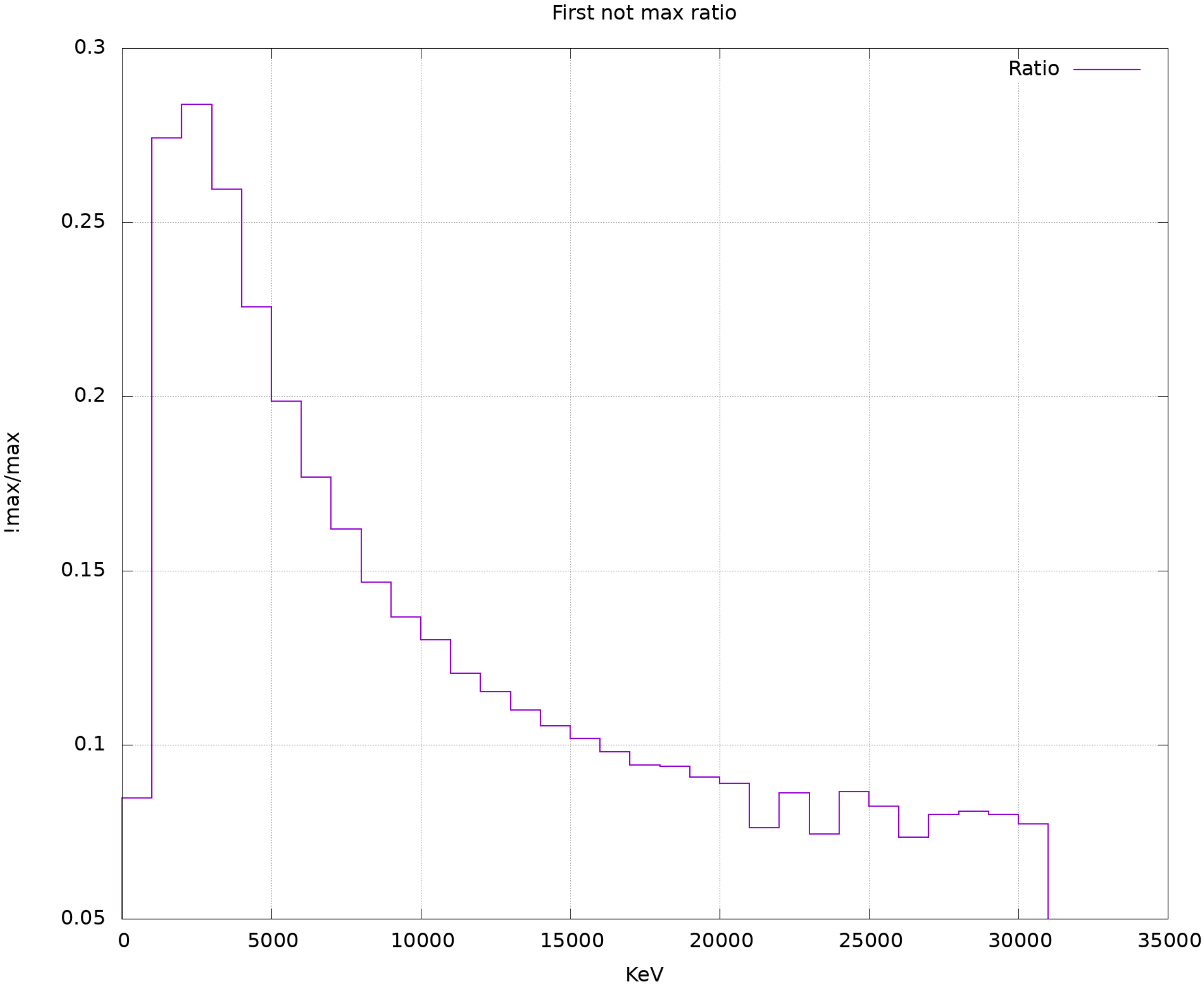

Figure 2.4: This plot shows the ratio between the events that do *not* have the first energy deposit as their largest over those that do. Note that the hypothesis becomes more and more realistic the higher the energy, while it's true between 80% and 70% of the times as the total energy becomes lower. The binning of the plot is the same as the simulations: 0.5 MeV.
Technical note: one should not read too much into this graph anyway: the underlying hypothesis is that GEANT3.21 will report the hits as they happen and then R3BRoot will save them in that order; it appears to be so, reading the code, and parallelism is not implemented while processing a single event, thus race conditions are not to be expected. Nevertheless, the actual behaviour of the software has not been directly tested against its design in this case: the order should be maintained and there are no reasons why it shouldn't, but I did not explicitly test if this is actually the case (and how often this is not the case, if it happens).

At this point, it is also possible to verify whether the hypothesis that the first interaction carries the largest energy holds. As can be seen in figure 2.4, the validity of the hypothesis is not constant throughout all the incoming photon energies and, in particular, it's at its lowest when in the scope of this work. In any case, though, still more than 70% of the incoming photons leave the most energetic deposit as their first, thus I decided to keep the assumption that the most energetic deposit is also the centroid of the cluster.

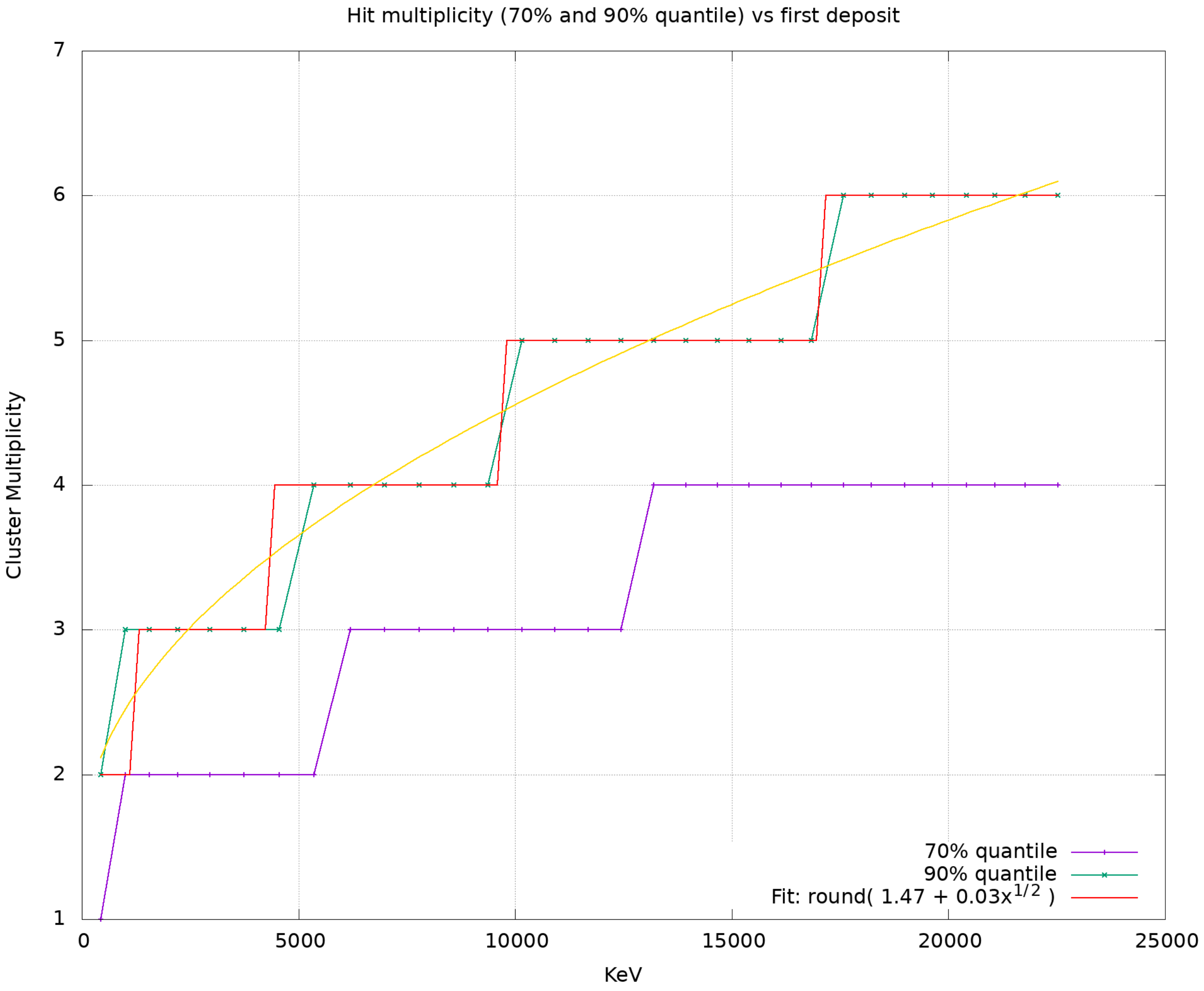

Figure 2.5: This Plot illustrates the dependence 70% and 90% quantiles of the multiplicity distribution from the first deposit energy (which is not the total energy). The algorithm considers the 90% quantile and, to that end, a fit has been carried out on that curve: the yellow line represents the function as it is, whereas the red line is the rounding of that expression, which is what the algorithm uses to set the maximum number of deposit to include in the cluster. More details about this procedure are given in the appendix B.

Although a general law may be a big ask (especially since this study happened exclusively in a calculator and not in real life), it is possible to link the expected value for the hit multiplicity with the first interaction energy. This allows to have a self adjusting clustering algorithm which is able to “tip-toe” competently around the background photons. For more details about the operation of the algorithms, please refer to the appendix B.

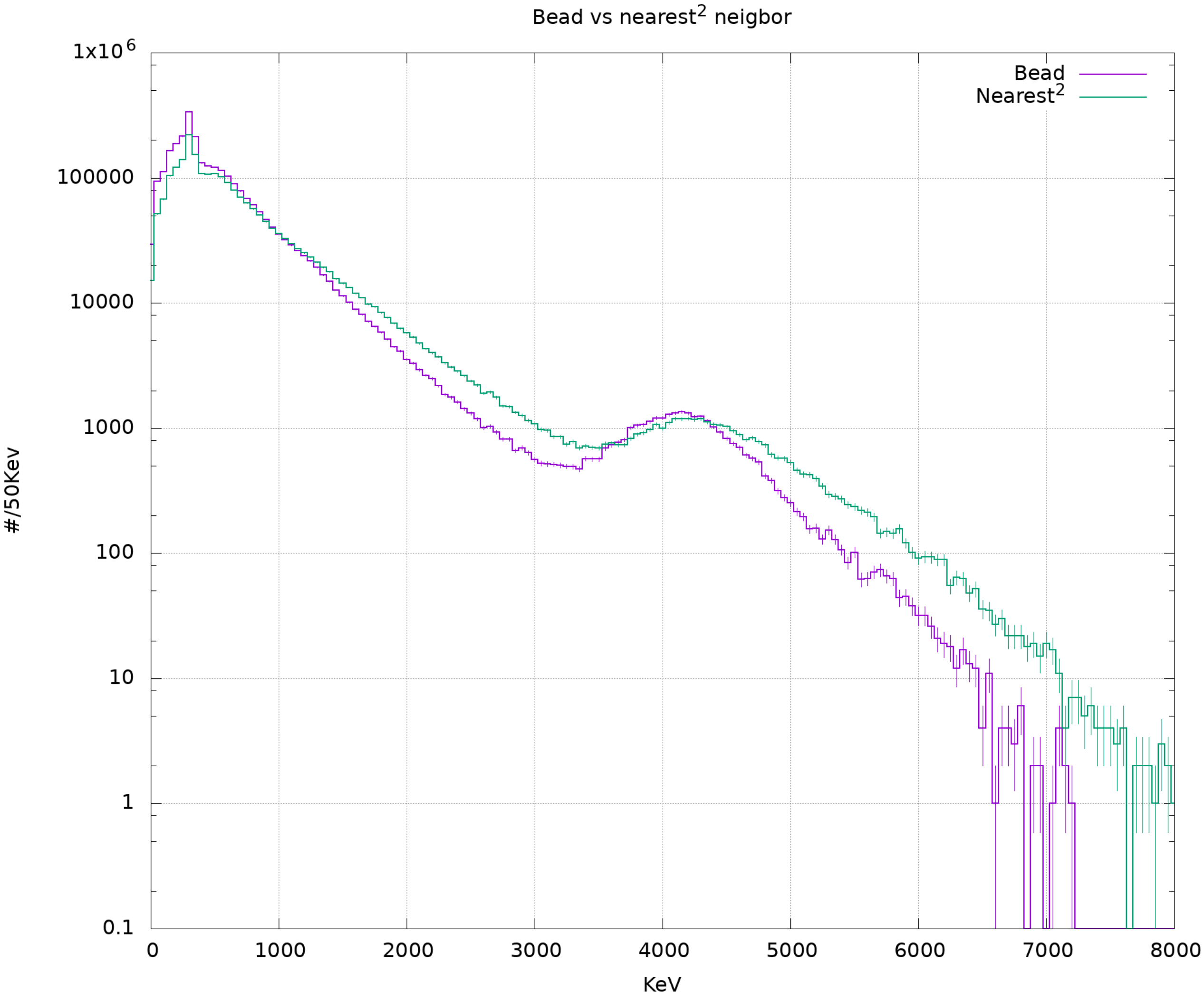

Figure 2.6: This plot compares the second to nearest neighbour algorithm with the beading algorithm. The difference between the two spectra is relevant and a strong point in favour to use the beading algorithm instead of the old one.
The nearest neighbour algorithm (not shown) is broadly similar in performance to the beading one, but conflicts with the expectation of multiple scattering events at higher photon energies. The data set is a 600 kiloevent simulation, containing both signal and background as the events are passed to the simulator program

As it is apparent, the ”beading” clustering algorithm improves the resolution throughout the spectrum and markedly outperforms the sum of neighbours algorithm at lower energies, where it makes visible the signal at 1 MeV, when compared with the approach utilised before of summing two orders of neighbourhood. quantitatively, this amounts to an improvement in resolution $\frac{dE}{E}$ on the 4 MeV peak from 0.32 ± 0.03 to 0.26 ± 0.04, calculated on the FWHM of the peak.

In this region, limiting the summation to one single ring of neighbouring crystals will obtain a similar resolution to the "beading" approach, although it is expected that a significant fraction of photons will scatter more than once at this energy. A possible explanation for this similarity in performance would be that the photons still have a significant chance to scatter back in the neighbourhood ring –or, alternatively, a "happy accident" where the atomic background picked up in the first neighbourhood ring would on average account for the energy lost out of it from scattering photons.

Given the close call in performance and the analysis done to come up with the beading algorithm, I chose to adopt this one over the sum on the single ring of neighbourhood for this work.

Timing In this analysis, I did not use the time of arrival given by the Crystal Ball to inform the clustering. The maximum timing resolution of the crystals is be 2.5 ns [Met82]: this value would already limit the spatial resolution of the array to 70 cm, which is considerably more than the maximum width of the crystals, thus even if the electronics would be ideal, ordering the events based on timing information would prove challenging.
The electronics is not ideal, though, and the time resolution of the whole Crystal Ball is around 30 ns. Although it would be possible to consider for a cluster only events in a window 60 ns wide centred on the time of arrival for the centroid, this condition would comprise the vast majority of the deposits anyway and would be of limited use when the new algorithm is in place. Furthermore, not all deposits in a Crystal Ball event have valid time stamps, with a prevalence that depends on how restrictive the data selection is (these deposits are less numerous when the reaction channel is selected): the reason for this behaviour is not completely clear, although several conversations with DAQ specialists have pointed to the possibility that it's an electronic issue.

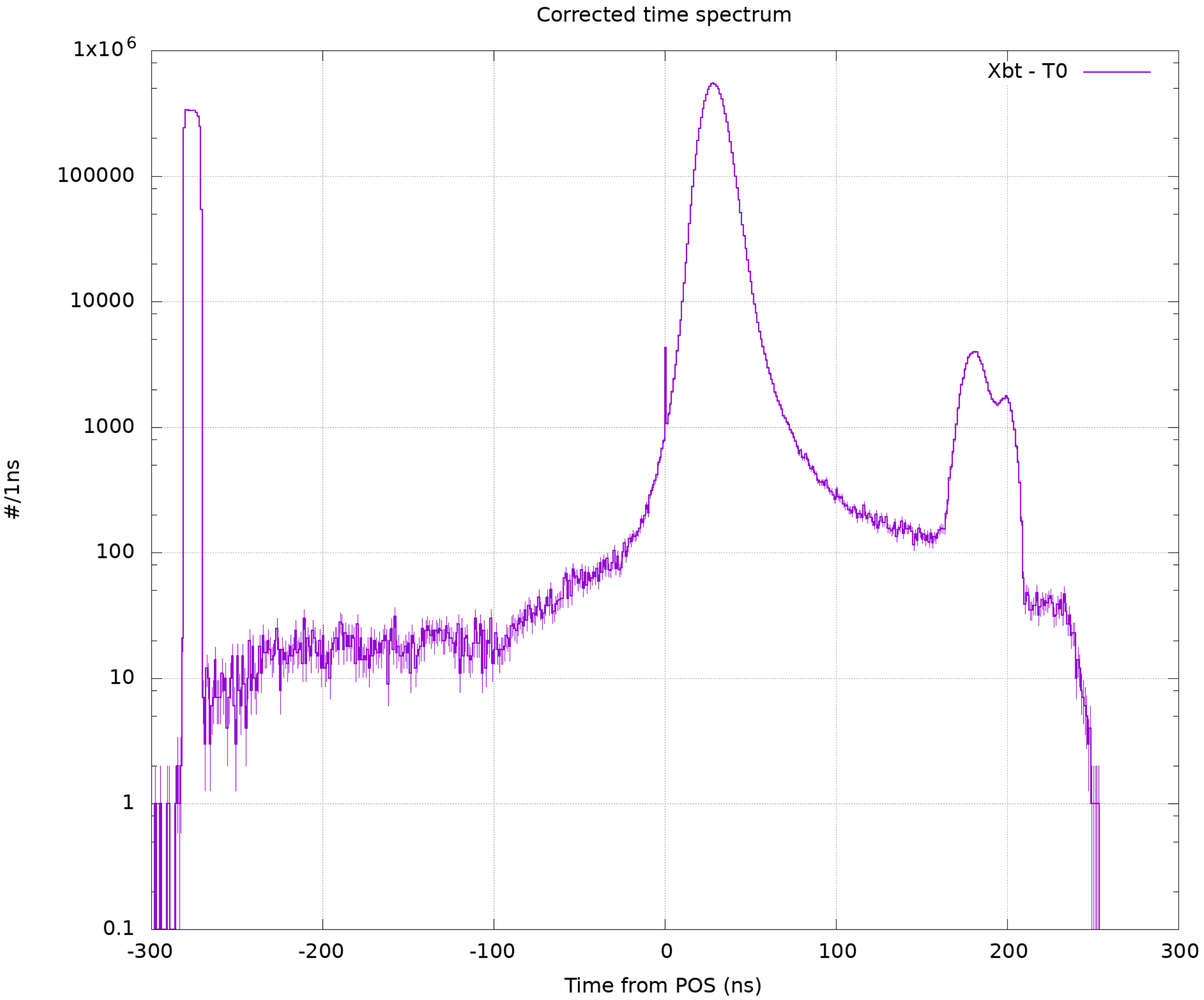

Figure 2.7: The calibrated time spectrum of the complete Crystal Ball. There are some interesting features to highlight. Firstly, the large peak between 0 and 100 ns represents the photons coming from the ions (and the target, shall there be any): these are the photons coming from the first interaction. Secondly, there is a feature at higher times, from 150 ns to slightly past 200 ns after the POS detector: these photons appear only in the back of the Crystal Ball (see section 2.4.1 for an illustration of front and back of the detector) and carry a very low energy; an hypothesis on their origin is that they come from the beam dump, but they play no role in the present analysis because of where they are located in the detector. Lastly, there is a sharp peak at very early times: those signals, as discussed in the text, are believed to be electronic artifacts and are excluded from the data sample by selecting the reaction channel.

Doppler correction

After the clustering, the energy deposits are organized in a data structure which also indicates the centroid: the crystal where the algorithm believes the first interaction happens. This is important for the Doppler correction because the location of the centroid sets the angle with respect to the beam line at which the photon was flying and, therefore, the correction factor for *all* the deposits belonging to the cluster.

Although the software has the flexibility of performing the Doppler correction on both clustered and non clustered data, there is a very strong argument to be made in favour of performing the Doppler correction *after* the clustering [Wam11]. It respects the chain of events: the photon had to first arrive in a crystal of the detector before scattering elsewhere and depositing more energy there.

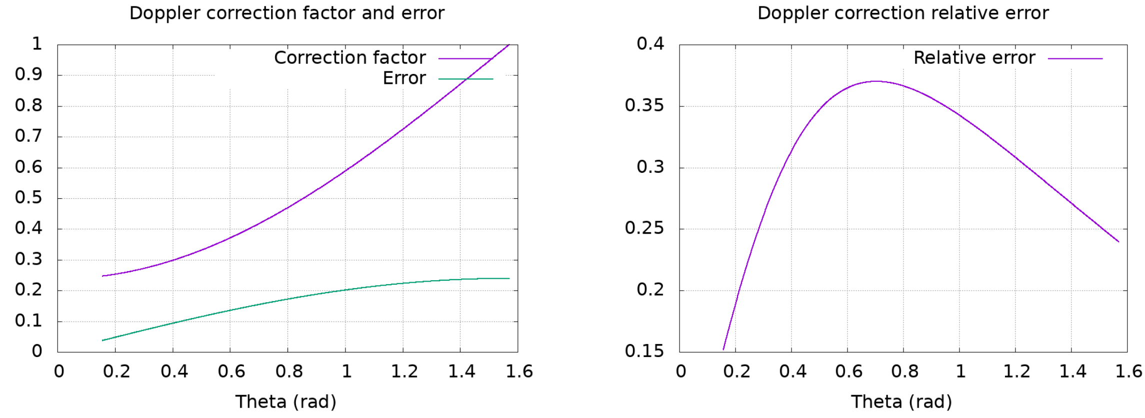

(a) The doppler correction factor and the uncertainty upon it

(b) The relative error on the doppler correction factor.

Figure 2.8: These plots show the evolution of the Doppler correction factor, $(1 - \beta \cos(\theta))$, and the uncertainty introduced on it by the granularity of the detector. As can be easily seen, the physical extension of the crystals is very relevant. It should also be noted that the $\frac{\pi}{10}$ angular aperture used here is a rough estimate and will vary for each crystal, depending on the frustum's base and orientation. Nevertheless, for all the energies considered in this work, the Doppler correction is *the* limiting factor to the energy resolution of the detector.

Note also that the correction, which is multiplicative, becomes one at $\pi/2$, but the actual Doppler shift of the photon's energy will be in general *more* than one from lower elevations already: in the formula 2.1 also the Lorentz factor $\frac{1}{\sqrt{1-\beta^2}}$ is present, which is always greater than one for $\beta \neq 0$.

Furthermore, the Doppler correction is by far and away the largest limiting factor of the whole detector resolution. In fact, although the resolution of the single crystal is around 70 keV at 1 MeV [Met82], the structure of the Crystal Ball has to be considered yet again: although the granularity is high for a NaI detector, the angular aperture observed by each crystal is still broad: around $\frac{\pi}{10}$. Since there is no available information on *where in the crystal* the photon arrived, we are forced to assume that it flew from the centre of the target along the longitudinal axis of said crystal. The uncertainty introduced thus is large and varies from around 15% to 35%, as shown in figure 2.8. Then, there will be an uncertainty on the measured β, used in the Doppler correction, that will affect the uncertainty on this quantity, but to a lesser extent.

To apply the Doppler correction, this rather standard formula for the relativistic Doppler shift is used:

$$E' = E\gamma(1 - \beta\cos(\theta)) \tag{2.1}$$

where θ is the angle between the crystal's geometrical centre and the beam line, E is the energy and β and γ are, as usual, the fraction of the speed of light the source is travelling at and the Lorentz factor.

2.2 Energy (and time) calibration

For this experiment, the Land02 output for the Crystal Ball and all other detectors was already calibrated. Nevertheless, the accuracy of the software has been checked for the gamma spectrometer.

2.2.1 Crystal Ball calibration

The procedure to calibrate the Crystal Ball is straight forward: during the experimental campaign, some data acquisition runs have been taken with a radioactive source (^{60}Co and ^{22}Na) placed closely to, usually, one half of the open Crystal Ball[1]. These sources, of course, have a very well known spectrum and, thus, one can use the position of the peaks to translate detector units into energy –typically, keV are a good choice.

As stated above, the detectors were already calibrated for this experiment when this work started and not much had to be done further. Nevertheless, an extensive check has been performed and the calibration has proven to be accurate within a keV for every crystal, well below the 70 keV quoted resolution for the devices. Furthermore, the resolution of the whole detector during the experiment is not limited by the crystals' energy resolution but from their spatial extension, as discussed in the previous section.

For this reason, also the energy calibration hasn't been over refined: NaI crystals are known to behave linearly [Krane87] enough and therefore more peak-rich sources like a Thorium one have not been employed.

---

[1] This approach allows for, essentially, parallel execution of two calibration runs at a time, when the detector is not being used due to maintenance or other operation on the experimental set-up.

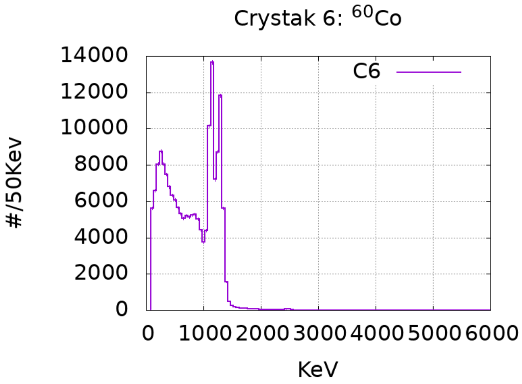

(a) The spectrum taken from crystal number 6 of the Crystal Ball. It's at the detector's right (crystal 1 being the rightmost). The source used to calibrate this half of the Crystal Ball was a ^{60}Co sample.

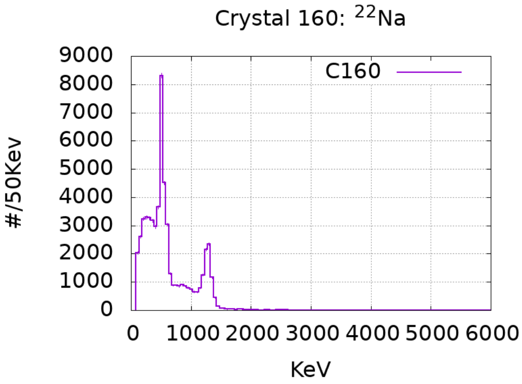

(b) The spectrum taken from crystal number 160 of the Crystal Ball (crystal 162 being the leftmost). The source used to calibrate this side of the Crystal Ball was a ^{22}Na sample.

2.3 Event selection

During an experiment where a relativistic radioactive beam impinges on a thick target a whole lot happens and, in general, it is not possible to restrict the range of reactions that can happen enough to have one single channel -actually, to investigate the most possible physics, restricting too much may be seen as counter-productive.

This means, in turn, that the reaction channels have to be selected after, by looking at the data.

2.3.1 Trigger matrices

A useful instrument to identify a reaction channel are the so-called *trigger matrices*. Each detector in the experiment produces a trigger of its own, and these are then collected by the DAQ which makes a global trigger decision[1] and eventually writes the event to storage.

For example, as mentioned in the introduction, the ROLU detector is used as veto: if a trigger for this detector is produced, the event will not be saved as the ion(s) are following a trajectory that would be out of acceptance for other detectors, or the magnet. More specific to this work is the interest for Coulomb excitation events that do not result in a neutron being lost: this means that the neutron detector LAND will be monitored to verify that no neutron has appeared in it before considering an event for analysis.

An example of a trigger matrix of interest for this analysis is shown in the following table. This table represents what three consecutive events may look like when the triggers are observed. In

---

[1] For the details about how this work, see [Jon06].

Produced Trigger			Required Signal(s)					
Tbit	Tpat ($= 2^{Tbit-1}$)	Name	POS!ROLU	NTF mul	XB OR	XB Sum	TFW mul	Spill on
1	1	Good Beam	x					x
2	2	Fragment	x	x				x
3	4	XB OR	x	x	x			x
4	8	XB Sum	x			x		x
5	16	Proton	x	x			x	x

Figure 2.10: This table illlustrate an example of how a trigger matrix is structure: the single detectors would produce a trigger that is then organised in an higher level flag for every event. Credit: Dr. F. Wamers [Wam11].

the case of this work, the third event is the one that will be selected. The names of the trigger flags are real, and represent, respectively:

POS!ROLU Also known as "good beam" trigger: the POS detector saw an ion that was not seen by the ROLU.

XB SUM This is one of the trigger generated by the Crystal Ball; in this case it's set when the sum of all crystals exceeds a given threshold, which is set for every data acquisition run. Another trigger generated by the Crystal Ball is "XB OR", which is set whenever either of the two halves has seen a sufficient amount of energy[1].

NTF It's the trigger generated by the NTF detector.

LAND It's the trigger generated by LAND: the detector has seen a neutron[2].

If we were looking just at the trigger matrix above, we would select for this analysis only the their event from the left, because it has the correct trigger pattern[3].

Downscaling Another important aspect to keep in mind, when discussing the triggering, is the so-called *downscaling* of the triggers: this is a stride applied to triggers that are too frequent for the DAQ to record all the events that generate them. The main DAQ listens to all

---

[1] Although it would be slightly more practical for this experiment to have the Crystal Ball divided into a front and a back domain considering the beam axis, the detector is wired and constructed such as the domains are left and right with respect to the beam axis, and the floor.

[2] The LAND trigger should be treated with care: because of the detection principle, it is relatively easy to obtain false positives and additional conditions have to be employed to discriminate background from real neutrons.

[3] Or Tpat. For more information, see [Wam11, Jon06] among others.

detectors waiting for the first trigger (master start); when this arrives, all electronic is read out and the data written to storage. This of course takes time and, if one trigger always happened, the DAQ would be completely saturated and potentially in dead time when interesting physics happens.

One such trigger is the one generated by the NTF in the fragment arm. Both unreacted beam and fragments strike the detector, so the trigger it generates is very common, also when no reactions happened. Therefore, this trigger is accepted once every 2^n times, where n is the number that is indicated as "downscaling".

This feature has to be taken into consideration when calculating cross sections, since it affects the reaction probability, and must also be treated with care, because it can create baffling artefacts, see [Hor19].

Because of this "quirk", and how the XB SUM trigger behaves, I have found that the trigger matrices are not a particularly powerful discriminant *after* the cuts for selecting the reaction channel are applied to the data. Nevertheless, a check on the downscaling is always performed to verify that no distortion of the data is happening –for example, if a downscaling factor deviates significantly from the one specified on the run sheet, there may be a problem that needs to be investigated.

2.3.2 Incoming isotope identification

As mentioned in the introduction, it is possible to label incoming ions by combining the information from the detectors before the magnet. The reconstructed information (already by the unpacker) consists in the charge, the mass-to-charge ratio, the incoming velocity and the velocity in the middle of the target.

To identify the incoming isotope, the charge and mass-to-charge ratio are used, as shown in figure 2.11. It is apparent from the plots above that the separation of incoming isotopes is good. Despite that, there is an offset in the charge determination (the reason for it is a non perfectly subtracted pedestal[1] in one of the PSPs); also, the detectors aren't perfectly stable throughout the different runs, so a correction has to be applied.

To deduce such correction, I developed a tool that tracks where ^{132}Sn should be and searches in the neighbourhood for the closest peak in the mass-to-charge ratio and charge, fits it with a Gaussian distribution, and calculates the shift that is needed to have the centroids of the fitted curves at $\frac{A}{Z} = 2.64$ and $Z = 50$. This procedure is repeated over all the dataset with a moving window of around 30 thousand events and an overlap of around 10% between subsequent steps. This generates a set of points, which are then put in correspondence with the event index[2].

---

[1] A pedestal is the signal a detector gives, or has to give, when no energy is deposited in it.

[2] Not to be confused by the event number: when I write about an event index, I mean the position the event has in the current set, whereas the event number is a hopefully unique number assigned to the event by the DAQ.

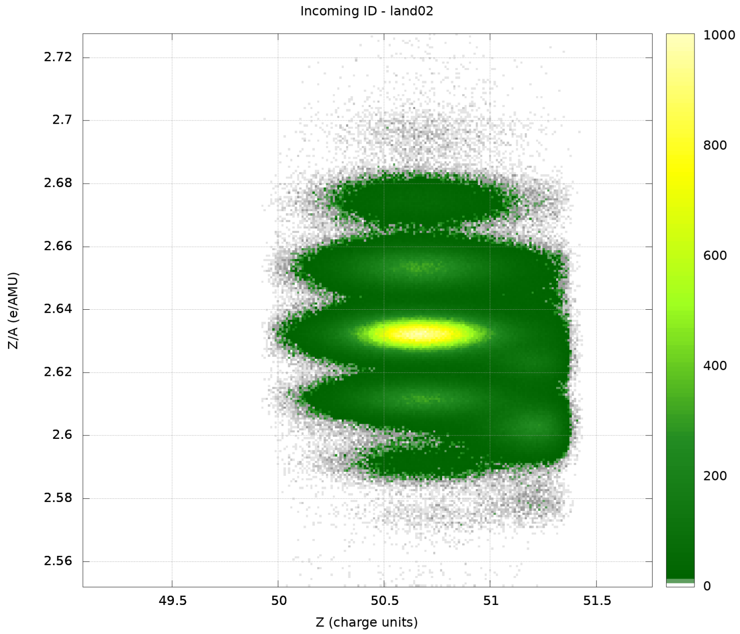

(a) The events as reported by Land02.

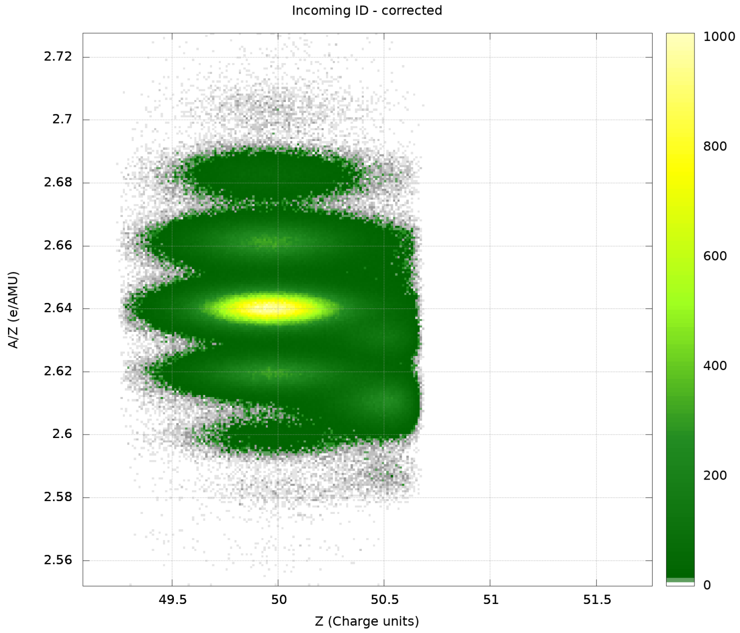

(b) The events after the correction.

Figure 2.11: These two “heat maps” represent the density of events from the perspective of the isotope identification: the plane, which will appear also in the following, is mass-to-charge ratio versus charge and, for this occasion, the colour scale is linear. The densest cluster of events are ^{132}Sn ions entering the experimental set-up. This cluster of events is used to correct the charge and the mass-to-charge ratio, such as ^{132}Sn events are at their densest at coordinates (50, 2.64). Note also that some lax pre selection has already been applied to focus on Tin isotope, whereas other atomic number were also present in the beam; this was not an issue, because the isotopes are well separated.

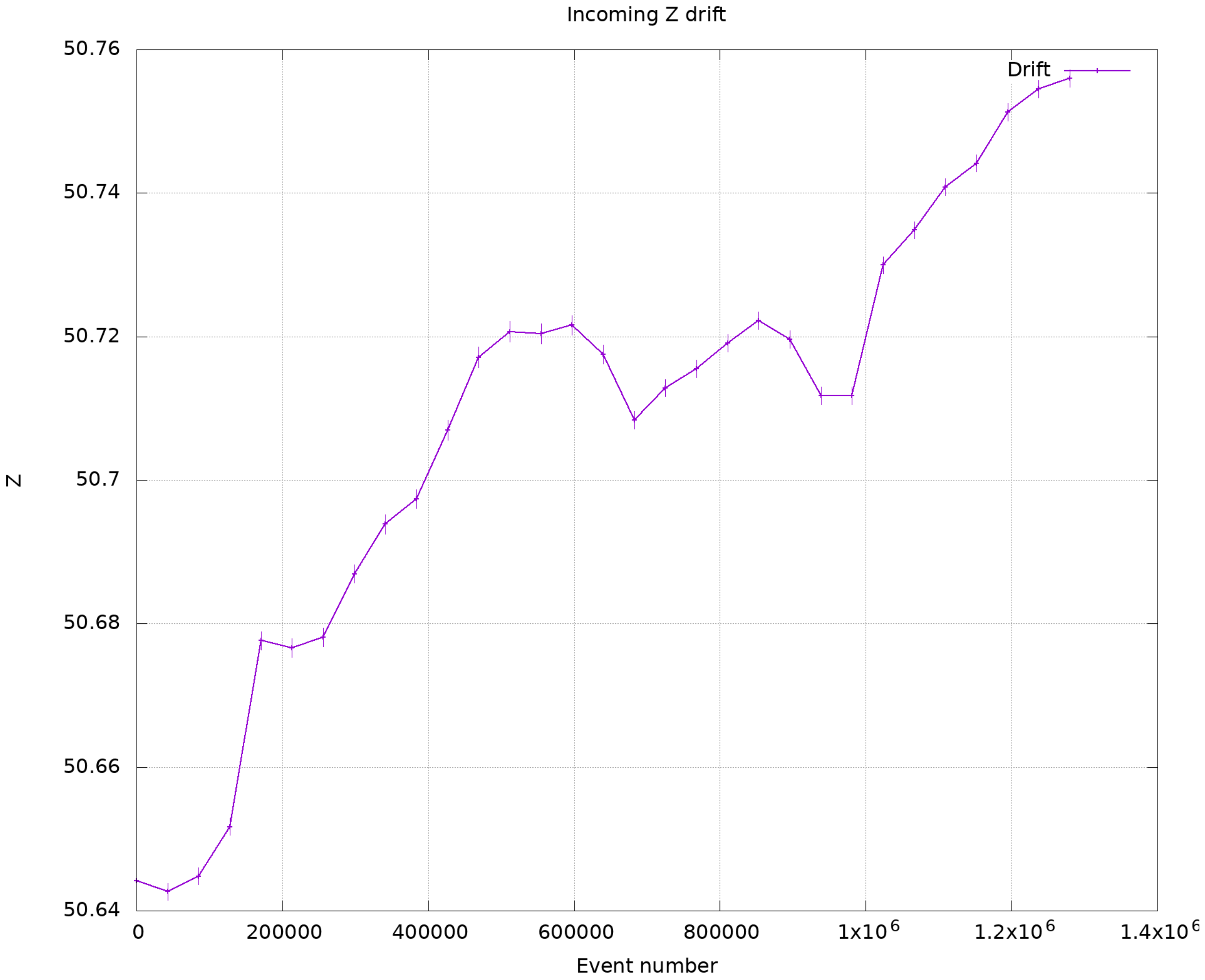

Figure 2.12: This plot shows the drift of the charge reported by Land02 for what would Tin 132. A moving window 50 thousands events wide and partly overlapping with its neighbours is fitted to a Gaussian distribution; for the sample size used, this procedure is applied 31 times. It is evident that during the runs examined there is a drift and this does not show particular discontinuities, indicating that it does not depend from the run number but rather from the time passed from the last setting of the detector. To correct each event, this curve is interpolated and read out at the event index.

Finally, an interpolation of the sampled correction is produced and that is used to correct every event in the set.

Such a procedure removes the offset and also should catch and remove every eventual drifts in the detectors that may not be taken into account by the unpacker. It may also slightly improve the accuracy in selecting the interesting isotope, since one effect it has it to have blobs with a shape closer to an ellipse, which in turn are easier to treat than more irregular ones.
Once the correction is applied, a 2σ cut in both Z and $\frac{A}{Z}$ is applied to select the ions of interest.

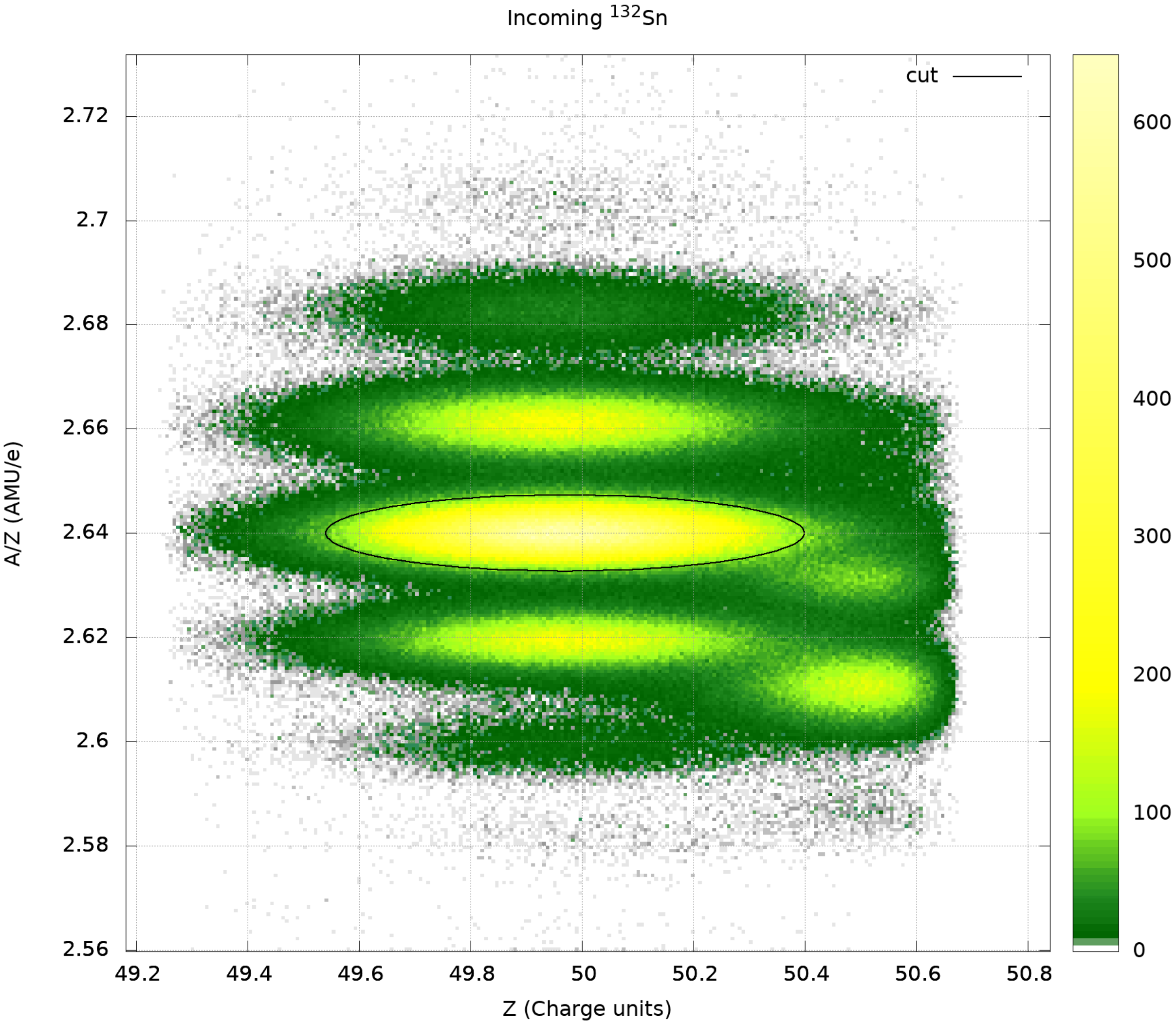

Figure 2.13: This “heat map” shows the density of events in the isotope identification plane, alongside the 2σ cut selecting ^{132}Sn as incoming isotope. The *colouring* here is logarithmic to better “illuminate” the distribution of the event density.

2.3.3 Outgoing fragment

After the target, all the fragments must be collected and identified to have a complete picture the reaction that happened, if any did.

As mentioned before, this work concentrates on the de-excitation of ^{132}Sn from 0[1] to the neutron separation threshold $S_n = 7.34$ MeV due to Coulomb excitation of the nucleus. This means that the nucleus must stay intact and all the energy should be released by gamma decay.

A consequence of the nucleus staying intact is that there will be just one hit in the NTF and both it and PSP3 should report the same charge. The mass of the ion, calculated from the trajectory the nucleus followed through ALADIN’s magnetic field and the reported charge, must also stay the same as the one reported by the FRS. Additionally, no neutron must be present

---

[1] Nearly.

in LAND.

Charge selection To select on the charge of the outgoing fragment, the information from before the target, PSP3 and the NTF are combined.

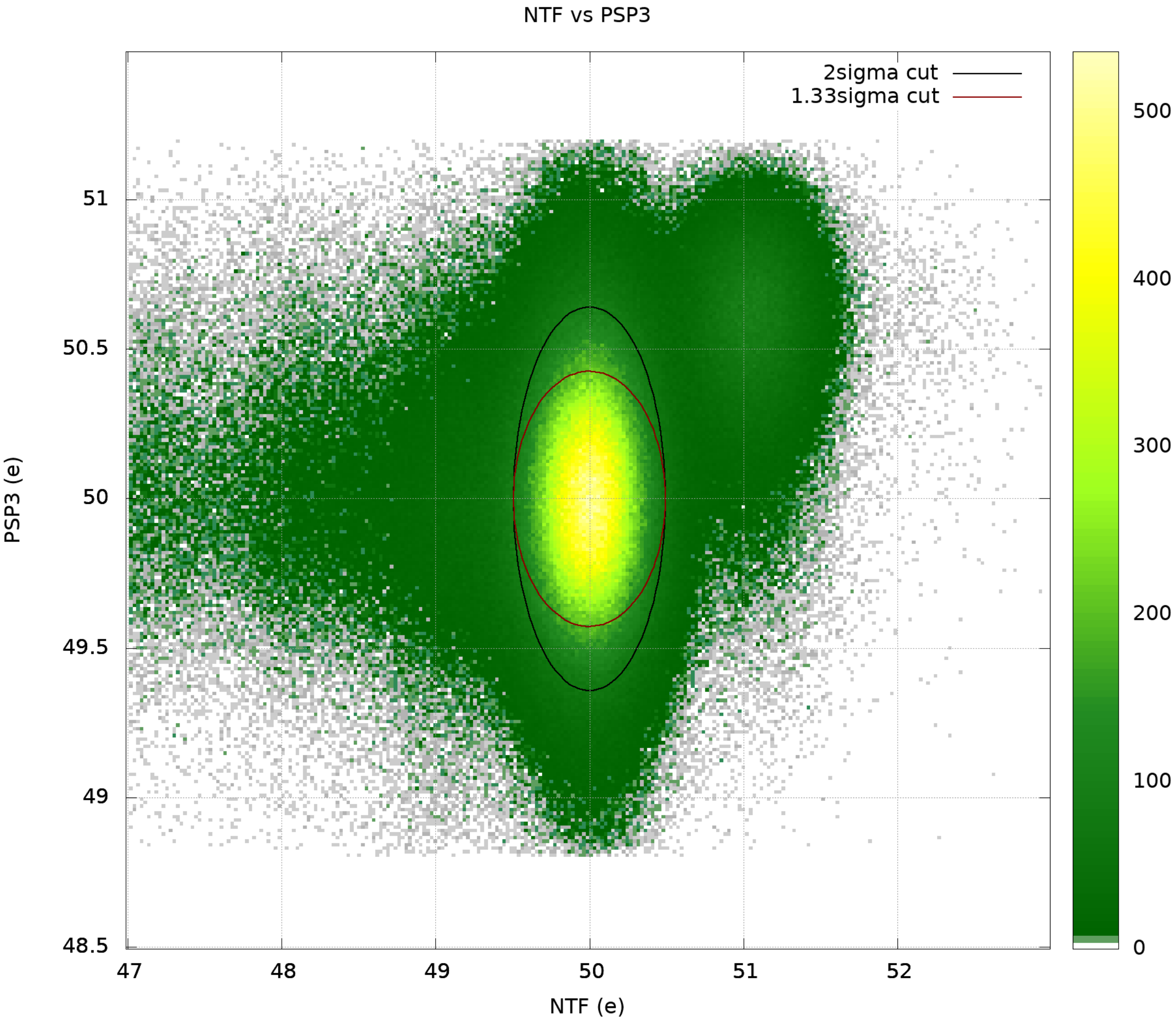

Figure 2.14: This density plot illustrates the distribution of events as seen by the NTF and the PSP3: they both report the charge of the interacting particle. While the black line denotes a 2σ, 2σ cut obtained by fitting the charge distribution reported by each detector, the dark red one is restricted to 1.33σ on the PSP3 reading. This because, observing the spectrum of the detector, it appears to have two peaks –observation that is confirmed by this density plot. Nonetheless, when the information from the PSP3 is combined with the NTF, the second peak is clearly due to another, well separated isotope.

We are interested in Tin staying Tin, so a $(2\sigma, 1.33\sigma)$ cut is applied around (50, 50).
The calibration of the NTF is not a trivial challenge, mostly due to the age and consequent

radiation damage of the detector. It has not been done in the scope of this work and the essential contribution of A. Horvat in this respect shall be noted.

Mass The mass of the fragment can be calculated in a number of ways; in this work, the method known as "ion optics", implemented in the `tracker` coded by R. Plag [PlagTRK]. Once the mass of the outgoing fragment is known, a cut on it can be applied to select outgoing fragments with mass 132.

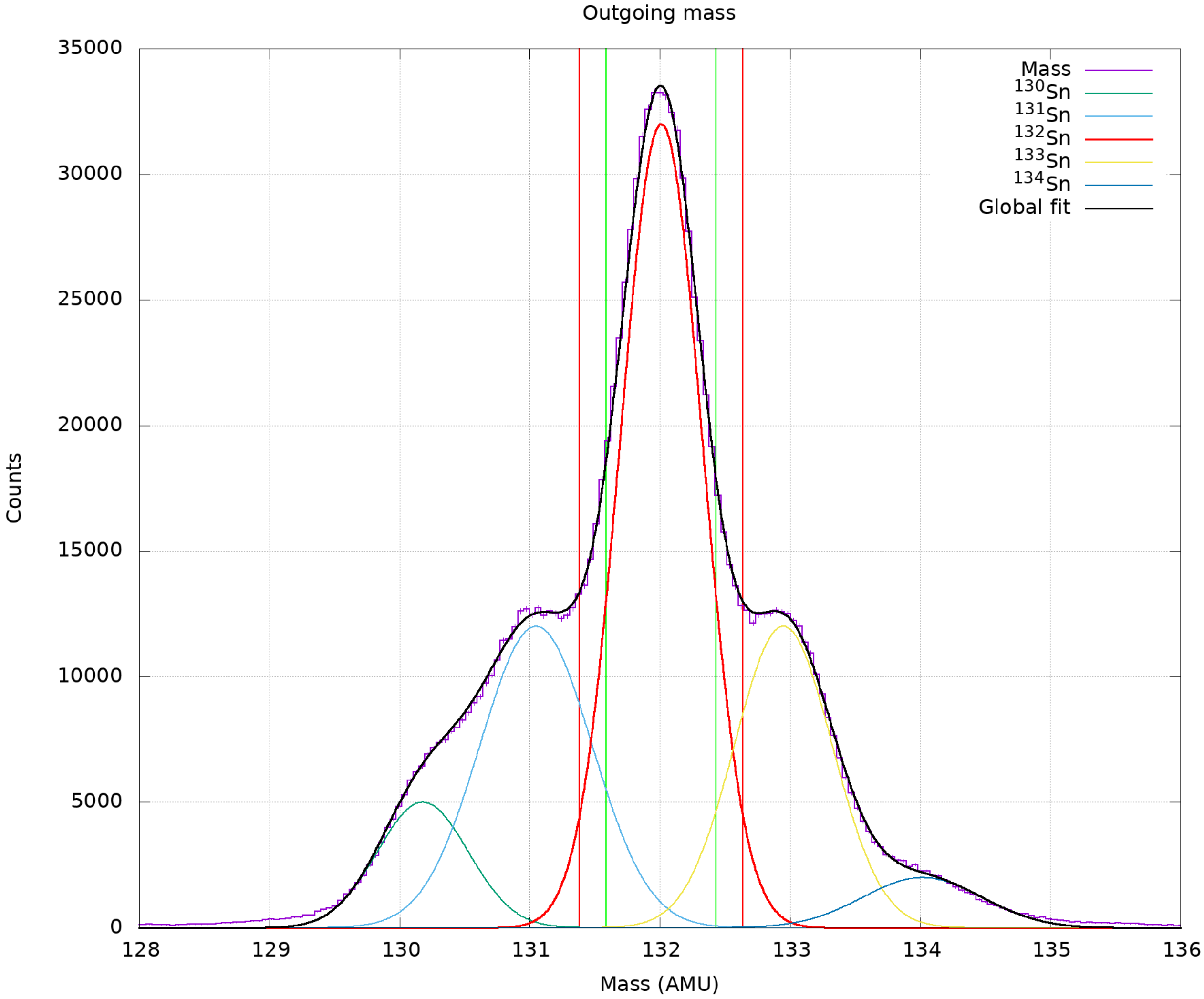

Figure 2.15: This is the outgoing mass spectrum of the fragments, complete with fits for all discernible peaks. The vertical lines in *red* represent a 2σcut around the fitted ^{132}Sn mass peak, whereas the *green* ones represent a cut of 1.33σ. Such a narrow cut is used to reduce as much as possible contamination from neighbouring isotopes, which can false the energy spectrum considerably –very few counts from ^{132}Sn are expected. The resolution for the central peak, relative to ^{132}Sn, is $\frac{\Delta M}{M} = 0.6\%$, with a FWHM of 0.74 AMU.

Because there is significant overlap between the mass peaks, it is a good idea to restrict the cut to 1.33σ instead of the usual 2. This choice is motivated by the need of excluding as much as possible the channel $^{133}\mathrm{Sn} \rightarrow {}^{132}\mathrm{Sn} + \mathrm{n} + \gamma$, where that photon comes from the de-excitation of the 2^+ state of the newly born ^{132}Sn nucleus and the neutron is not detected, which is not such a rare eventuality when compared with the extremely low statistics expected for the 2^+ state of $^{132}\mathrm{Sn} \rightarrow {}^{132}\mathrm{Sn} + \gamma$.

2.4 Data preparation

2.4.1 Front and back of the Crystal Ball

As already mentioned here and there, for this experiment it is advantageous to divide the Crystal Ball into two domains, the front and the back:

FRONT This is the part of the Crystal Ball that looks the beam "in the face" when it enters the target region. I'm defining it as the **neighbourhood up to the fifth order** of crystal 81 (which is not installed, as it is the beam out port).

BACK This is, quite simply, the set of all crystals that are not in the front of the Crystal Ball.

A depiction of this concept is shown in Figure 2.17.

Front vs. back The amount of information that can be found in either half of the Crystal Ball is very different: simulations have shown that the large majority of the photons from the ions will be detected in the front: 83% of all the photons emitted by in flight by the ions will be detected in the front of the detector. The back thus, will carry little physical information and, to the cost of a somewhat reduced efficiency, it is ignored when it will come to the calculation of α_D.
This situation is illustrated in figure 2.16: it is a result of a simulation of 10^5 events containing one single photon, which is emitted in a random direction in the Ion's frame of reference and then Doppler shifted according to a beam energy representative of the dataset I'm going to analyse for this work: 512 aMeV.
It is easy to notice that, as stated before, the majority of the photons will travel broadly in the same direction of the beam and strike the Crystal Ball in the region I'm defining as front.

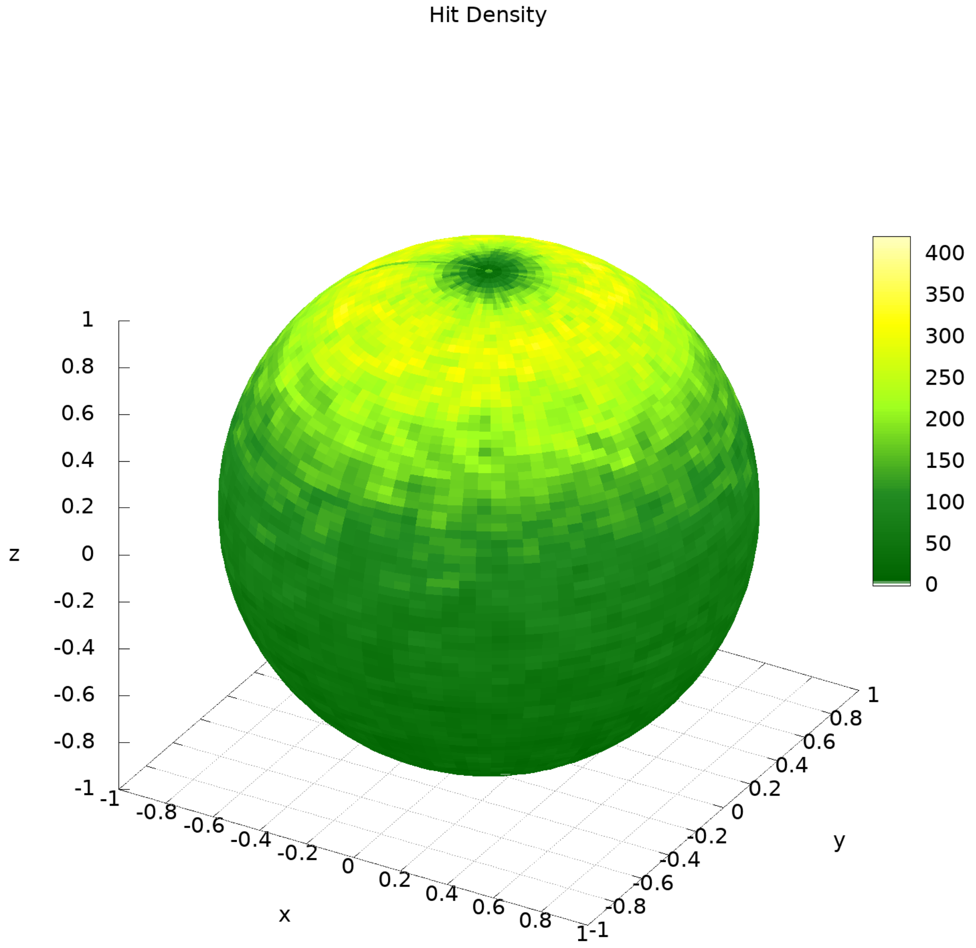

Figure 2.16: This “heat map” represents the density of photons around the solid angle. The generated particles are 10^5 and each angular dimension is divided 100 fold. As can be easily noticed, the photons concentrate around the beam axis and part of the solid angle covered by the front of the Crystal Ball receives by far the largest illumination.
The beam direction is along the z axis and it travels toward the positive values. The axes’ units are arbitrary (you are looking at a density map of the orientation of the photons’ momenta versors).

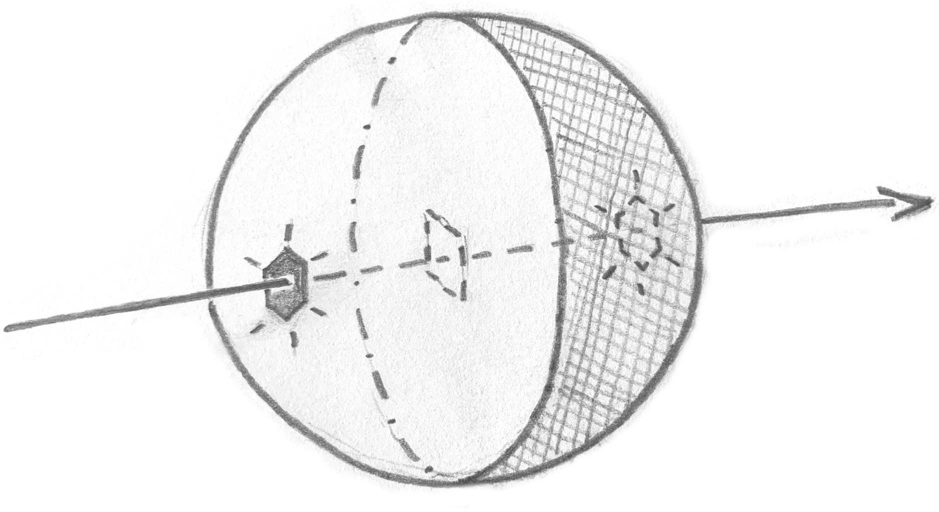

Figure 2.17: This artwork illustrates which are the domains of the front and back of the Crystal Ball: the shaded part covers roughly the region which in this work is referred as "the front", whereas the rest is "the back". The arrow represent the beam axis and direction. At the centre of the detector, not to scale, the square represents the target.

2.4.2 Crystal thresholds

Every single module of the Crystal Ball has its own energy threshold, implemented in hardware before the main DAQ takes over. Because the illumination of each crystal differs, these threshold also differ from crystal to crystal; for example, the crystals in the front of the detector have their thresholds set to around 300 keV: photons coming from the ions at such acute angles with respect to the beam line would be extremely blue shifted, thus one can be quite liberal with the threshold and obtain a good background suppression.

On the other hand, crystals in the back of the detector and still close to the beam line have thresholds typically in the order of 70 keV: photons from the ions in this case would be significantly red shifted and, thus, a higher threshold would reduce the efficiency of the detector[1].

These thresholds are easily deduced[2] by taking a simple spectrum of each crystal and see where it terminates at low energies –this termination can be defined with various levels of sophistication, but in this work it is set simply were there are no more than 5 counts any more for any

---

[1] Which is reduced nevertheless, and more, by not considering the back of the detector at all.

[2] Deducing from the data is usually way easier and more robust than looking for a piece of documentation and trusting it.

lower energy[1] .

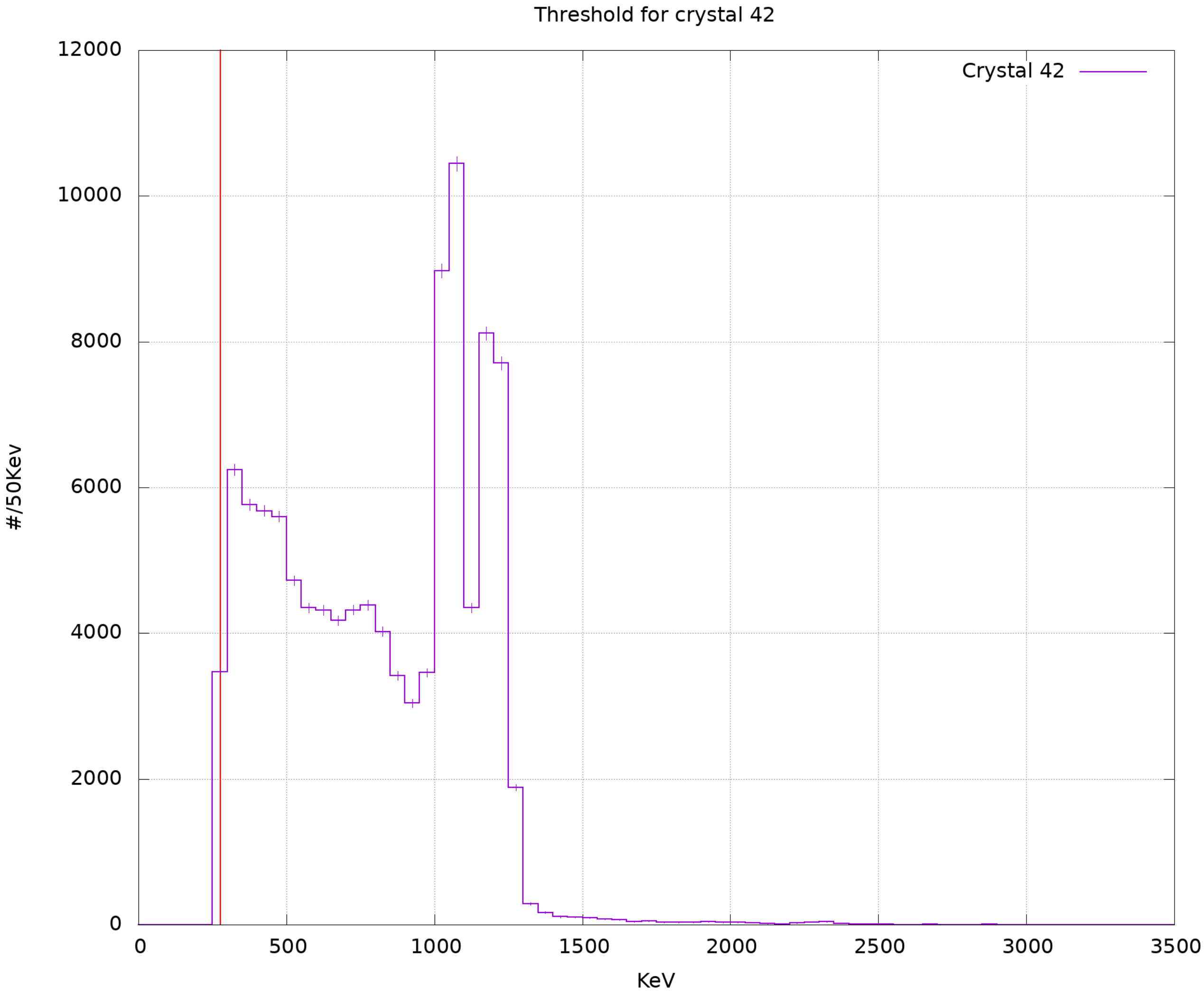

Figure 2.18: An example of a spectrum for a crystal, the number 42, and how the threshold is then determined. The red line in the plot denotes this threshold. Note that this spectrum has been taken from a source run, although it is not necessary to use a source run to determine the thresholds.

A table with all the retrieved thresholds can be found in appendix C; these thresholds are required to ensure that the simulations are correct.

2.4.3 Empty target contributions

Finally, another aspect should be taken into account is the background due to the beam being present, the detectors being on and all other external sources. To investigate this, some data

---

[1] One may be tempted to just take the minimum energy of the spectrum, but this is not a subtle enough approach as it would grossly underestimate the threshold.

acquisition runs *without* a target have been taken: these are then used to build a model for the empty target contribution, which is expected to be there regardless.
First of all, since the incoming isotope identification is independent from having a target in the beam line, the same set of corrections and cuts are applied to select the incoming ion species. Then, one has to properly normalize the number of events. One way to do so is to compare the number of events in the NTF: given the experimental setup, if the target is empty and the incoming ion is not rejected by the ”good beam” condition, it will strike the NTF detector. To normalize the number of events, then, one can require the same number of events in the NTF for both datasets.

Fitting the background and using a generating function

Thankfully, the empty target contribution is not dominant and, thus, the number of hits in the Crystal Ball generated by having just the beam is not large. This, though, results in a very coarse spectrum and when this is scaled up to match the number of events found in the dataset being analysed, very large fluctuations are present and it’s not infrequent to have bins with negative counts once the empty target contribution is subtracted to the data. This is undesirable, so I have chosen to fit the empty target contribution with a double decaying exponential. This has no particular foundation in theory, but it does reproduce the empty target signal well. With this model, it is possible to obtain a smoother spectrum and it is in general easier to subtract it from the data without having to contend with histogram bins with a negative count number (rather unphysical, and the solution of forcing the number to zero whenever negative is not particularly elegant).
Because the function maps the real field into itself, whereas it is difficult to obtain a fractional count number in the data, a rounding is also applied before comparison.

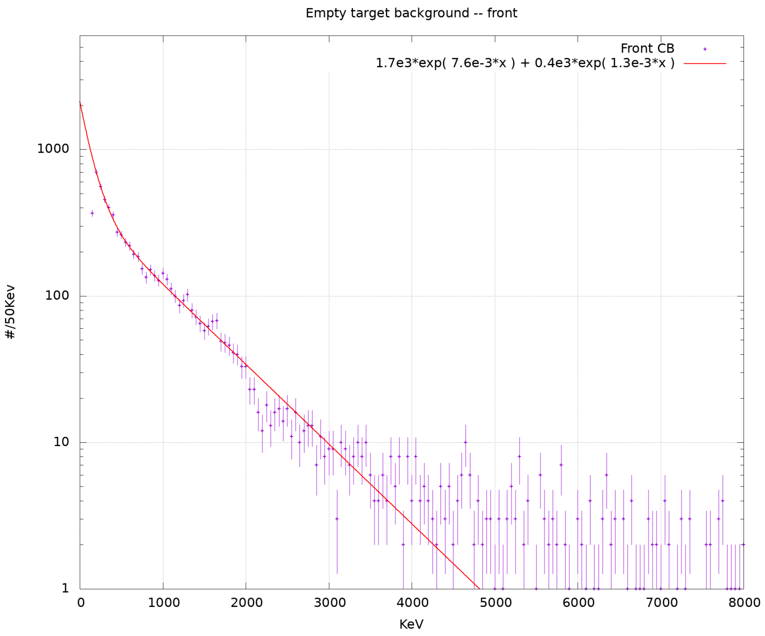

(a) This plot shows the spectrum of the empty target background for the front of the Crystal Ball with the double exponential fit, in red.

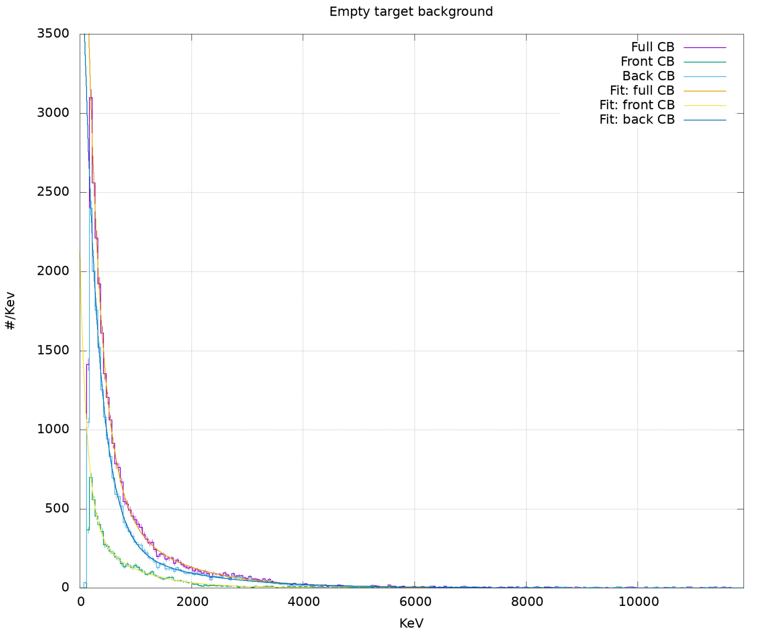

(b) The result of the fit procedure applied to the complete Crystal Ball, only the front and only the back.

Figure 2.19: It is in general possible to model the empty target background, especially at very low and low energies, with a double exponential fit. Furthermore, to select the data sample, the *same* cuts on the isotope identification and the NTF vs PSP3 plane have been applied: this allows for an easier scaling of the sample.

Random coincidences Another aspect that should be taken into account is the occurrence of random coincidences: events that just happen to generate a valid trigger and manage to be recorded despite coming from, for example, cosmic rays.

The usual approach to estimate the number of events that have this origin in a sample is based on the timing; in this case, though, the timing of the Crystal Ball proved to be not completely reliable. A workaround is nevertheless possible, by not imposing any constraint (or, rather, the *same* constraints, due to the DAQ) on the timing of the empty target contribution and consider that as a reference.

This approach is in general less preferred because, for example, would miss out eventual neutrons produced in the interaction of the ions with the target that would be caught by examining a reliable timing spectrum, but it should be reliable when the estimation of random coincidences due to cosmic rays and environmental radioactivity are considered.

2.5 Simulations

An important instrument for this work are simulations: these are used for background subtraction and to obtain a known oscillator strength and photoabsorption cross section distribution to compare with the data and, thus, use to calculate the dipole polarizability.

2.5.1 General setup and `sbkg`

To run the simulations necessary for this work, I developed a program based on GEANT3.21 [GEANT3.21], which is used as the Monte Carlo transport engine, and the ROOT [ROOT] specialization known as R3BRoot [R3BRoot], developed internally by the R^3B working group[1] and which is used to define the geometry of the various detectors and define the magnetic field of the magnet. In a compatible manner, also the geometry of the target chamber, the shielding and the target wheel is imported into GEANT3.21, but not as mainstream part of R3BRoot.

A more technical description of `sbkg`, as the program is called, can be found in appendix E; in less details, this software reads or receives some events in an ASCII format (which has also the advantage of being human readable) common with R3BRoot, manages the memory for large simulations[2], and allows the Monte Carlo transport engine to do its job. The computed data are saved in a R3BRoot format, ready for later analysis.

The usage of a program instead of a ROOT script provides also the opportunity to rely on UNIX-like operating systems' characteristic input and output redirection, which in turn allows

---

[1] Some contributions have also been made in the scope of this work.

[2] Thanks to this program's memory management, all the simulations could be run on a laptop without significant loss of performance per core and without running into memory issues.

for parallel execution of the simulation[1]. Another key difference with the scripts used with ROOT in general is the availability of a configuration file to turn on and off detectors and physical processes that are included in the simulation, thereby making it easier and more straight forward to repeat simulations in the same conditions, and rendering the whole process more transparent to the user.

2.5.2 The atomic background

The most important task for this analysis to succeed is to remove the atomic background. This relatively low energy, high intensity background is due to highly charged ions flying through neutral matter –thus, having a lot of electrons to interact with. This is a known and very well studied phenomenon and, therefore, tools are available to predict the cross section distribution in the angle and energy.
The processes included in the simulations used to reduce the atomic background are[2]:

PB Stands for Primary Bremsstrahlung;

SEB Secondary electron Bremsstrahlung: electrons are knocked off by the energetic ion and receive a considerable kinetic energy, this is then dissipated through the familiar Bremsstrahlung process.

REC_K K-shell radiative electron capture: weakly bound electrons in the medium are captured by the projectile's K-shell while in flight; this process is known to contribute to the continuum X-ray spectrum.

REC_L L-shell radiative electron capture: the same as above, only with the L-shell.

TX Target X-rays, the target's atom get excited and emit their characteristic X-rays.

Most of these processes result in isotropic radiation emission and are at rest in the target frame of reference, with the exception of PB, which predominantly happens in the direction of the beam and it is Doppler shifted.

2.5.3 Event generation and `abkg`

To calculate the cross section for the atomic background with the experimental conditions, the program known as `abkg` has been chosen: it is a very well proven program originally developed at the GSI in the '80s and then revised by Professor H. Scheit, a member of the working group where this work developed.

---

[1] Without the need for re-engineering some of the core features of the R3BRoot package, which was out of the scope of this work.

[2] Indicated in the same way as the tool I have used indicates them.

This program provides (among other things) the distribution of the double differential cross section in the angle and energy, $\frac{d^2\sigma}{dEd\theta}$:

This distribution is then utilized by another program, built on code originally provided by Dr. D. Rossi, to generate the photons that are expected from the atomic background when and ion flies through the target.

2.5.4 Experimental condition for the atomic background

Because one of the objectives of this work is to see through the atomic background, which contributes hundreds of thousands of counts over mere tens generated by the physics, an excellent control over the conditions used for the simulation is essential. The objective is to have a simulation that does not require any further normalization at all when compared with the data, so that the level of arbitrariety in the process can be kept to a minimum and, thus, what will be observed can be confidently regarded as physics.

Beam energy A crucial quantity to determine the cross section for the atomic background is the beam energy to be utilized. The `abkg` program can calculate the cross section at a single energy, whereas in reality the beam is not exactly monochromatic, thus a distribution of energies would be best suited for the comparison.

Modifying working and well proven code is not necessarily a good idea, therefore I settled for additional processing after `abkg`. First of all, the incoming energy distribution for the beam, both at the entrance of the experimental setup and in the middle of the target, needed to be determined; both quantities are available either from the unpacker or the tracker, and those have been used.

Once that has been obtained, `abkg` has been put to work on energies from the maximum (found in the incoming beam) to the minimum (after large deposits in the target) with a stride of 3 MeV and, then, these datasets have been passed on to the simulation software.

The spectra obtained in this way can be then compared to the data obtained during the acquisition runs with the target of interest: the energy distribution obtained from Land02 and the tracker is used to weight a sum of all the spectra; each bin weights the spectra at the energy it refers to, after the beam energy spectrum is normalized by the number of events.

It has been found, not in complete agreement with the lore surrounding the comparison between this kind of simulations with the data, that considering the energy of the beam as it is entering the target instead of the energy in the middle of the target tends to reproduce the data better.

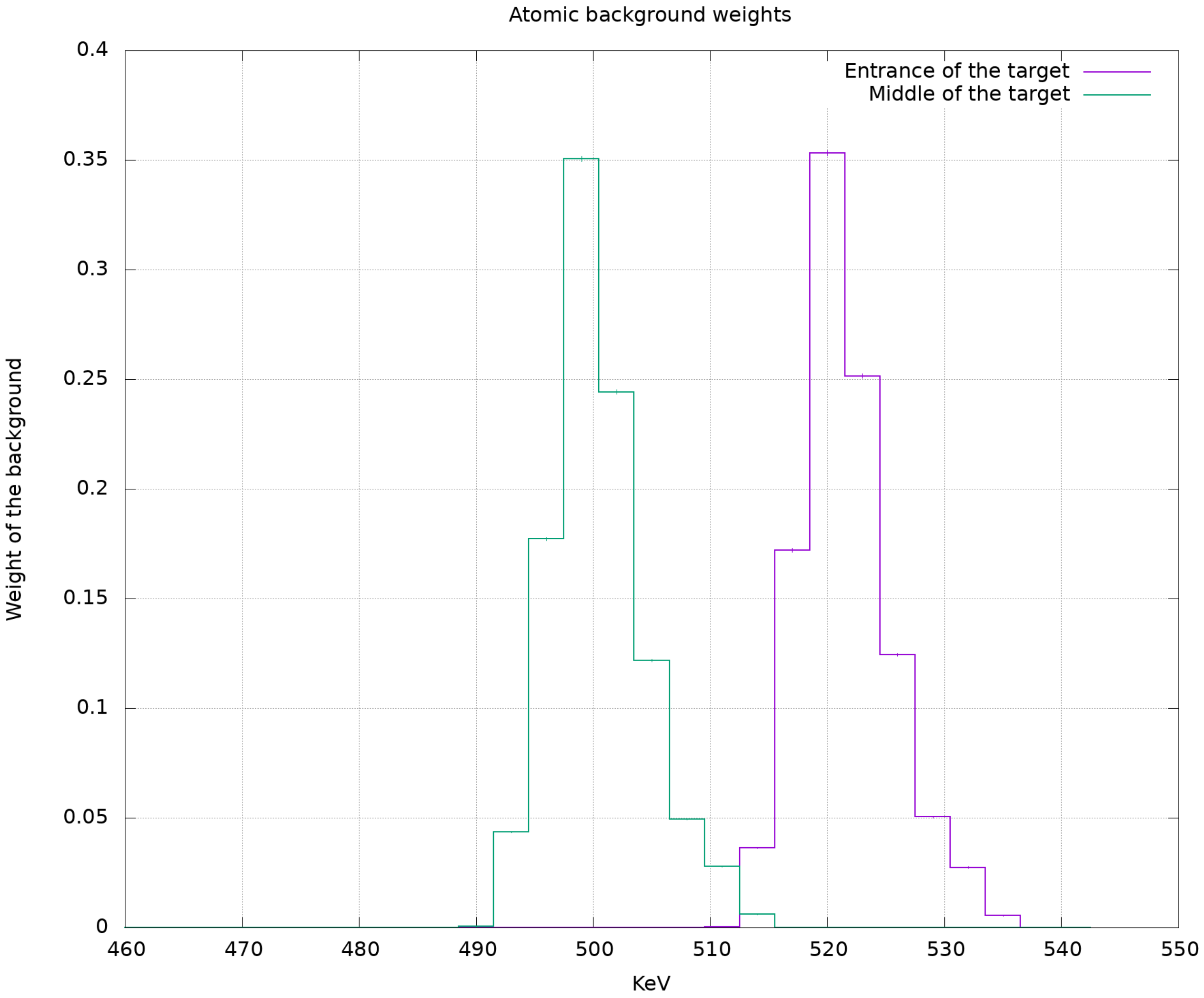

Figure 2.20: This is the distribution of the incoming beam energy and the energy calculated (by Dr. R. Plag's tracker) at the middle of the target. As it is easy at noticing: the energy is shifted by more than the distribution's width, hinting to that effect being significant.

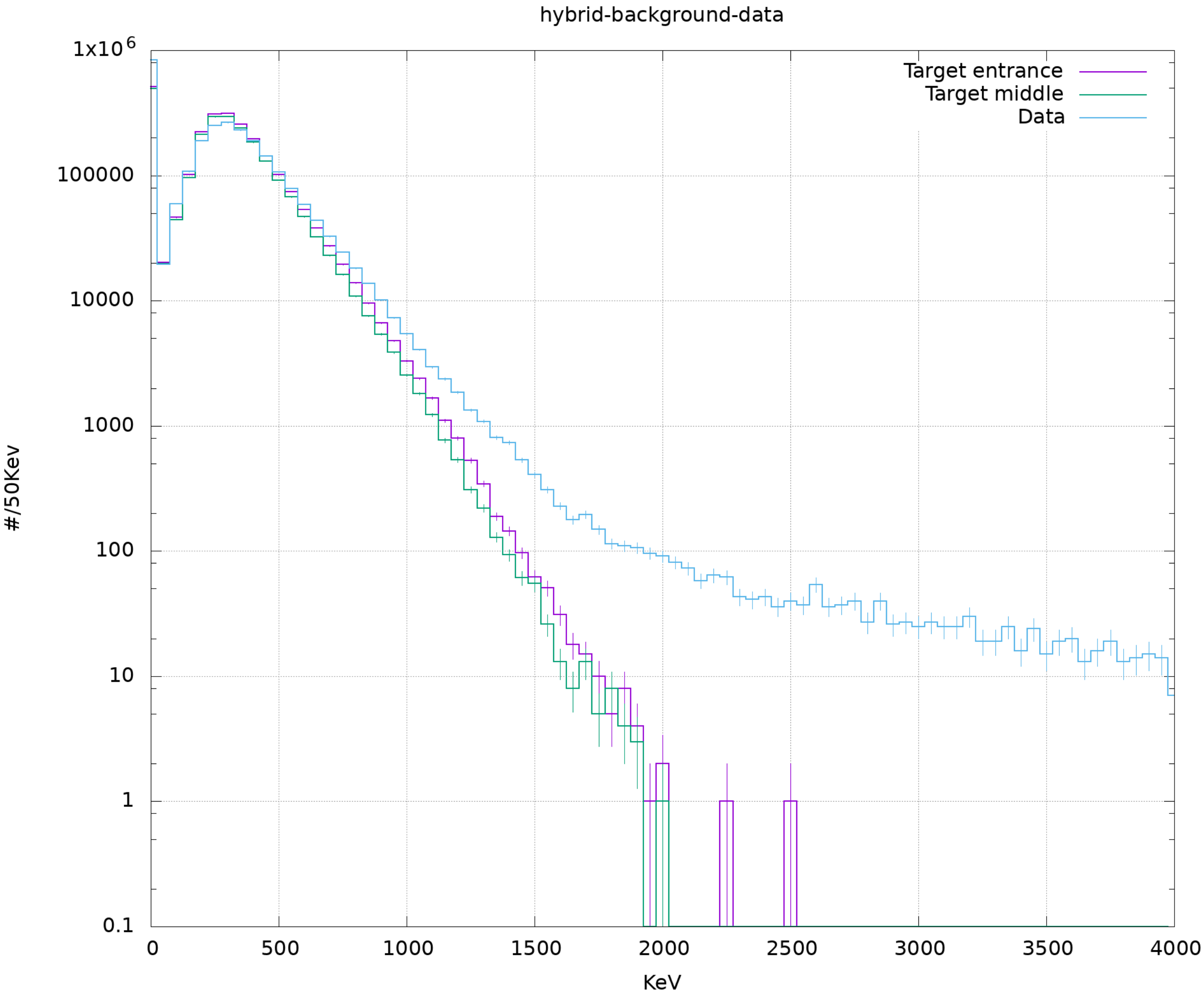

Figure 2.21: Comparison between the background calculated with the energy distribution at the target entrance and the one obtained from the energy distribution at the middle of the target with the experimental data. As one can easily note, the difference is less stark than it could be anticipated by comparing the energy distributions; however, the atomic background calculated from the energy distribution at the target *entrance* is closer to the data. Please note that the data contains more counts because, hopefully, there are also photons coming from the ions and this sample is *not* Doppler corrected, as the vast majority of the background is generated at rest in the laboratory frame of reference.

Excess of hits in the Crystal Ball It is easy at noticing in figure 2.21 that the simulated background does not reproduce completely the data in the region from close to 0 to around 4 MeV: the simulated spectrum has some features at very low energies that cannot be observed in the data[1] but, more strikingly, the slope of the spectra in the background region is not the same. This points to an excess of counts in the data with respect to the simulation.
More details can be obtained by comparing only the front and the back part of the Crystal Ball: it is apparent that the excess counts are mostly where they should be, that is to say *in the front*.

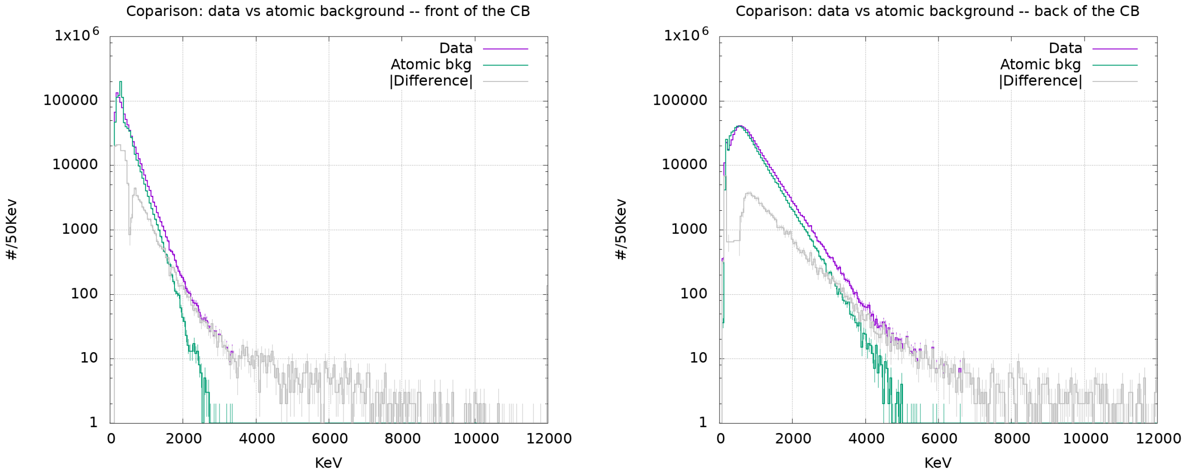

(a) Comparison for the front of the Crystal ball.

(b) Comparison for the back of the Crystal Ball.

Figure 2.22: These plots illustrates how the atomic background compares with the data. As expected, there is more in the data than just atomic background, and there is more of if in the front of the Crystal Ball than in the back. These sets of event have been clustered and Doppler-corrected, fact that is evident because the atomic background in the second plot is considerably blue-shifted.

What the composition of this excess hits is will be one of the main focusses of this work and the investigation can be found in the following.

2.6 The whole background picture

Of course, nothing outside physics happens in the target and what is background and what is not is a matter of definition, informed by the experimental interest. From now on, "background"

---

[1] Threshold effects: although the thresholds for every single crystal are applied to the simulation as well, the behaviour of a software cut is slightly different than one implemented by a piece of electronics, which is affected by a resolution. This may account for some of this discrepancies. Another possible source for this is simply some non completely linear sensitivity of the detector modules in that region, which would smooth out some spectral features.

will indicate the sum of the atomic background and the appropriately scaled spectrum obtained from the empty target runs. For reference, this is the background spectrum and the comparison with the data.

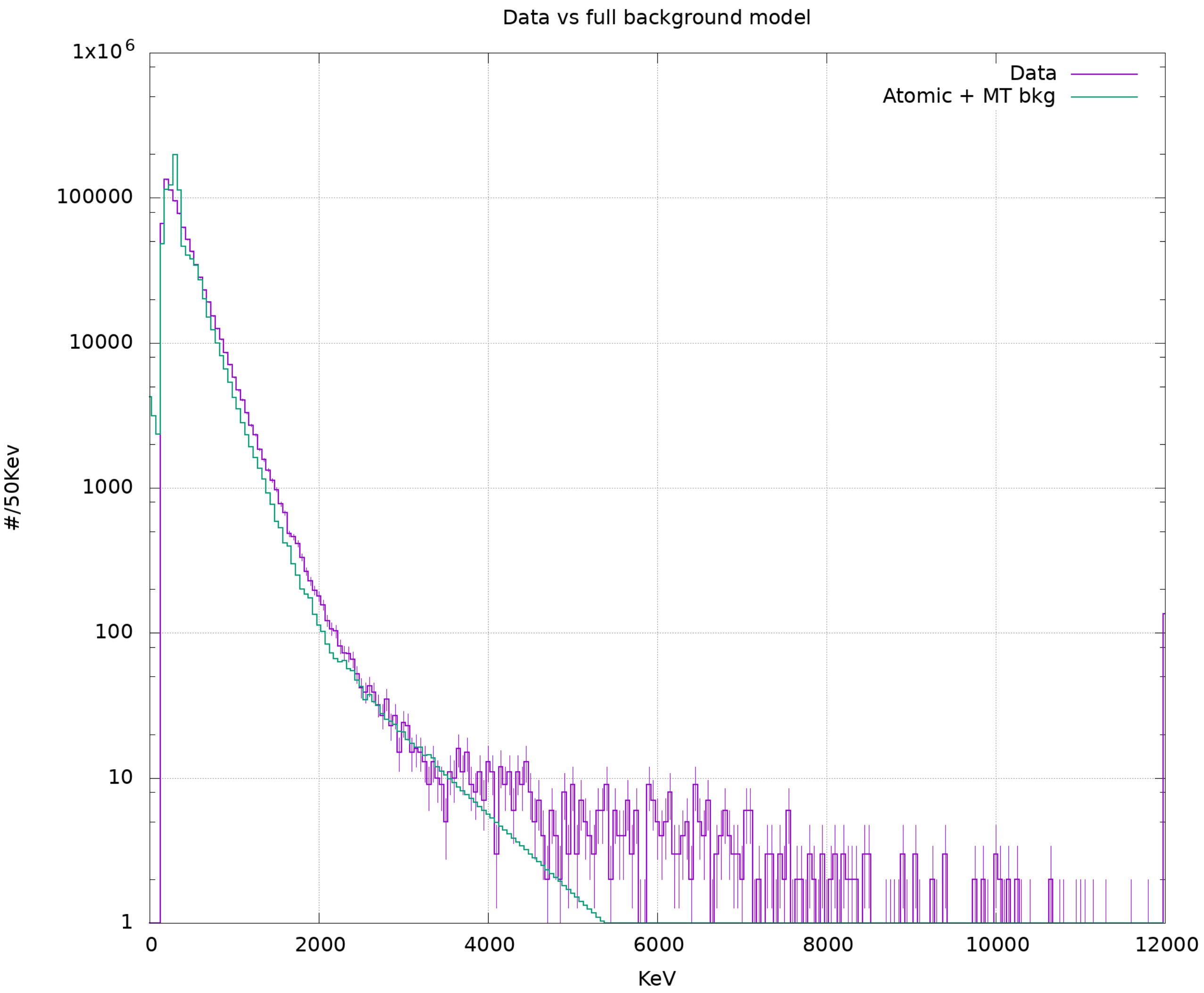

Figure 2.23: The data compared with what is *defined* to be the background in this work. The counts in the first two bins of the histogram for the background are due to the empty target model, which is a function and is defined for all real numbers.

2.7 Calculations

Once the event selection has been worked out and performed, it becomes possible to obtain and calculate some observables.

2.7.1 Cut efficiency, specificity and uncertainties

As discussed above, the selection of the reaction channel happens by virtue of cuts applied to the dataset. These cuts are in general an ellipsoid in the space where they are applied: they assume naturally that shape because, for each dimension, events tend to accumulate according to a Gaussian distribution[1].

To reach an accurate estimate of the reaction probability and, then, of the cross sections involved, it is necessary to know how many events would give raise to the observed number within the cut. Furthermore, of course, all these quantities come with an uncertainty and this propagates to all the conclusions based on them.

Cut efficiency. The cut efficiency ϵ_{cut} is the fraction of the events from a given channel that are selected by the cut applied to that channel. All the cuts that I employed in this analysis are *independent* from each other; this means that they are all applied to the starting sample without any prior cut and, furthermore, they don't assume or necessitate any previous cut being applied in order to work properly. This choice makes the efficiency estimation easier, since the global efficiency will be the product of all the single efficiencies.

cut	**description**	**efficiency**
Incoming isotope ID	2σ on Z, 2σ on $\frac{\text{A}}{\text{Z}}$	0.84
Outgoing vs. incoming charge	2σ out, 1.33σ in	0.72
Mass	1.33σ on the mass	0.94
CB half	front half of the CB	0.84

Table 2.2: This table groups the efficiencies for all the cuts applied for the reaction channel selection. I have included the efficiency loss due to considering only one half of the CB: although this is not an elliptical cut, it does carry an efficiency with itself. This has been estimated with a Monte Carlo simulation (see previous sections for a more detailed discussion).

Cut specificity. Obviously, the interesting reaction channel is not alone, there will be contaminations from the neighbouring ones. The amount of this contamination is taken into account here and is called the specificity of the cut: it's the ratio between the number of events that are expected to be the kind that is being selected and the events that are selected despite coming from something other process –just sitting on the tails of the respective Gaussian distributions.

More formally, this quantity can be expressed by:

$$\xi_{\text{cut}} = \frac{\int_\Omega f_{\text{interesting}}(\vec{x})d\vec{x}}{\sum \int_\Omega f(\vec{x})d\vec{x}} \tag{2.2}$$

---

[1] At least, if the detectors were ideal or perfectly corrected; in the real world, there could be some hits of exponential tails attached to these gaussians (in CERN's jargon, this function is indicated as "crystalball", I believe). In general, though, these effects have not been observed for these dataset, as a testimony to the goodness of our detectors and analysts.

Where ξ_{cut} is the subject of this paragraph, $f(\vec{x})$ is a multivariate Gaussian distribution[1] with a footer that denotes its interestingness and Ω is the region comprised by the cut.
These integrals are to be solved numerically, in the case of this work with the Monte Carlo method.

cut	**specificity**
Incoming Isotope ID	0.994
Outgoing vs. Incoming charge	0.71
Mass	0.97

Table 2.3: The calculated specificities for the cuts. Please see table 2.2 for the descriptions: they are always the same. In this case, the specificity of the cut on the front of the Crystal Ball is not reported: it amounts to the same as comparing the atomic background simulation plus empty target noise with the data, something that is discussed elsewhere.

The part this quantity plays is, together with the cut efficiencies, in determining essentially a multiplicative factor with which to scale the number of events inside the cut to obtain a reliable number of event effectively happening for the selected reaction channel.

Cut uncertainty. In table 2.2 is given the width of the cut along a particular axis in terms of the number of σ's that cut spans. This is subtended by the assumption, already mentioned, that the events distribute normally along every axis; this means that it is also easy (usually) to fit their distribution and, thus, have an error estimate on the parameters of the event's distribution, including the width.
In relative terms, then, the uncertainties on efficiency and specificity for each cut are:

cut	**δ on efficiency**	**δ on specificity**
incoming isotope ID	7%	7%
Outgoing vs. Incoming charge	2%	2%
Mass	0.12%	0.2%
CB half	0.02%	–

Table 2.4: The relative errors on the efficiency and specificity. These errors are estimated numerically starting from the uncertainties associated to the fit, except for the cut on the CB half, where the uncertainty is assumed to be the square root of the number of events counted.

2.7.2 Reaction probability

The reaction probability describes, quite simply, how many of the incoming ions interact and populate one reaction channel. In the most simple form, this is given by the number of events

---

[1] In this work, the most variables that we'll ever encounter is 2.

that belong to a channel divided by the number of total events: $\frac{N_{ch}}{N_{total}}$, where the number of total event is defined as the all the events that are considered valid. This condition, in the case of this experiment, would correspond to all the events that triggered with `POS!ROLU`.

In the case of this experiment, though, one has to consider the effects that might arise from the "downscaling": the "good beam" trigger has a downscaling factor of 3, meaning that only one out of eight events will be recorded if left to its own devices –and, indeed, making sure that only around one event in eight has `POS!ROLU` is an important test to run; if a good beam trigger is generated alongside with another one which is *not* downscaled (either because it is not set as such or because it so happens that at that particular moment the DAQ would register the trigger), the event is saved nevertheless.

Once these cases are considered, it appears clear that if a condition on the trigger matrix is also applied to identify the reaction channel and within that condition there is a downscaling included, the comparison has to be performed with only events that have an explicitly set flag *and then* multiplied by the set downscaling.

In the case of this work, neither the trigger `XB_OR` nor the sum condition `XB_SUM`[1] are downscaled[2], therefore it is possible to rely solely on the conditions on the single detectors.

The trigger flag distributions for the entire dataset are:

```
UNSET.......:                           |         0
POS_NOT_ROLU:+++                        |    160324
PNR_PUP.....:+++                        |    160393
FRAG........:++++++++++++++++++++++++   |   1279237
LAND........:+                          |     33498
FRAG_XB_SUMF:+++++                      |    276282
FRAG_XB_SUM.:+++++++++++++              |    708838
FRAG_XB_OR..:                           |     19865
PIX.........:                           |         0
```

Where the total events are 1279276. When all the cuts are applied, the trigger statistics for the 285959 selected events they become:

```
UNSET.......:                           |         0
POS_NOT_ROLU:+++                        |     35716
PNR_PUP.....:+++                        |     35727
FRAG........:++++++++++++++++++++++++   |    285959
LAND........:                           |      2656
FRAG_XB_SUMF:+++++                      |     58802
```

---

[1] This flag is set when the readout value of all the crystals in the Crystal Ball sums to a value greater than a certain threshold. Note that this happen *before calibration*.

[2] Yet another private communication.

```
FRAG_XB_SUM.:+++++++++++++            |     154851
FRAG_XB_OR..:                         |       4540
PIX.........:                         |          0
```

As expected, the relative trigger proportions are largely unvaried, with the exception of LAND, which is actively selected against to avoid neutrons[1].

The reaction probability for ^{132}Sn $\rightarrow^{132}$Sn $+ n\gamma$ is 0.46 ± 0.07, already corrected for efficiency and specificity of all the cuts, after selecting the reaction channel as described in the sections above, and calculated from a set which comprises all the events that have a valid "good beam" trigger[2].

2.7.3 Cross section

It is possible to derive the cross section from the reaction probability by including the information on the material density. Namely, the cross section is proportional to the number of targets in the material where the beam impinges, which equals $\frac{m_{mol}}{\rho_t N_a}$, where m_{mol} is the molar mass, ρ_t is the target thickness and N_a is the Avogadro's constant. The cross section thus becomes:

$$\sigma = r_p \frac{m_{mol}}{\rho_t N_a}. \tag{2.3}$$

Nuclear reactions In general, there can be competing nuclear reactions with the process of interest happening in the target. To reduce this contribution, one can examine the data acquired with a different target: in the case of this experiment, Carbon targets have been used; Carbon offers a very low cross section for Coulomb excitation because it is very light compared to the projectiles, neutron rich Tin isotopes[3]. In the specific case of this work, because a fundamental selection condition for the reaction channel is that the projectile conserves both mass and charge numbers, nuclear reactions that result in nuclear disintegration of any sort should already be excluded. The remaining contribution comes from inelastic nuclear scattering mediated by the strong force, which may offer a non-zero cross section at the energies of interest. Nonetheless, its contribution is expected to be at least small.

The cross section for nuclear reaction for ^{132}Sn impinging on ^{208}Pb can be estimated [Bor95] with the formula:

$$\alpha_{\mathrm{Pb}} = \frac{\sigma_{\mathrm{Pb}}^{\mathrm{nuclear}}}{\sigma_{\mathrm{C}}} = \frac{1 + a \cdot A_{\mathrm{Pb}}^{\frac{1}{3}}}{1 + a \cdot A_{\mathrm{C}}^{\frac{1}{3}}} \tag{2.4}$$

---

[1] Not all LAND triggers are neutrons: the selection criterion is a bit more nuanced and is explained in [Hor19] and [Sch15] and also takes into account the neutron velocity; the criterion used here is the same, NOT-ed.

[2] The sample size of "all" events, before the reaction channel selection, is defined as "events that can be successfully tracked", which amounts to roughly $\frac{1}{8}$ of all the events that are on-spill and generate any valid trigger pattern, but they do not necessarily contain enough information to track the ion and fragments.

[3] More details on the calculations are given in the next subsection.

The constant a, according to [Bor95], is $a = 0.14 \pm 0.01$ which, when substituted in the expression 2.4 gives a coefficient α_{Pb} of around 1.4.

To actually run the comparison, one can apply the exact same set of cuts to the data acquired with a Carbon target (in our case, with a thickness of 2.756 g/cm^2) as those utilised for the event selection with a Lead target. Once this is done, it is possible to integrate the cross section obtained between, 2 and 6 MeV photon energy to obtain an estimate of how much the nuclear reactions are contributing to the total cross section observed with the Lead target. The result of this integration is $\sigma_{\mathrm{C}} = (0.036 \pm 0.003)$ b and $\sigma_{\mathrm{Pb}} = (0.74 \pm 0.02)$ b, indicating around 5% of the total cross section observed for Tin impinging on Lead coming from nuclear reactions.

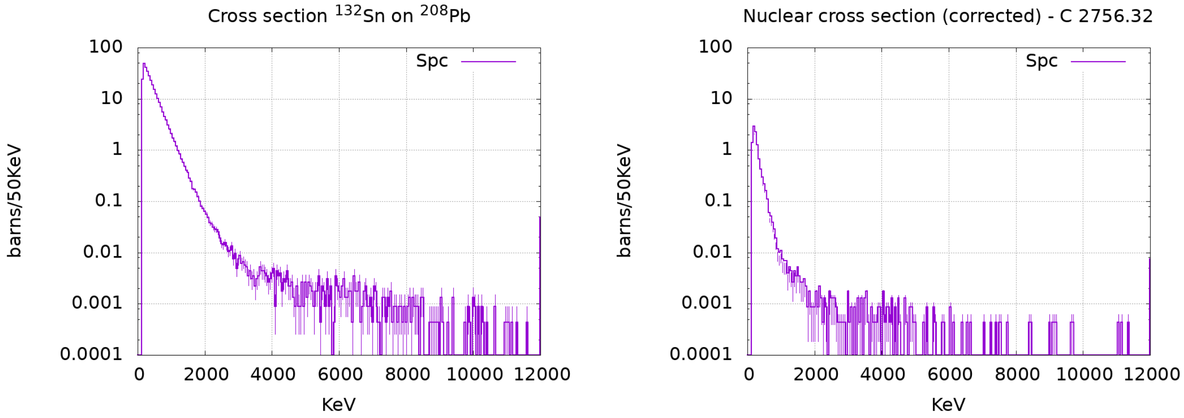

(a) The differential cross section for ^{132}Sn impinging on a Lead target. This comprises the cross section due to Coulomb excitation and, potentially, nuclear reactions. Already corrected for α_{Pb}, see expression 2.4.

(b) The differential cross section for ^{132}Sn impinging on a thick Carbon target. Because Carbon is a light nucleus, it does not offer a significant Coulomb excitatio cross section to Tin.

Figure 2.24: Above the differential cross sections for different targets are shown. It is immediately apparent that Carbon offers a much smaller cross section to Tin than Lead. This is also reflected in the integrated cross section, which turns out to be 5% for Carbon than it is of Lead. Note that in this comparison, because the integration is performed from 2 to 6 MeV, the background is not subtracted; to obtain a comparison also on lower energies, the atomic and empty target background has to be subtracted as well.

2.7.4 Virtual photon number

The idea of describing the nucleus-nucleus interaction as an exchange of virtual photons was first introduced by Weiszker and Williams [Wei34, Wil34] with a semiclassical approach. In that picture, the spectrum of the virtual radiation is defined as the Fourier time-domain integral of the electromagnetic interaction.

The virtual photon method was later revisited by Bertulani and Baur [Ber85], who put it in terms of the plane wave born approximation for calculating the Coulomb excitation cross section. For the total cross section at a given energy, they derive the expression:

$$\sigma(\hbar\omega) = (Z_p\alpha)^2 \sum_m \left(\frac{\omega}{c}\right)^{2(l-1)} g_m(\xi) \left|G_{\pi lm}(\beta)\right|^2 \frac{B(\pi l)}{e^2} \tag{2.5}$$

Where the functions $g_m(\xi)$ and $G_{\pi lm}$ are shorthand notations and their explicit form can be looked up in Bertulani and Baur's paper at equation 3.13b, 2.16a and 2.16b, respectively; ξ is called the *adiabaticity parameter* and, most importantly, the indices π, l and m represent the kind of interaction (electric, magnetic), the angular quantum number and the magnetic quantum number[1].

To obtain the total Coulomb excitation cross section, it is necessary to integrate the electromagnetic cross section over all energies $\epsilon = \hbar\omega$ and sum over the final states while weighting the integral by the density of said states:

$$\sigma_c = \sum_{\lambda\pi} \int \sigma(\epsilon)\rho_{\lambda\pi}(\epsilon) d\epsilon \tag{2.6}$$

The cross section that appears in the integral[2] is the same object that is described by equation 2.5. By using it in equation 2.6, it is possible to separate the contributions from the electric and magnetic contributions (by virtue of how $G_{\pi lm}$ is defined. It is also possible to express the cross section as the product of the photonuclear absorption cross section and an adimensional function of the energy:

$$\sigma_c = \sum_{\lambda\pi} \int \{n_{El}(\omega)\sigma_l^E(\omega) + n_{Ml}(\omega)\sigma_l^M(\omega)\}\rho(\omega)\frac{d\omega}{\omega} \tag{2.7}$$

where

$$\sigma_l^{E,M}(\omega) = \frac{(2\pi)^2(l+1)}{l\left[(2l+1)!!\right]^2} \sum_{\lambda\pi} \rho(\epsilon) k^{2(l-1)} \frac{B(E,Ml)}{e^2} \tag{2.8}$$

is the said photonuclear absorption cross section[3][4] for a given multipolarity l and in function of the angular frequency of the incoming photon (remember that $\epsilon = \hbar\omega$), and

$$n_{\pi l} = Z_P^2 \alpha \frac{l\left[(2l+1)!!\right]^2}{(2\pi)^2(l+1)} \sum_m \left|G_{\pi lm}(\beta)\right|^2 g_m(\xi) \tag{2.9}$$

is the expression for the number of virtual photons exchanged.

---

[1] In the standard nomenclature when these are introduced.

[2] It may not be immediately clear why a sum *and* an integration are both necessary: whereas the integration acts upon the final states, which are expressed as a density, the sum is on the multipolarities: λ denotes the order and π the kind, magnetic or electric.

[3] There is a funny operator in the formula: !! is not the factorial of the factorial, but the *semifactorial* which is defined as $n!! = \prod_{k=0}^{\lceil \frac{n}{2} \rceil - 1}(n-2k)$.

[4] This formula differs from expression 4.3 in [Ber85]: if you observe 3.13a and perform a dimensional test on the formula, you shall find that 3.13a's arrangement is correct, whereas 4.3 does not result in an area. In the calculations for this work, the exact form quoted in equation 2.8 is used.

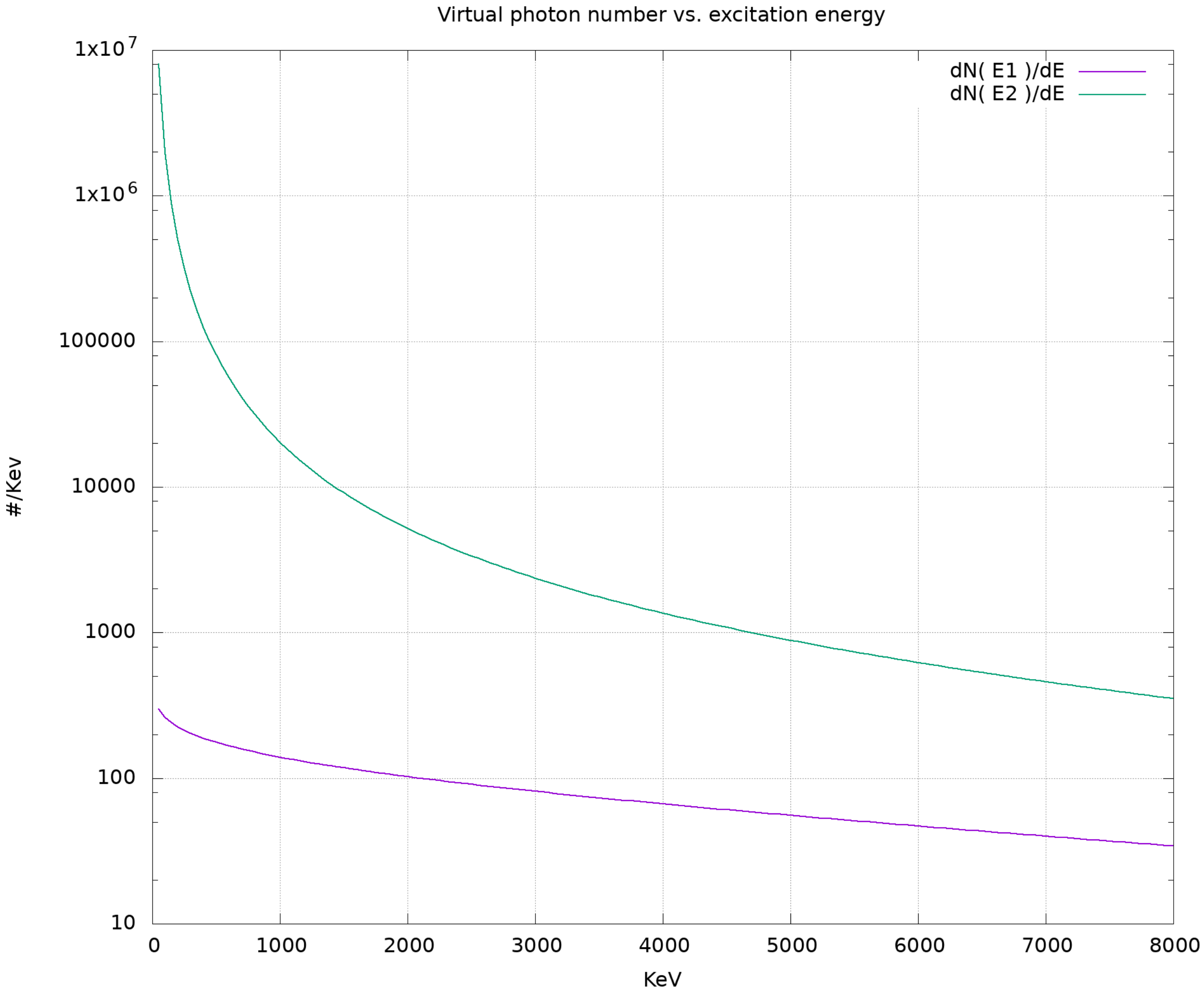

Figure 2.25: This plot illustrates the dependence of the virtual photon number, calculated for E1 and E2 modes, with the excitation energy. Note that, while such a number is vastly superior in absolute terms for E2, the photo absorption cross section for the E2 mode is so much smaller than for the E1 more that, in the end, the Coulomb cross section for E2 turns out to be smaller than for E1.
Another interesting thing to note is that this photon number depends on the beam energy, but it varies slowly enough in the region of interest that a single representative energy can be considered without introducing significant sources of uncertainty: this plot refers to the measured beam energy centroid of around 520 aMeV.

The two plots in figure 2.25 are relative for dipole and quadrupole electric transitions. It is evident that the lower order electric transition actually has a significantly lower number of virtual photons exchanged at a given energy than the other kind. This, however, is not going to be a problem and we'll be able to neglect the magnetic transitions altogether, since the transition probability associated with magnetic transitions is orders of magnitude smaller than for electric transitions [Sto05]. For convenience, here follows the explicit expressions for the E1, E2 and M1 virtual photon spectra:

$$n_{E1} = Z_p^2 \alpha \frac{2}{\pi} \beta^{-2} \left[\xi K_0 K_1 - \frac{v^2 \xi^2}{2c^2} (K_1^2 - K_0^2) \right] \tag{2.10}$$

$$n_{E2} = Z_p^2 \alpha \frac{2}{\pi} \beta^{-4} \left[2 \left(2 - \beta^2\right)^2 K_0 K_1 + \frac{\xi^2}{2} \beta^4 (K_0^2 - K_1^2) \right] \tag{2.11}$$

$$n_{M1} = Z_p^2 \alpha \frac{2}{\pi} \left[\xi K_0 K_1 - \frac{1}{2} \xi^2 (K_1^2 - K_0^2) \right] \tag{2.12}$$

Where K_n are the modified Bessel function of the nth order.

Adiabaticity parameter Expression 2.9 introduces the parameter ξ, which was then defined as the adiabaticity parameter and contains the information on the distance of closest approach for which the interaction happens only via the electromagnetic force. Closer than that, the cross section for the nuclear reaction mediated by the strong force becomes dominant and, thus, it is of little use to explore that region within this picture.
By defining the minimum impact parameter of the collision as R, the expression for ξ becomes:

$$\xi = \frac{\omega R}{\gamma v} \tag{2.13}$$

An interpretation of introducing this cutoff parameter is given in [Ber85]:

> "It amounts to punching a cylindrical hole in the plane wave and resembles the semi classical approach where R is identified as the minimum impact parameter that still leads to Coulomb interaction."

The minimum impact parameter R depends on the mass numbers of the projectile and the target nucleus and can be parametrised as follows [Ben89]:

$$R = 1.34 \left(A_p^{\frac{1}{3}} + A_t^{\frac{1}{3}} - 0.75 \left(A_p^{-\frac{1}{3}} + A_t^{-\frac{1}{3}} \right) \right) \tag{2.14}$$

Where A_t and A_p are the mass numbers of the projectile and the target, respectively; also, note that the expression is symmetric with respect to the target and projectile roles. Which is reassuring, because it allows us to study a nucleus in reverse kinematics, without the need of actually producing a ^{132}Sn target and thus make inhabitable a large part of Hesse.
Once the cutoff parameter R is fixed, so is the maximum possible excitation energy achievable by Coulomb excitation: $E_{max} = \frac{\hbar \gamma v}{R}$. In the case of ^{132}Sn impinging on ^{208}Pb at the beam energies utilized in the S412 experiment, this energy is calculated to be around 21 MeV[1], which is way above what we are interested in this work, but allowed for the study of the Giant Dipole Resonance (GDR) with the technique of Coulomb excitation.

---

[1] This energy refers to the maximum energy a single virtual photon exchanged by two nuclei can have, not the total energy that can be exchanged by the nuclei while interacting.

2.7.5 Coulomb excitation cross section from n-pole strength

From equation 2.7 it is possible to derive the differential Coulomb excitation cross section with respect to the energy. First of all, note that ω is the energy when multiplied by the reduced Plank constant; after that, the Coulomb excitation cross section is given by:

$$\sigma(E) = \sum_f \{n_{El}(E)\sigma_l^E(E) + n_{Ml}(E)\sigma_l^M(E)\} \tag{2.15}$$

To simplify things, though, most multipolarities can be neglected because the photonuclear cross sections for those processes are very small and they will not significantly contribute to the final spectrum. In practice, for this experiment it will be sufficient to consider:

$$\sigma(E) = n_{E1}\sigma_\gamma^{E1} + n_{E2}\sigma_\gamma^{E2} \tag{2.16}$$

Thus only for electric dipole and quadrupole.

Neglecting higher multipolarities The expressions 2.8 and 2.9 are valid for all multipolarities orders by virtue of their formulation –the authors of the paper maintain they hold as long as the original assumption that the first order perturbative approximation holds, but that is a limit we did not explore in the experiment S412.
The photonuclear cross section, though, which can be measured for some nuclei and can be also calculated independently, decreases sharply when the multipolarity order increase and, furthermore, the cross section for magnetic processes are usually a good order of magnitude smaller than those for electric processes.

The Thomas-Reiche-Kuhn sum rule A sum rule describes the transition of a quantum system from one initial state to some final states (hence the sum part of the name). In the case of transitions of a charged "oscillator" exposed to a varying electromagnetic field, the canonical sum rule to be used is the one published in 1925 by Thomas [Tho25], Reiche [Rei25] and Kuhn [Kuh25] at the same time, independently. This sum rule is often indicated as *the TRK sum rule.*
One application in nuclear physics of the TRK sum rule is to check the correctness of a proposed model for the collective excitations of a given nucleus. For the E1 and E2 transitions, the sum rule has the the parametrizations [Har01, War69]:

$$\sum\nolimits_{E1} = \int_0^\infty \sigma_\gamma(E)dE \approx 60\frac{NZ}{A}\text{MeV mb} \tag{2.17}$$

$$\sum\nolimits_{E2} = \int_0^\infty \frac{\sigma_\gamma(E)}{E^2}dE \approx 2.2\cdot 10^{-4}XZA^{\frac{1}{3}}\frac{\text{mb}}{\text{MeV}} \tag{2.18}$$

Where N and Z denote, respectively, the neutron and the proton (charge) number of the nucleus and X has to be substituted, for the quadrupole transitions, with Z for the isoscalar component and N for the isovector one.

These parametrizations can be then used to calculate the total photoabsorption cross section[1] for the selected multipolarity and, also, it has been observed that using them in conjunction with a Lorentzian curve will provide a good fit of the corresponding giant resonances. This latter approach, though, it is not suited to the energies examined in this work: in this region, in fact, the nucleus will have distinct energy levels and will not respond with a continuous spectrum; these, though, can be influenced in their density and relative strength by the so-called tail of the giant resonances that may extend also to energies well below the neutron separation threshold.

---

[1] It is customary to express the integrated cross section for a giant resonance in percentage of the TRK sum rule. This percentage is often very close to 100% [Ber70].

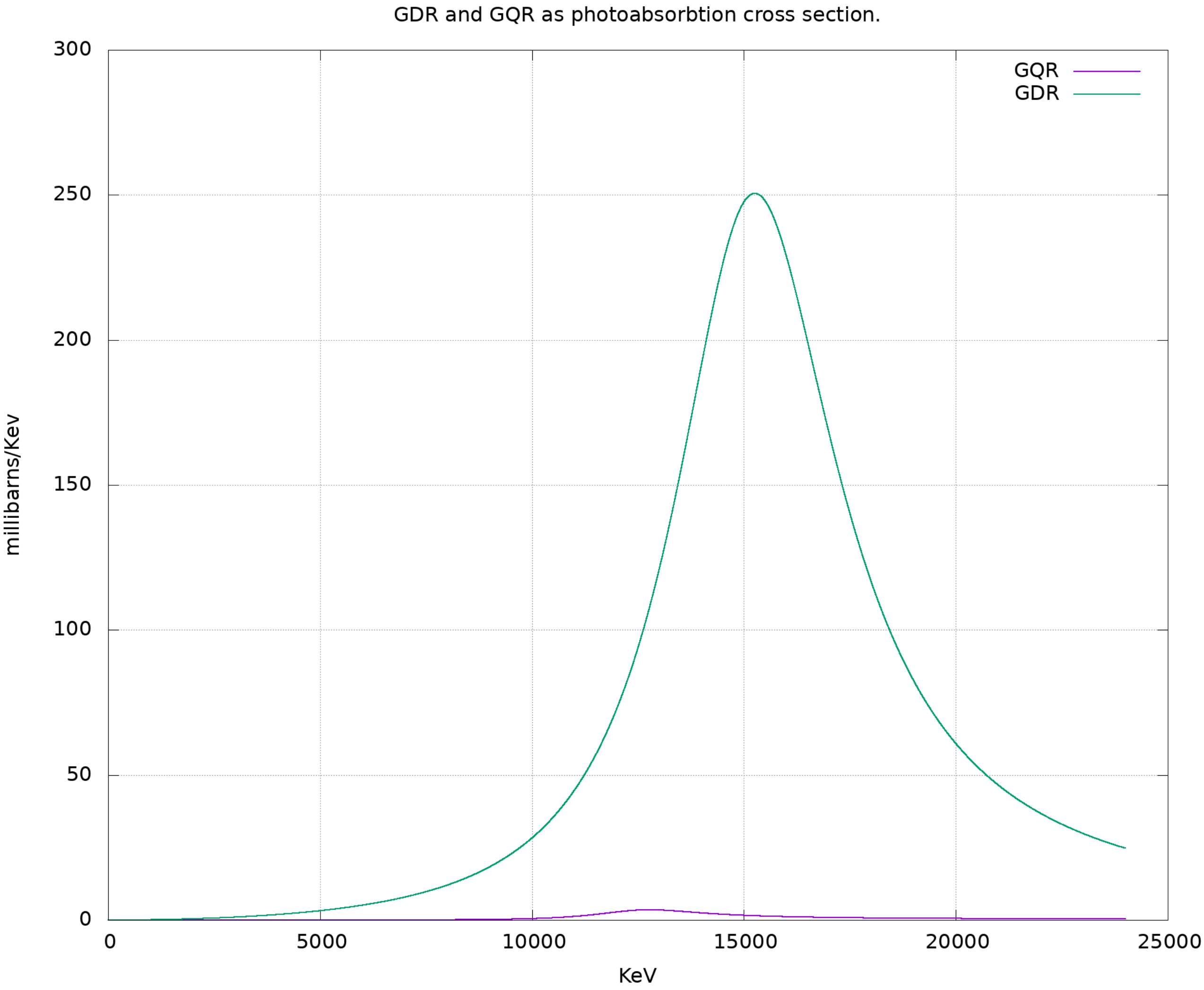

Figure 2.26: This plot shows the GDR and GQR as differential photoabsorption cross section, calculated according to the TRK sum rule and the virtual photon number. This picture is not realistic at low energies: below the neutron separation threshold, the nucleus is expected to show a level structure and not a continuum –although the functions used to generate the plot are defined also in that region.

2.7.6 α_D from dipole strength and photo absorption cross section distributions

The electric dipole polarizability, usually denoted by α_D, is a measure of the response of a nucleus to an external electric field -for its dipole component[1].

As anticipated in the introduction to this thesis, there are two kinds of dipole polarizabilities that can be discussed, a static one [BoNg81] and the dynamic one [Lip88]: whereas the first

---

[1] Given an electric field, you can expand it in terms of its multipole orders, each corresponding to the electric field generated by a distribution of N charges for the Nth order, at some given distances from each other.

relates to an electric field that does not vary with time (at the scale the process used to study it happens), the second one shows up when the nucleus is exposed to a varying electric field –hence: dynamic. Throughout this work, again, whenever not specified the subject is the *static* dipole polarizability.

Strength function The dipole polarizability is closely related to the dipole strength function. A strength function is an object of this sort [Lip88]:

$$S(\omega) = \sum_{k>0} \left|\langle k\,|F|\,0\rangle\right|^2 \delta(\omega - \omega_k) \tag{2.19}$$

Where F is the excitation operator and $|k\rangle$ are eigenstates of the nucleus[1]. The Dirac's delta in the expression will handily simplify the calculation of the moments for that function and, then, use those to define the polarizability with respect to that operator.
In the case of the dipole polarizability, the opreator in question is the electric dipole operator $\hat{D}$, which also happens to be an observable and thus well behaved. In general, then, the expression for the dipole polarizbility takes the form [Rei10]:

$$\alpha_D = 2 \sum_{k \in RPA} \frac{\left|\langle k \left| \hat{D} \right| 0\rangle\right|^2}{E_k} \tag{2.20}$$

Where the eigenstates k in this case are explicitly indicated to come from the random phase approximation, RPA.
A form that is more user friendly for the purposes of this work, and also relates to its motivation, is the familiar integral inversely weighted by the excitation energy [HaKr15]:

$$\alpha_D = \frac{\hbar c}{2\pi^2} \int_0^\infty \frac{\sigma_\gamma}{E^2} dE \tag{2.21}$$

$$\alpha_D = \frac{8\pi}{9} \int_0^\infty \frac{B(E1)}{E} dE \tag{2.22}$$

It is possible to express the dipole polarizability both in function of the strength function for the dipole response $B(E1)$ and in terms of the photoabsorption cross section σ_γ because of the relationship that links the two [Lip88].
In a Coulomb excitation experiment, as discussed in the previous sections, neither of the quantities are accessible directly, but one has to measure the Coulomb excitation cross section and then extract the information from there throught the virtual photon exchange number. Hence, to perform the integral, the photoabsorption cross section or (and) the dipole strength distribution have to be deconvoluted with a variant of the method proposed by Dr. D. Rossi in [Ros10]. This method will be described in the next chapter, when the result of it will be presented.

---

[1] The source uses natural unit, $\hbar = c = 1$.

Chapter 3

Results

Given the analysis methods and intermediate results presented in Chapter 3, it is time to apply them and say something quantitative about the main goal of this thesis.

3.1 A landmark: ^{132}Sn 2^+ state

^{132}Sn is a double magic nucleus: this means that it achieves a shell closure both for neutrons (82) and for protons (50). This condition is particularly energy favourable for the nucleus and so it is expected that the first excited state lies relatively high in energy above the ground state 0^+.

In this case, the first excited state for tin 132 is the 2^+ state at 4041.20(15) keV [RaBa05] and, most importantly, its electric quadrupole strength has been measured to be 0.11 ± 0.03 b^{2}e^2,[1]. This means that, after the event set has been selected, it is possible to calculate the expected Coulomb excitation cross section for the state. Under experimental condition, this is 2.6 mb, with a relative uncertainty of 27%; with this cross section, 42 ± 11 events in total are expected; taking into account the efficiencies involved in the reaction channel selection, this number is reduced to 26 ± 7 events.

What is included in this calculation The cross section quoted above is calculated assuming an excitation energy exactly[2] equal to the state to be populated: 4.04 MeV[3]; in reality, a range of excitation energies are accessible to this experiment and some of the states lying above the first excited one will decay into it instead of directly to the ground state. Since the objective of this work is not to provide a better measurement of B(E2) for the two-plus state, a lower bound to the cross section will suffice for the moment.

One way to have a potentially more precise comparison would be to select on events that *only* contain one photon at 4.04 MeV, plus or minus the resolution achieved by the Crystal Ball at

---

[1] The units in which the electric multipole strength function is given vary considerably across the literature; In general, a quadrupole strength should be quoted as having the dimension of a length to the fourth power at the very least, with the charge of the electron squared here to make it dimensionally "compatible" with the formulas presented in the previous chapter. Other units may be found in other works.

[2] In the close neighbourhood.

[3] Approximating the value for this state is not the end of the world, since the uncertainty in the calculations is anyway going to be completely dominated by that of the strength for the 2^+ state.

that energy, but this is around 25%, making the condition not particularly stringent. Furthermore, due to the thick target, the atomic background is very dominant and the probability of finding enough events for a meaningful comparison is as good as non existent.

3.1.1 Efficiencies involved

The efficiencies (and specificities, although they have a much smaller impact) considered to determine the *number of events* to be expected are those of the cuts employed to select the reaction channel, whereas the efficiency introduced by considering only half of the Crystal Ball does not play any role. Also, it is taken into account implicitly by considering only the front of the detector while analysing the simulations.

Furthermore, for a direct comparison, it is possible to choose whether to scale the spectrum resulting from the experiment *up* to neutralize the effects of the efficiencies involved and, then, simulate the number of events expected by considering the full sample, or scale *down* the expected number of events yielding a 4.04 MeV photon to match the number of events selected for the relevant reaction channel. This latter is the chosen approach and, so, the number of simulated events is 26 ± 7 events.

3.1.2 Comparison with the data

As stated above, only around 26 events are expected to have the 2^+ state excited and out of the around 285 thousands that constitute the dataset for the analysis. Such a figure though is not yet final: although it is correct from a reaction probability point of view, the efficiency of the gamma detection system must still be taken into account. This efficiency is in general complicated to calculate from principles, because the geometry of the shielding and all the other hardware around the target and the efficiency of the Crystal Ball itself, which is only considered in its *front* half, are not trivial. To take into account all these aspects, a Monte Carlo simulation has been chosen as the instrument for having, hopefully[1], a realistic expected spectrum for such a few events.

First of all, a simulation with just the said events has been performed, to investigate how the setup would respond in the absolutely best scenario of no background and no electronic noise. Note in figure 3.1 that the statistics is so low that it was not possible to populate all the bins in the region where the 2^+ state is found. Nonetheless, a clustering of events in that region is still clearly visible. This behaviour is not at all surprising, given the low statistics. Then, the atomic background (determined as explained in the previous chapter) was added to the data sample ex-post: this approach, as discussed previously, is slightly optimistic, but because of how the "canonical" atomic background is defined in this work, a lot more practical.

---

[1] A software is not the real world, but a model of it and it is as good as the coder. One hopes that a packages such as GEANT3.21 has been as thoroughly tested as humanly possible.

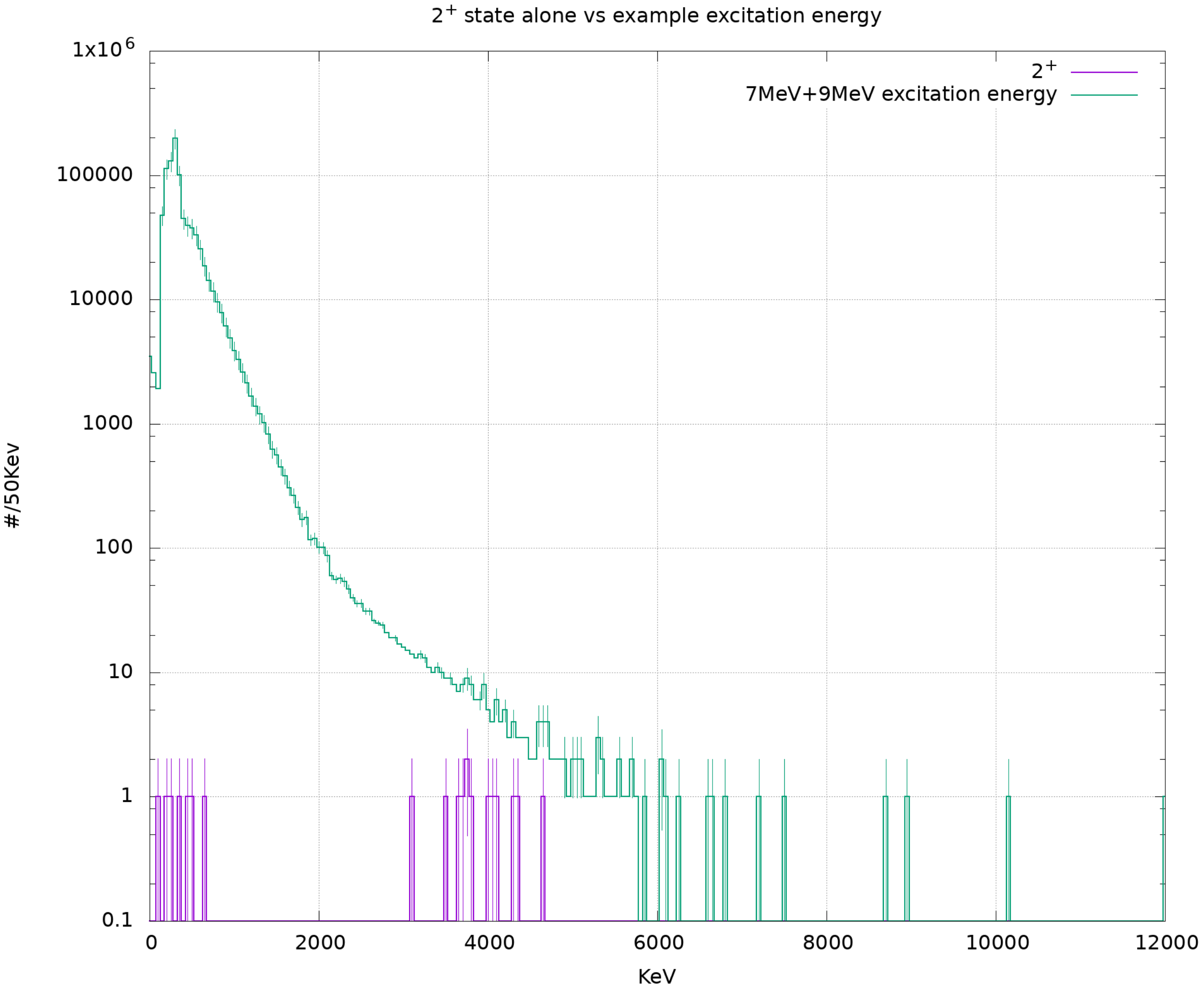

Figure 3.1: A comparison of two sample gamma cascades (calculated at 7 and 9 MeV excitation energy) and just the photons coming from the 2^+ state of ^{132}Sn. Both signals are scaled to comprise the same number of events (26) for a direct comparison with the selected events from the data runs. The gamma cascades are also simulated together the atomic background, whereas the empty target background has been summed afterwards.

Finally, the spectrum from the sum of the signal from the 2^+ state and the canonical atomic background can be compared with the data.

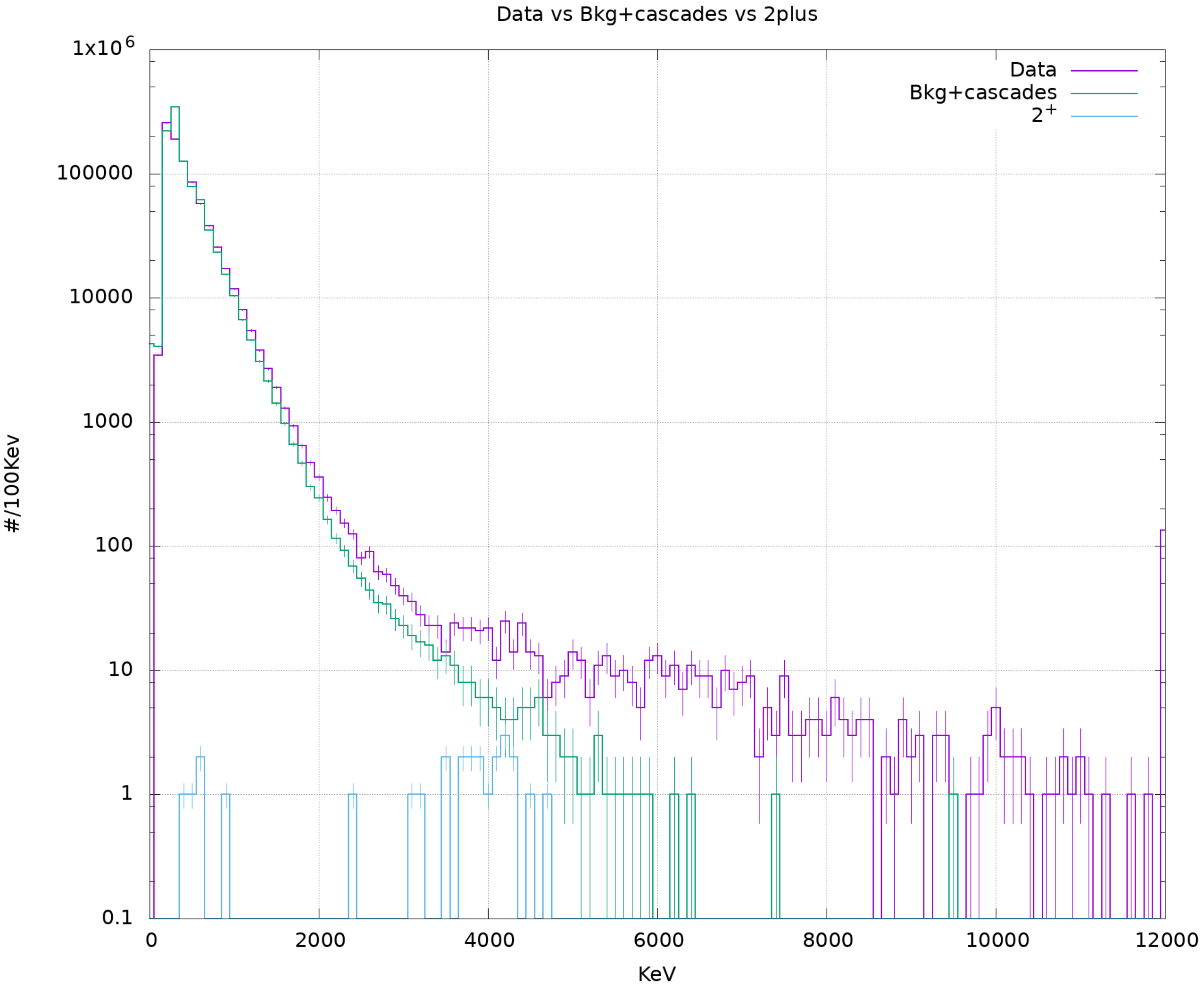

Figure 3.2: A comparison between two gamma cascades (generated at 7 and 9 MeV excitation energy), the data, and just the photons from the 2^+ state of ^{132}Sn.

As expected, the simulations slightly underestimate the observed data in the region of interest, around 4 MeV, but it is also apparent that there is a considerable overlap in the error bars: this is evidence of the 2^+ excitation of ^{132}Sn and also it is close enough to the theory to be considered acceptable.

It is also apparent that a lot more is present in the data. As it should be, since we are expecting also more gammas from the cascades that should happen at excitation energies higher than 4041 keV.

3.2 Target excitation

In the previous chapter, we noted an excess of hits in the Crystal Ball, mainly in the front. The fact that this event excess is located in the front suggests that its source is not at rest in the laboratory frame of reference; this can suggest that said source should not be target excitation, despite some calculations performed by A. Horvat would suggest 0.2 b of integrated cross section for photons due to the excitation of Lead nuclei. This can be justified [Hor19] by the linear dependence of the TRK sum rule in the nuclear charge, thus leading to an expected ratio of the Coulomb excitation cross section presented by the target and the projectile[1] of $\frac{\sigma_C^t}{\sigma_C^t} \approx \frac{Z_p}{Z_t}$. Although being very heavy, the Lead nuclei are bombarded by ^{132}Sn, which is in turn a significant fraction of the Lead's mass and charge, so the ratio above is expected to be not completely negligible.

A way to gather more evidence about whether it is due, at least in part, to target excitation uses the Doppler correction and the consideration that, because of the expected level scheme, for ^{132}Sn we do not expect events with a total energy deposition in the Crystal Ball of less than 4 MeV[2] (and no neutrons). The 2^+ state for ^{208}Pb lies at around 4.1 MeV [IAEAMar07], so it the method described in the following is expected to work for this isotope as well[3].

If we apply an energy cut on the sum energy for each event at the said 4 MeV to the *Doppler corrected data*, if the excess hits come from a source in motion there will be a clear separation between just background, with $\sum E < 4\,\mathrm{MeV}$, and events with physics in them, with $\sum E > 4\,\mathrm{MeV}$, whereas the same condition applied to a dataset that is *not* Doppler corrected would return no clear separation. And vice versa[4], if the source is at rest. It can be easily noticed, in figures 3.3 and 3.4, that there is no clear separation in the non Doppler corrected data, whereas the spectrum obtained from the Doppler corrected ones below 4 MeV of sum energy is fitted well by the atomic background simulation, also on the front of the Crystal Ball. This is a strong indication that the source of the excess counts is indeed moving and not at rest[5]. Given all this, it appears very unlikely that the excess counts in the front of the Crystal Ball can come from target excitation.

---

[1] Remember: projectile and target are completely exchangeable in the calculation for the Coulomb excitation cross section.

[2] The energy of the first excited state for ^{132}Sn is 4041 keV.

[3] Natural lead is composed primarily, around 52%, out of ^{208}Pb, followed in abundance by ^{206}Pb (24%) and ^{207}Pb (22%) and some others in traces. For these two latter isotopes, the first excited state lies at much lower energies, but they are expected to contribute less to the eventual signal, since they are less abundant. Note also that ^{208}Pb is a doubly-magic nucleus as well, hence the very high excitation energies.

[4] This particular cut would work also for lead, since the first excited state this nucleus lies at around 6 MeV

[5] But can't the Lead nuclei recoil? Yes, they would. But with a much lower kinetic energy than the beam, thus a Doppler correction based on the beam speed would clobber the signal. Remember that the excitation energies are in the order of a few MeV, whereas the beam carries in excess of 500 MeV *per nucleon* and the Lead nuclei comprise more than 200 nucleons.

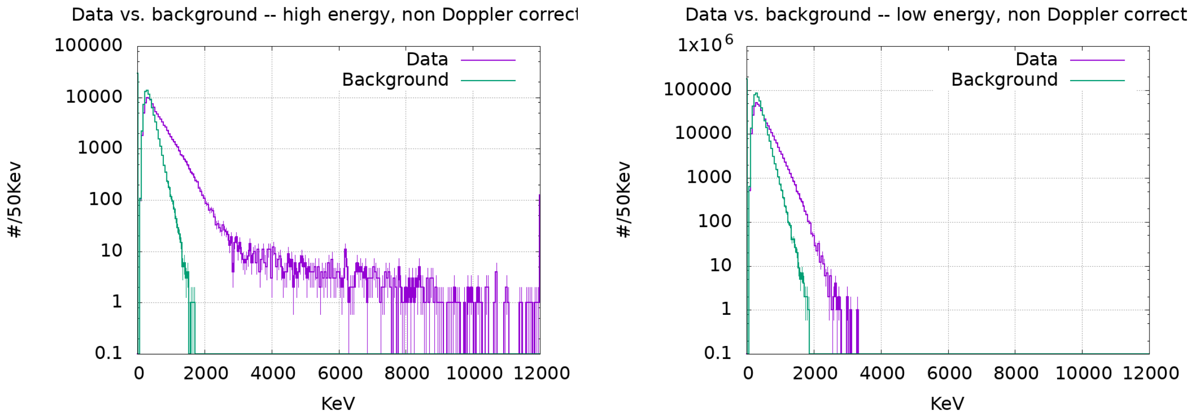

(a) This is the data sample for which the total energy is more than 4 MeV.

(b) This is the data sample for which the total energy is less than 4 MeV.

Figure 3.3: This is the comparison between the data sample and the atomic background (mostly non Doppler shifted) before the Doppler correction of both. If there were some target excitation, there would be discernible structure in the higher energy part (a) and a stark difference in the shape of the spectrum. As it can be easily seen: the only variation is in the bins at energy above the cut, which have some count in (a) and not in (b).

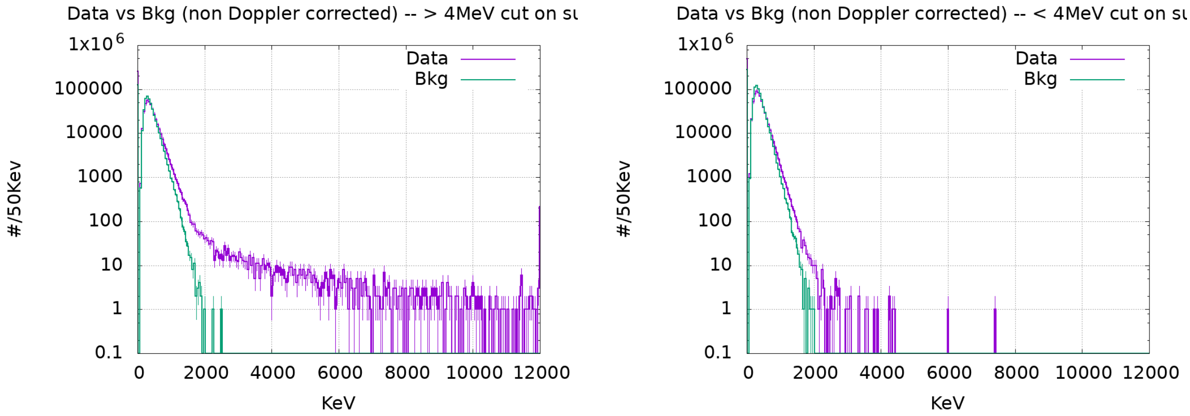

(a) This is the Doppler corrected data sample for which the total energy is more than 4 MeV.

(b) This is the Doppler corrected data sample for which the total energy is less than 4 MeV.

Figure 3.4: This is the comparison between the data sample and the atomic background *after* the Doppler correction: as can be seen, while in (b) the cut sample and the atomic background are essentially the same, in (a) the spectrum deviates considerably; this is a strong indication that the source of the signal above the background is in motion with respect to the laboratory, at a speed which is compatible with that of the ions.

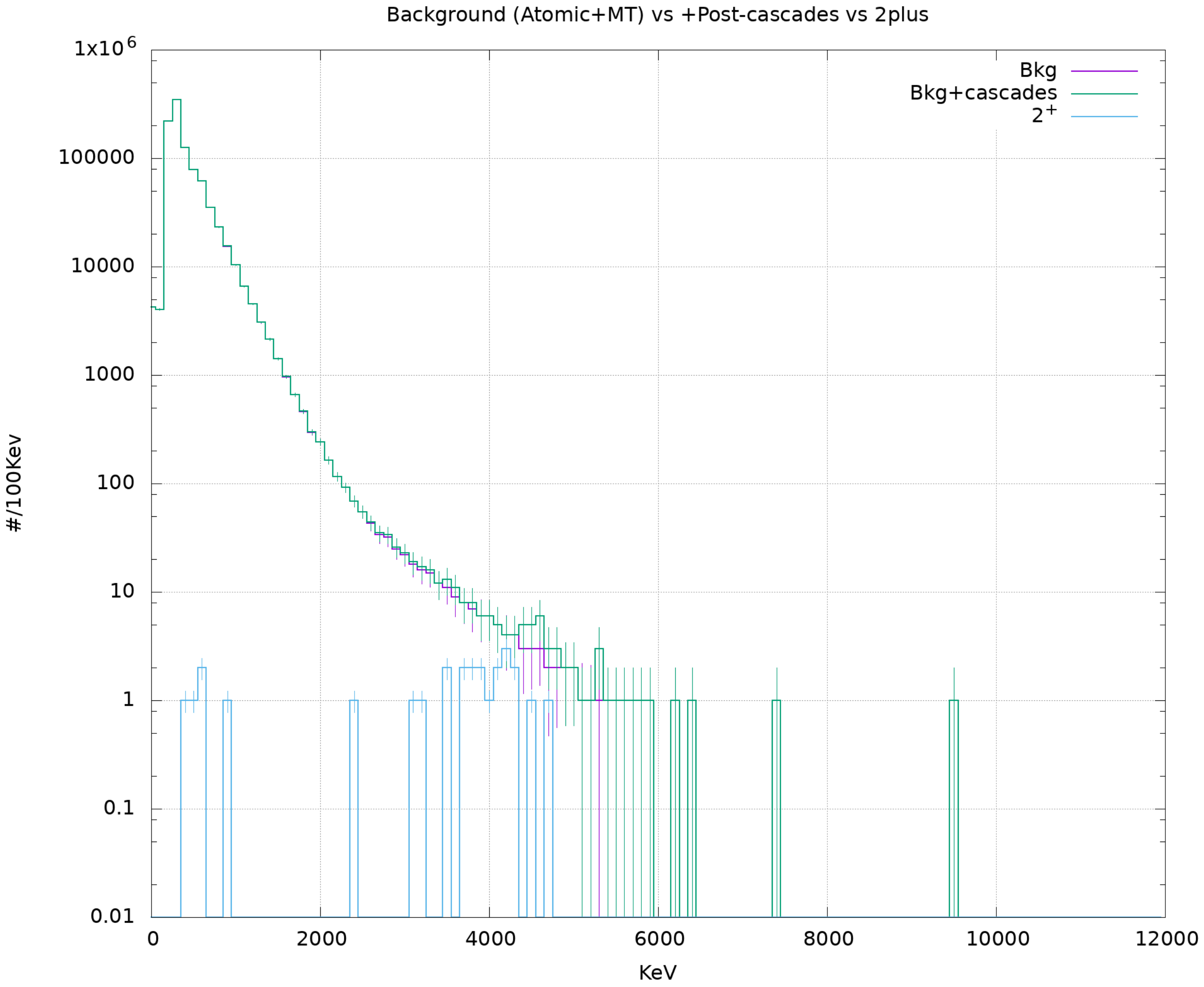

Figure 3.5: The comparison between the the atomic background plus the empty target background and (almost) the same, combined with two examples of a generated gamma cascade of ^{132}Sn, respectively for an excitation energy of 7 MeV and 9 MeV. The two gamma cascades are scaled to that the sum of their cross section for the 2^+ state is the one predicted by the strength measured by [RaBa05]. It can be noticed that the signal generated by the gamma cascades, especially in the region of the 2^+ state, deviates just enough from the reference background model to be above the sensitivity of the apparatus.

3.2.1 Sensitivity (short)

An important question to ask is whether the very small amount of event expected to come from Tin excitation would lie within the sensitivity of the Crystal Ball in the region of interest. More formally, if the excess counts due to the (faint) signal in that region, when considered together with the amount of background present, would be statistically significant.
To answer this question, I compared the canonical atomic background spectrum summed with the empty target contribution model and the same thing, only with the 26 ± 7 2^+ events added *before* the Monte Carlo engine[1].
A more detailed discussion of the sensitivity can be found in the next chapter.
In figure 3.5, one can see that in the region of 4 MeV the spectrum that comprises the signal does clear the error bars associated with the background, which is normalized for the number of events selected in the reaction channel, but the error bars associated with the spectra are still overlapping.
This suggests that expecting only 26 events out of 285 thousands is just about within the sensitivity of the Crystal Ball and the very large errors associated with the strength of the 2^+ state assumes a crucial role.

3.3 "Deconvolution" of ^{132}Sn cascades

An important problem to solve in this, like in every other, experiment is the necessity to separate the response of the detector system from the signal itself. In fact, every detector ever created has introduced some sort of distortion in the measurement it was supposed to do: this is due to the general impossibility of observing a particle "directly" while it rests on your desk, but always through the interaction with some matter and then scaling up that interaction so that some macroscopic system (such as a human being) can then look at it and interpret it.
For simpler detector systems, it is usually possible (if not particularly practical) to calculate a priori what the response is and, thus, correct the data collected from the detector itself to obtain the clearest possible picture. This might be the case, for example, for a single scintillator detector with a particularly simple geometry. In general, though, this operation is very difficult and may involve some drastic simplifications that might lead to the correction under performing.
One method to get around this difficulty is known as *deconvolution*[2] and was first refined by Dr. D. Rossi in [Ros10]. As used in this work, the deconvolution method is based on simulating generated events and then comparing combinations of those simulations with the data acquired

---

[1] As discussed previously, this takes also into account the performance of the clustering algorithm, which is an integral part of the detector system.

[2] Or "convolution", for reasons that will be apparent in the following. According to the inventor, this is a philosophical question.

during the experiment runs. These comparison are evaluated with the cost function:

$$\frac{\sum_{i=1}^{N} |\log(d_i) - \log(m_i(a_k))|}{N} \tag{3.1}$$

Where d_i represents the data points, $m_i(a_k)$ is a weighted sum of the spectra resulting from the cascades; the weights a_k are the subject of the fit. N is the number of data points: 241 for the full spectrum, 201 excluding the bins up to 2 MeV, excluded.

The best solution will be the one with the minimum value of the cost function. In order to decrease the sensitivity of the cost function to the background, a logarithmic weighting with respect to the absolute number of counts in the bin has been introduced[1].
For the comparison itself, twelve excitation energies between 4.04 MeV and 8 MeV[2] have been selected and, for those ten energies, a γ-cascade has been calculated with the software `Rainier`[3] [Kir18]: there comprise a nuclear level scheme with their relative strengths and transition probabilities, thus resulting in a collection of spectral lines. These levels is generated using a model level density scheme (for example, a back-shifted Fermi gas), but it's random by nature: the levels and the transition probabilities between them are randomly generated in the scope of the general model.
The datasets obtained are then mixed with the atomic background events and passed to `sbkg`, the Monte Carlo software based on GEANT3.21 and R3BRoot[4] in order to obtain a gamma spectrum as if the Crystal Ball was observing it from behind the target shielding and structure.
The spectra resulting from the simulation are then summed with twelve different, variable coefficients a_k and fitted[5] to the data spectrum.

---

[1] This, essentially, amounts to comparing the two spectra in a logarithmic scale, if you were to run the comparison with your own eyes.

[2] Although the energy of the first neutron separation for ^{132}Sn is 7.35 MeV, I opted to add two energies above that to both probe whether there is some amount of the Coulomb excitation cross section for the gamma decay above S$_n$ and, since this is not expected to be significant, as a "canary in the gold mine": if all the strength seems to come from where it's not supposed to, then the adoption of that fit may be considered questionable.

[3] Opportunely tuned and modified by Dr. D. Symochko.

[4] Please see appendix D for more information.

[5] Because of the high number of free parameters and the dominance of the atomic background, I developed a tool that allows for manual resetting of some or all the coefficients and then explore the immediate neighbourhood of that point in the 12 dimensional space around the coefficient vector. For more details on the tool, please consult appendix A.

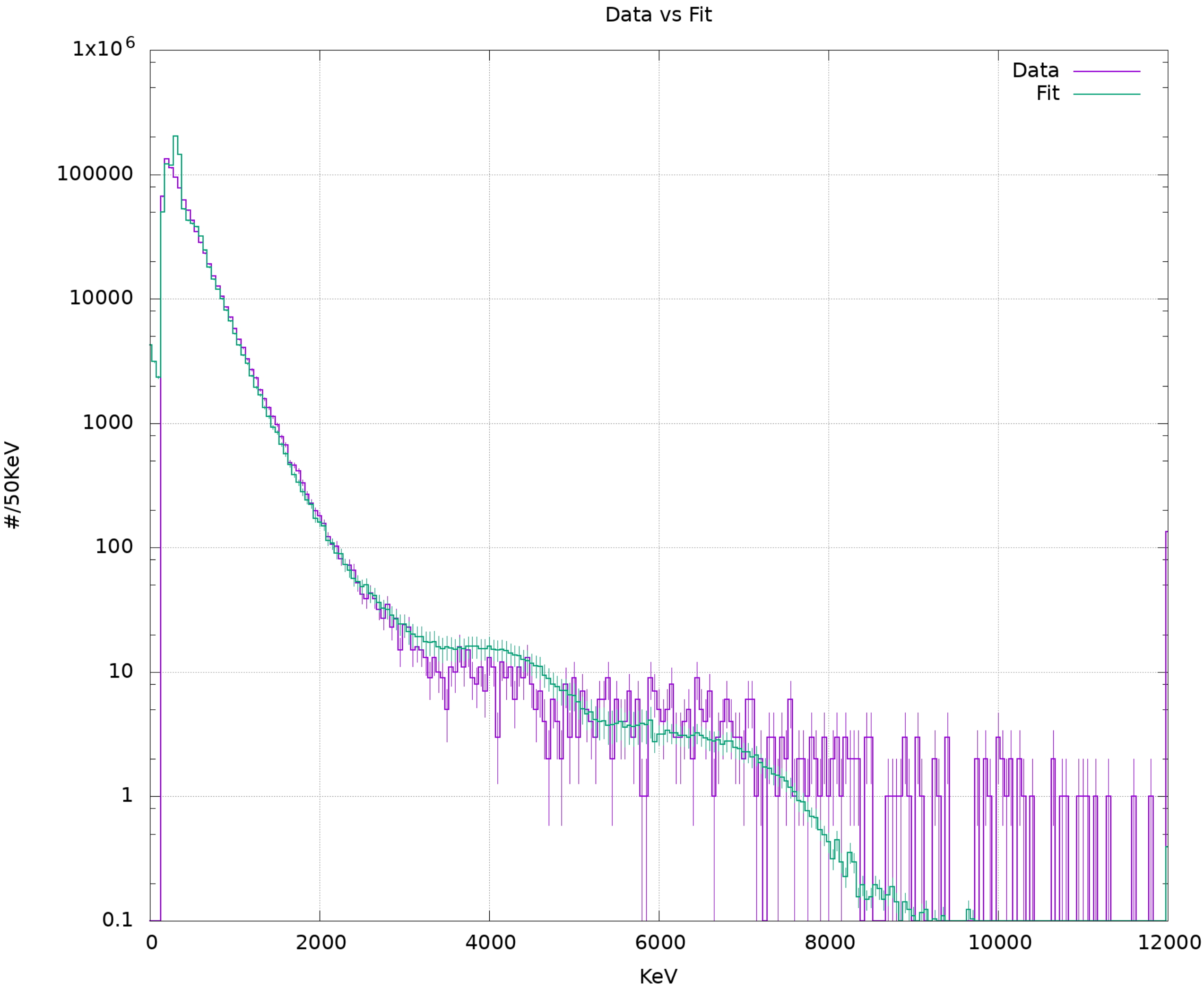

Figure 3.7: This plot shows one realisation fitted to the data.

3.3.1 Nuclear realisations

There are several hypothesis on how the level structure of ^{132}Sn may look like between the very well known first excited state at 4.04 MeV and the neutron separation threshold. The approach that was chosen for this analysis, though, is to start for how much as possible with a blank sheet of paper, and randomly generate the level scheme. This would allow, in future, to compare with various hypotheses and allows now to keep the analysis as much as independent from a single model as possible.

As mentioned before, these realisations are generated by a software called `Rainier`: the nuclear realisation also includes transition probabilities.

To perform the fit, twenty-five different realisations have been produced and tested. Since there is in principle no favourite nuclear realisation a priory and, after the fit, it has been noticed that the goodness of the fit did not vary very much between the realisations, a value for α_D is

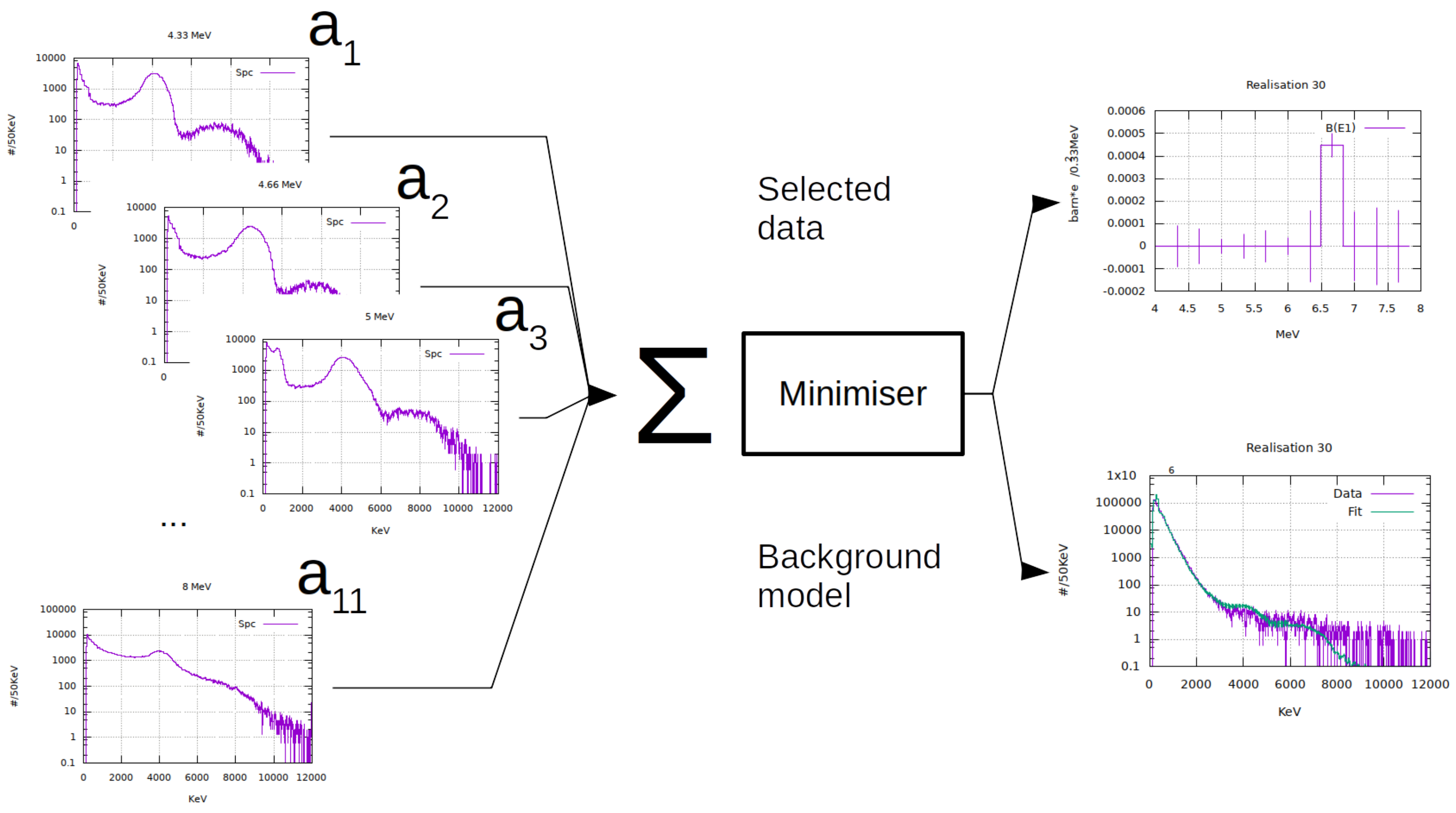

Figure 3.6: This schema illustrates, in a simplified way, how the deconvolution procedure used for this work operates. Some gamma cascades, already simulated together with the model background, are assigned a coefficient a_k and then summed, weighted by that coefficient. Note that a_0 is associated to the direct excitation of the 2^+ state and is not shown in the picture. Then, the model background is added *again*, but as a fixed quantity: this is necessary because not every ion interacts with the target and not every interaction leads to a purely γ decay.

This sum is then passed to the minimiser, which compares it with the data according to the cost function 3.1. At the end of the procedure, a fitted spectrum is produced by representing the sum described above, performed with the coefficients individuated by the minimiser, and also the coefficients for each γ-cascade is converted into a dipole strength, B(E1).

calculated for each realisation and then these values are averaged to obtain an estimate. The values of α_D calculated are organised in an histogram in figure 3.9.

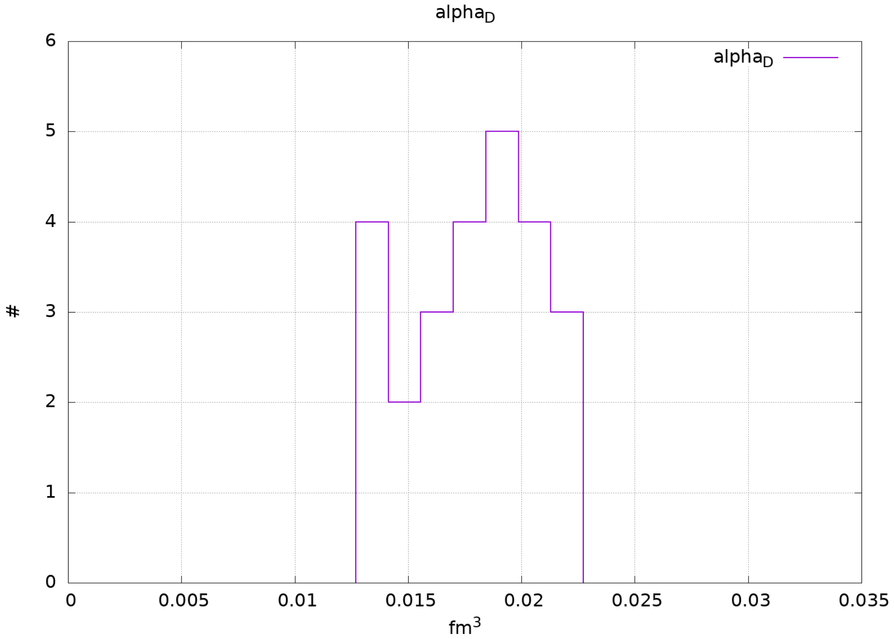

Figure 3.9: This is the distribution of α_D resulting from the "deconvolution" of the γ-cascades.

Because the dipole strength distribution and the photo absorption cross section distribution underlying the generated γ-cascades are known, it is now possible to performed the inversely energy weighted integral up to the neutron separation threshold.

3.4 Dipole polarizability

Once the coefficients for the ten excitation energies have been determined, it is then possible to compute the integral(s) in equation(s) 2.21.
That said, the dipole polarizability is estimated as $0.018 \pm 0.007_{\text{stat}} \pm 0.003_{\text{sys}}$ fm^3,[1] from the dipole strength distribution, calculated from around 4 MeV up to 8 MeV. This value has to be summed to the one obtained in previous works from the neutron separation threshold to the limit of the Coulomb excitation for the experimental conditions (about 21 MeV) to obtain the dipole polarizability on the whole spectrum.

---

[1] The statistical error derives from the error reported on the fit parameters, which in turn ultimately depends on how much statistics was possible to gather from the experiment. The systematic error takes into account the uncertainties on the event selection, the width of the α_D distribution shown in 3.9 and the possible contributions from nuclear reactions and the tail of the GQR, see section 3.4.1.

3.4.1 Is it really just the dipole strength?

The short answer is mostly. In fact, because of the method used to produce the nuclear realisations, one cannot be sure about the multipolarity order of each and every level generated. Despite that, some considerations can be made about how much dipole strength is there to be seen among the total strength itself.

GQR and TRK sum rule Another way to impose an upper limit on the contribution of the B(E2) strength to the total strength below threshold may be estimated considering the tail of the GQR. Famously [Nor90], the quadrupole response of the nucleus can be modelled with a Lorentzian curve:

$$\sigma_{\gamma,\mathrm{E2}} = f \cdot \frac{2}{\pi\Gamma}\frac{\Sigma_{\mathrm{E2}} \cdot E^2}{1+\left(\frac{E^2-E_m^2}{E\Gamma}\right)^2} \tag{3.2}$$

Where E is the energy, Γ is the amplitude of the Lorentzian, E_m is its central value and f and Σ_{E2} are the distribution of the sum rule strength and its value calculated for the quadrupole operator.

The profile of the GQR can be seen in figure 2.26, in arbitrary units. This is not a particularly good picture for below the neutron separation threshold, where the nuclear states are not expected to occupy a continuum but be well separated (with a possible increased density around the PDR region), but can be used to give a not unreasonable upper bound to the contribution of B(E2) to the total B. Reported in [Sch15], from [Har01], the parametrization of the GQR is as follows:

E_m	12.37 MeV.
Γ	3.1 MeV
Σ_{E2}	0.108 mb/MeV

This contribution is, integrated from 0 to 8 MeV, 5% of the total observed strength, well below the relative error that could be achieved on the value for the dipole polarizability.

Any other multipolarity? In general, the contribution of higher multipolarities decreases exponentially while their order increases, so it is expected to be negligible. The same, essentially, goes for the magnetic modes.

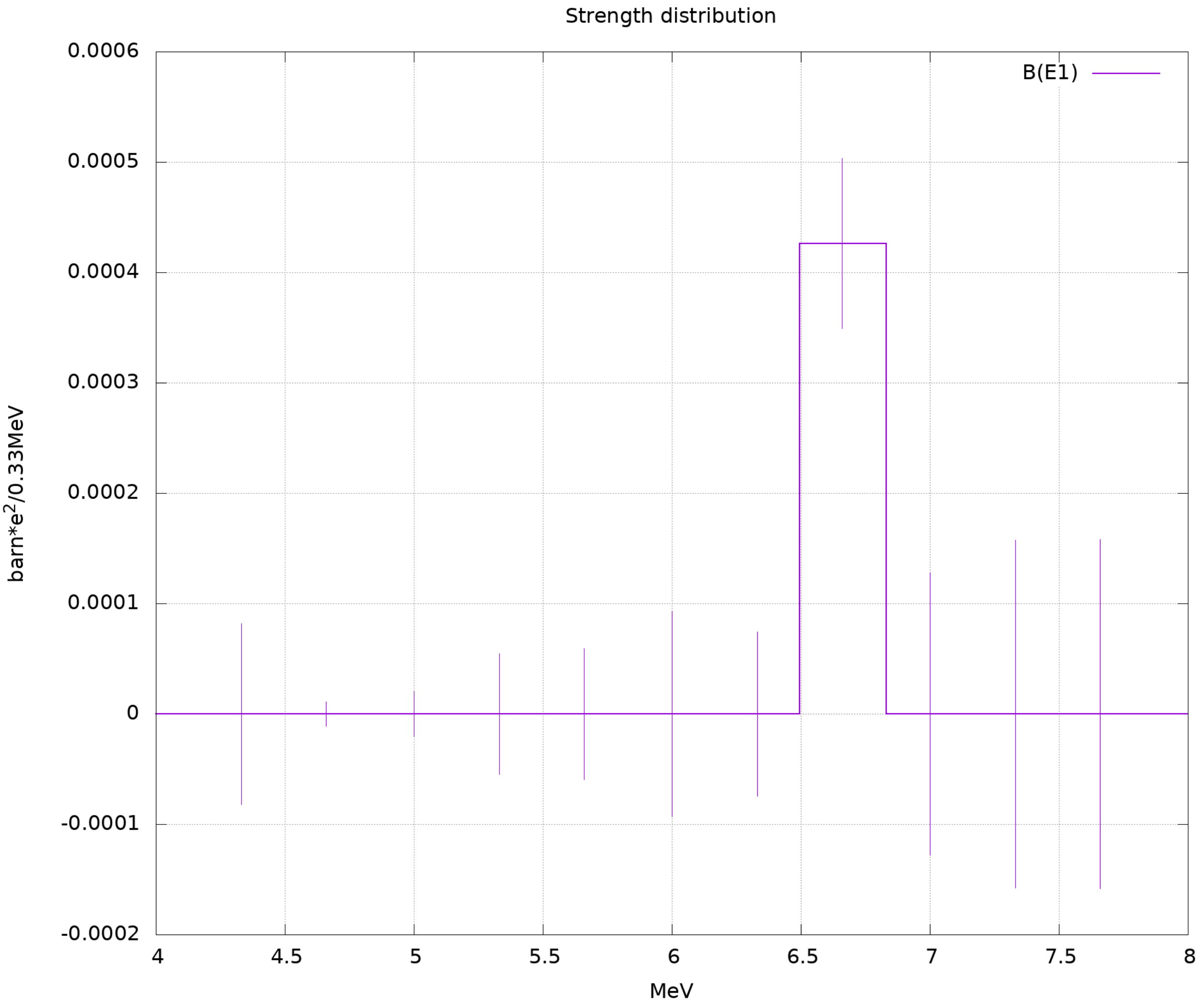

Figure 3.8: This figure shows the dipole strength B(E1) the minimiser thinks each of the 12 excitation energy should contribute to the final spectrum, in order to sit at a (constrained to positive value weight) minimum of the cost function. As it can be noted, there is only one, largish contribution from an excitation energy of 6.67 MeV. The errors reported by the fitter are significant, though, so other contributions seem to be not ruled out completely. The one that is individuated, anyway, sits significantly above 0.
This is of course shown as an example of the procedure's output.

Chapter 4

Conclusions and Outlook

The major aim of this work has been reached: an estimate for the dipole polarizability of Tin 132 is now available and can be thus used to constrain the L parameter of the nuclear equation of state.

4.1 Sensitivity and target choice

Although a thicker target is preferable because it offers a larger cross section for Coulomb excitation, a thinner one would give rise to far less atomic background –which is a bane for the sensitivity at low energies. So, which is best?

4.1.1 Sensitivity

The sensitivity of the detector system is its ability of delivering a signal above the uncertainty. In other words, one can consider the sensitivity of the detector system for each energy bin the minimum distance between counts in that bin, so that those number are separate.

A particularly stringent, yet well founded, way to decide whether two counts are separate is to square-sum[1] the uncertainties they have appended to and consider that value the minimum distance for which their separation counts as significant[2].
For the thick target, the one used in the experiment, the sensitivity estimated, as described above, is around 10 counts of separation in the 4 MeV region. For the thinner target, this estimate is at around twice that, for the same region and the same selection criteria. This result has an explanation and a caveat, though, which can be found below below.

---

[1] The cumulative error on a sum of two independent, stochastic variables is usually given as the square root of the sum of the squares of the respective uncertainties. The resulting quantity will correspond to half of the 68% confidence interval for the sum variable.

[2] They stay clear from each other's 68% confidence interval.

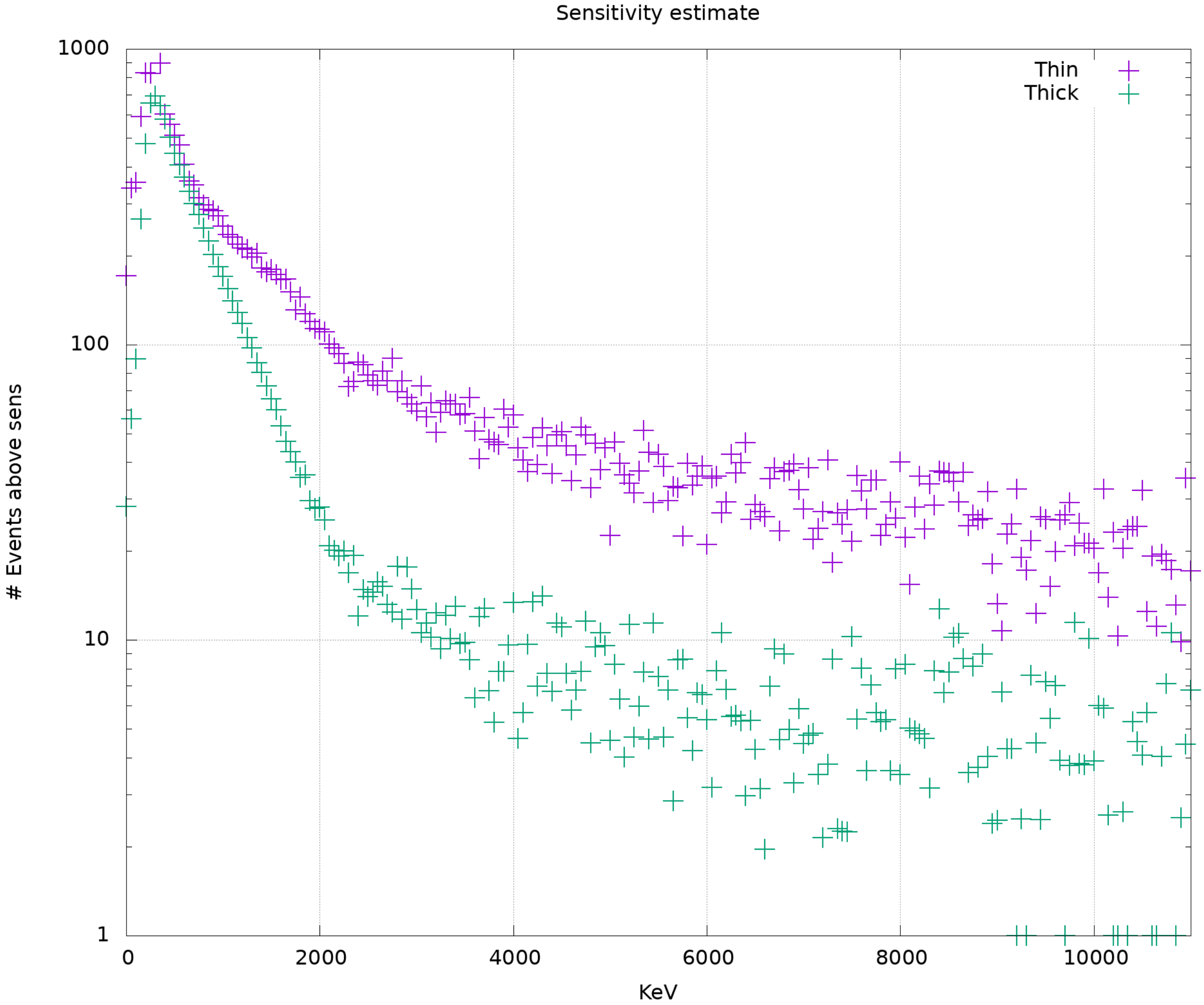

Figure 4.1: For each energy bin (for the gamma spectrum of the CB), an estimate of the sensitivity. These estimates have been deduced from the total amount of background, atomic and empty target contribution alike. This second, though, has been treated a bit differently than usual. In figure 2.19a a fit has been produced and used to model this kind of contribution. This is a good idea, in short, because the spectrum is "jagged", especially at higher energies, and simply multiplying it by a factor would lead to counts that are probably not a good estimate. The fit has the limit, though, of effectively estimating 0 counts from above 5 MeV. To have a non-0 estimate also above that energy, the empty target spectrum has been first smoother with a Savitzky-Golay filter of order 3 and length 21 and then scaled up to match the data.

4.1.2 Target choice

If the material used is the same, two key aspects differentiate the targets: the amount of atomic background produced and the amount of beam time required to collect a meaningful amount of events. Thicker targets present a larger cross section to the ions, thus they will generate meaningful physics quicker, at the expense of more atomic background *per event*, exactly because the increased cross section presented.

Thinner target will require longer observation times but, for every event, less photons from atomic processes will be generated. Aside from monetary costs, longer exposure times will also increase the chance of random coincidence and, thus, may introduce some additional noise in the data. As explained before, though, a possible mitigation would be to observe an empty target in the same experimental condition, which should also account for random coincidences and cosmic rays[1].

Whereas the thin target would, for the same number of events collected, be just as noisy as the thicker one in term of global counts of photons due to atomic processes, each event would contain fewer of them and, also, these would be generally lower in energy. This would mean that a "simple" cut on events, whose total energy does not add up to more than 4 MeV, would dramatically reduce the contribution of atomic background, whereas leaving the contribution from ^{132}Sn as good as untouched. This is, sadly, not true for the thick target, that contributes more than 4 MeV for a significant fraction of events.

This has to be balanced against, as mentioned, increased costs, running time and increased random coincidences.

---

[1] Assuming that no major solar flare or coronal mass ejection hit that day.

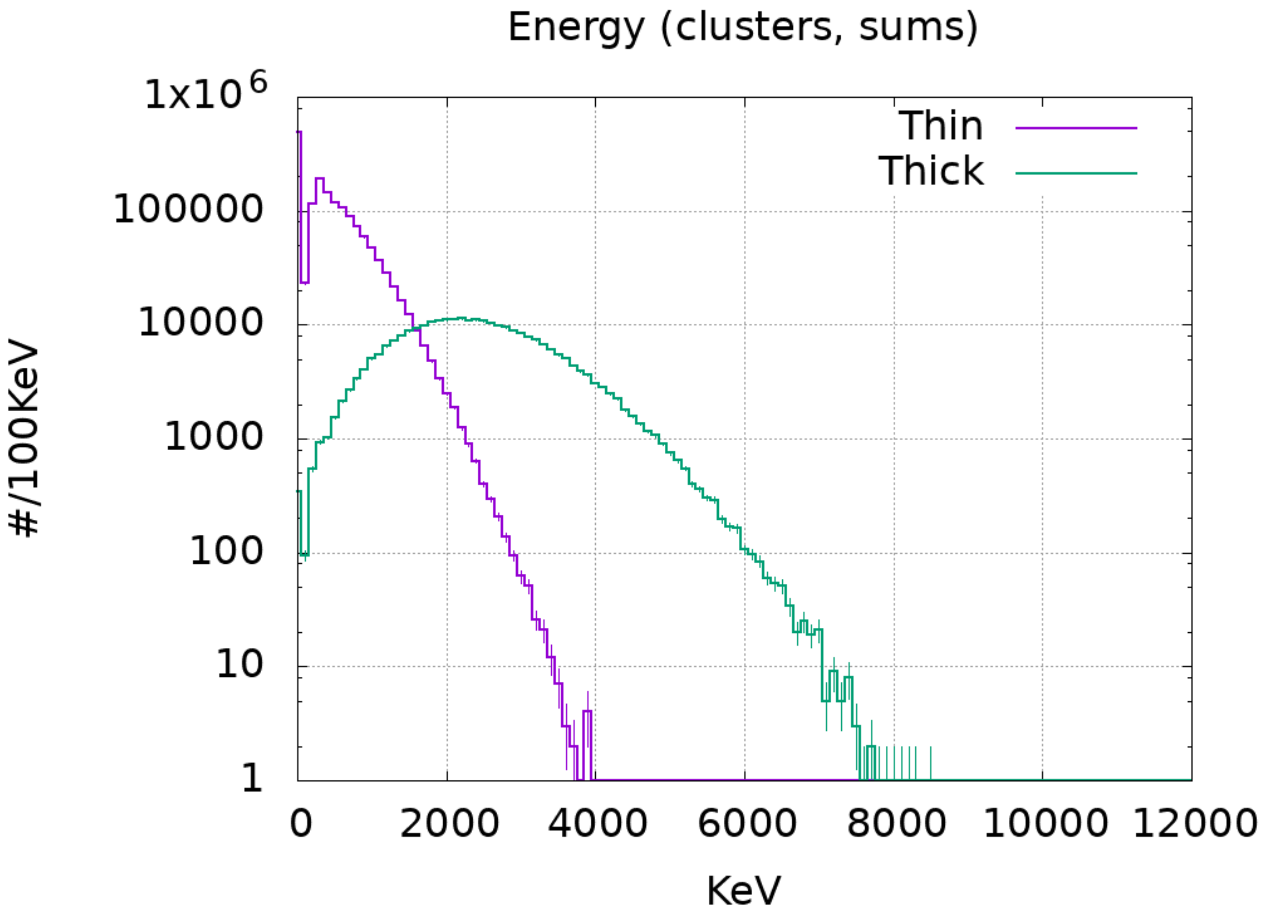

Figure 4.2: This is the spectrum for the sum energy generated by the background, for the thin and the thick target. As it can be very easily noted: the contribution from the atomic background of the thin target never exceeds 4 MeV, it is then possible to completely remove the events that contain *only* background and no subject physics from the sample by cutting on the sum energy. This is very evidently not true for the atomic contribution of the thick target, which is for a good fraction above the 4 MeV threshold. Thus, a thinner target would have the potential to increase the sensitivity below 2 MeV, should this be desired.

4.1.3 Outlook

All thing considered, if this experiment were to be repeated, the first recommendation would be to gather more statistics with the thick target, mainly by increasing the beam luminosity to lower however much possible the chance of random coincidences in the 4 MeV region. If sensitivity sub 2 MeV becomes of utmost importance, though, longer exposure times with a thinner target is recommended.

As far as energy resolution is concerned, it has been showed that the limiting factor is the detector's granularity; this has been already addressed with the new proposed gamma array CALIFA [Califa]. Following that, further development of the clustering algorithm may mitigate the peak broadening due to the numerosity of the atomic background photons; from past experiences, I may also suggest that a matched filter may be able to solve the problem of ”all the photons look alike” to the detector, but this is definitely a solution that necessitates further study.

What about the other Tin isotopes? The method developed here is portable to other Tin isotopes studied in this experiment; in some cases, the results may be more precise due to increased statistics and cross sections. Furthermore, a similar clustering algorithm can be easily developed for the CALIFA gamma array, currently being commissioned and that will be used in future R^{3}B experiments and, as stated above, the energy resolution would benefit greatly from the higher granularity of the new detector. This would also translate in smaller error on the fitted parameters.

Appendix A

Toolkit

The toolkit used to analyze the data from the Crystal Ball is composed of three subsets of programs, two of which have been developed by me.

A.1 Land02

To unpack the data of the experiment I used Land02. Although some cosmetic changes to the code had to be made periodically to allow compilation with modern versions of GCC, the semantic of Land02 was unchanged, thus any description found in many previous works is still completely accurate.

A.2 XB programs

Xb programs, or `xb_progs`, is a collection of programs that extract the data from a CERN's ROOT format to one easier to handle, run the cluster, the Doppler correction and a couple of other minor things. Each single action is performed by a single program: this is intended to give more flexibility in the analysis and having a limited amount of options for each program, without sacrificing too much performance.

A.2.1 Why not ROOT?

Most of the operations needed to treat the Crystal Ball data, such as Doppler correction and clustering, are not present in ROOT and have to be developed independently, making the use of the ROOT framework of no advantage in that respect. Furthermore, ROOT has a very painful habit of relying on global variables that are sneakily modified behind the programmer's back: this means that shared memory parallele execution is not compatible with ROOT. Since this paradigm is remarkably convenient when processing events, ROOT can also become a hindrance.

Aside from the parallel processing considerations, there are also minor things that would be more difficult to get working with ROOT instead of without it: after making a balance of the time needed to use ROOT, program efficiency and practicality, I opted to not use CERN's framework for the analysis.

A.2.2 Data structures

The data structures used to manipulate and store the data are:

xb_event_holder It's the parent type for all the structures used to store event information. It contains:

1. Event multiplicity
2. Event number
3. Trigger pattern[1]
4. Beam velocity relative to c.
5. Incoming charge (if it applies[2]).
6. Incoming mass-to-charge ratio (if it applies).

xb_data This structure holds the single hits in the Crystal Ball for a single event. Among[3] the information saved in this structure is:

1. Index of all the firing crystals.
2. Energy deposited in the crystals (in the same order as the indices are memorized).
3. Time stamp.

xb_track_info This structure contains the tracker[4]'s output, such as the beta in the middle of the target (calculated by the tracker) and the number and mass of the fragments. The velocity of the projectile in the middle of the target is of particular relevance for the Doppler correction.

xb_clusterZ This structure contains the *clusters inside the event* and the cluster multiplicity, aside of the event holder header.

xb_cluster This structure contains the information for every single cluster and *does not inherit from the event holder*. Among the data saved inside here there are:

1. The centroid, with its index and its angle.
2. The indices of all the member crystals.
3. The energy deposited in every member crystal.

---

[1] The "trigger pattern', or Tpat, is a byte-array that carries information on what detector generated a valid trigger in the current event. This field is used to aid the selection of the reaction channel.

[2] Sometimes this field is unused for simulations.

[3] Land02 has many fields dedicated to the Crystal Ball, although not every one of them always contain useful information; in any case, xb_data saves every field –or "leaves", in ROOT jargon.

[4] At the present moment, the Land02 tracker is "Ralph's tracker" [**?**].

4. The total energy of the cluster.

xb_arbitrary_data This is an extensible structure (it's a cousin of a generic associative array) that can be used to store data relative to other detectors if needed.

These structures are also replicated in the GNU Octave tools[1], which will be discussed in the following.

A.2.3 File format

The file format is straight forward: it consists of an header carrying minimal information and then the data structures above following, in a linearised form.

The data is also compressed before writing to disk using the `bzip2`; to keep the I/O real time needs at a minimum, a parallel implementation of said program is used whenever possible. When this is available, there is also a noticeable performance gain compared to ROOT formats.

Inch-worm or all in memory? Because also relatively small machines come with a very large amount of memory and the datasets I have been dealing with are not very large, I took a "short cut" and work completely out of memory; that is: the files need to be fully loaded (or copied, when piping data from a program to the next) in memory before any processing can happen.
This is not strictly necessary and limits the flexibility and portability of the toolkit, but it has never represented a problem big enough to need fixing[2].

A.2.4 Data conversion

The program `xb_data_translator` brings the data from a ROOT format to the internal format[3].

While switching formats, the program also performs some checks on the data: Land02 flags invalid or empty fields in its structures with `NaN`[4], whereas saturation of the detector is flagged with `Inf`; this may create problems when performing calculations. To avoid always checking before calculating everywhere (and possibly invalid results), events that are empty are flagged

---

[1] Which hasn't always been the most efficient approach, admittedly, but it makes the data appear consistent throughout the toolkit.

[2] Except on Octave, where most numerical entries are effectively saved as a double, increasing the memory consumption significantly when compared to the toolkit's programs.

[3] The internal format is straightforward enough; for the finest details, please refer to the documentation in the package, otherwise refer to section A.2.2

[4] Not a Number.

as such and optionally removed from the dataset, either by deleting them or by setting the affected value to something that would behave well in calculation while clearly meaning ”empty”[1] in that context.
The strictness of these checks can be modified at the command line, as needed[2], or completely turned off with the option `-R`.

This program extracts the tracking information from appropriately processed Land02 output as well. This selection is done at launch with a command line option `-t`.
Not all the information is memorized in the same file because of memory usage concerns. When information has to be combined, the events are matched using information such as the event ID (a progressive number) and some other features such as the Tpat[3].

A.3 Octave tools

Alongside the programs of the toolkit, also a number of Octave functions and scripts have been developed to allow for easier and more time-efficient manipulation of the data.
GNU Octave [Octave] is a free software[4] package for scientific computing originally developed by John W. Eaton and which shares the same language as the proprietary suite ”MATLAB”. The main interest in Octave for this work lies in Octave’s syntax, which is in general very compact and is remarkably smart in its handling of code vectorisation, and in Octave’s prompt itself, which is particularly suited for data manipulation at the command line. In this aspect, I find it superior to the standard Python prompt[5] and is significantly less cumbersome than ROOT’s CLING, using its pseudo-C++ syntax.
There may be a speed penalty at times (not always, especially if the code is properly vectorised) and this was experienced in one or two applications, due to the early decision of maintaining the same data format as the suite, but this was not really significant when compared with the speed up in the development process and, above all else, the interaction with the machine while handling the data.

---

[1] Mostly, this means setting the affected value to 0, although not always.

[2] When producing an arbitrary data structure, no *NaN* removal is performed since an appropriate substitution is not trivial. One could engineer a way to pass the proper parameter at the command line or with a config file, but there’s a limit to over-engineering.

[3] Although the event ID number should be more than sufficient, extending the comparison base will reduce the risks of false positives.

[4] It adheres to the principles of the Free Software Movement, it’s not just gratuitous or open source.

[5] Among the very numerous declination of Python there are some that come close to Octave, though. But Octave was a language I already had familiarity with.

A.3.1 ”Manual fitter”

To this work, the most important Octave script to have been developed is the so-called ”manual fitter”, which is slightly more than what its name suggests: it can also operate autonomously –and ideally it should, in ideal to good conditions.

This bit of software expects several files containing the components of the fit: these are the generated data for the 10 different excitation energies. Then it loads the experimental data and optionally a fixed background model.

After this, the cost function shown in 3.1 is prepared. Where N is the number of channels in the spectra, d_i is the value of the i-th bin, $\vec{a}$ is the parameter vector and the model which is being fitted is denoted as $M_i(\vec{a})$, and is a sum of the generated spectra weighed by the components of $\vec{a}$.

I settled for this kind of cost function, based on the logarithm of the counts, and not on a canonical version which would consider just the counts linearly, because in the region between 0 and 3 MeV the atomic background dominates the data by several orders of magnitude and, thus, a fit ”in linear scale”, so to say, would be as good as blind in the region where mostly the photons from the nucleus are present, which is the region where the fit *has* to work reliably in order to point to a realistic model for the energy weighted integral 2.21.

Manual fitting Where the manual intervention of the user is possible (at times, required) is between the various iteration of the minimiser –in this case, a simple gradient descent algorithm in place of the more sophisticated but less stable internal Octave functions. The user can set the learning rate of the algorithm[1] and reset each single component of the parameter vector $\vec{a}$. This approach is somewhat unorthodox (or, at least, rarely disclosed in literature) because it points to a fit that is not particularly robust. In the case of this work, given the preponderance of the atomic background and, in general, the numerosity of the fit parameters, it allows for at least faster execution if not a more reliable fit altogether.

A gradient descent minimiser is guaranteed[2] to converge at a local minimum, assuming the function has one, but not to the global minimum: already in this case, the possibility of setting the starting point of the algorithm may give an advantage. Furthermore, it is possible to steer the algorithm away from minima that can occur but are unphysical.

Another approach would have been an extensive search of the parameter space and then finding the minimum value for the giant 10-dimensional resulting tensor. This approach, though, is

---

[1] The gradient descent determines the gradient at a point in the function’s domain and moves a (small) negative multiple of the vector. It is customary to indicate this multiple as the ”learning rate” of the algorithm; this nomenclature is mutuated from the machine learning terminology, where these tools are frequently used.

[2] Given a proper setting of the learning rate: if this is too large, the minimizer can actually oscillate around the local minimum and even move away from it, indefinitely, until the iteration limit is reached.

very computationally demanding and can quickly become infeasible if the search space becomes too big: in this sense, it could be combined with a gradient descent that points to a candidate minimum (or a set thereof) and then the whole search space is finely sampled. Still, this would have been just too demanding on the hardware compared with a minimiser with the option of user intervention.

Appendix B

Clustering

B.1 What is “clustering”?

Clustering means grouping a point in a dataset into non intersecting subsets.

There is a variety of clustering algorithms to suit an even broader spectrum of problems, from those arising in machine learning to our case: interpret the data from a granular detector.
The Crystal Ball consists in 162 crystals[1] covering the solid angle. This configuration represents, from the conceptual point of view, a rather coarse and small problem; because of this, even a simple clustering algorithm such as *k-means* would be too elaborate.

B.2 Specificity of our problem

An interesting aspect of our problem is, also, that we don’t want data points coming from the atomic background mixing with the real signal: this would distort our spectrum and compromise our energy resolution and sensitivity.
The major reasons why the energy deposit won’t necessarily stay confined inside the crystal where the photon arrives are Compton scattering and pair production: both of these processes will not make the photon ”splatter” onto many neighbouring detectors.

B.2.1 Reasonable assumptions

Given the non-splattering nature of the interactions, we might reasonably assume the following to develop a clustering algorithm:

- Every interaction that is not the end of the event will continue in one only crystal.
- Interaction doesn’t jump crystals.
- Interaction points are ordered as non increasing in energy.

Clearly, this is a simplification: we could have a pair production event with both electron and positron escaping the origin crystal and we could also face a Compton scattered photon that

---

[1] Actually, not all of them are installed or counting for every run, but this will not disturb the development of a clustering algorithm for the detector.

jumps a crystal and ends up nearby. But these are supposed to be rare cases.
As it turns out, the assumption that the interactions are ordered as non-increasing in energy is the most problematic, as it has been already discussed in the ”Calculations” chapter, but it still holds true in the large majority of cases.

B.3 Nearest neighbour

The traditional way to cluster the Crystal Ball has always been to look at neighbouring crystal rings after selecting a centroid.
The version of the algorithm that I used when this work began has been inherited from P. Schrock [Sch15] and worked as follows:
For each event,

1. order the energy deposits from the largest to the smallest in a list;
2. pick the largest one: this will be the centroid;
3. look in the neighbouring crystal rings, up to order n, if there are energy deposits;
4. these deposits plus the centroid are a cluster; remove them from the list;
5. sum everything in the cluster: this will be the photon’s energy.
6. repeat from 2 until the list is empty;

B.3.1 Problem of the nearest neighbour

This approach is reasonable and there is nothing wrong with it, *unless the background level is very high*, either because of the number of background events or because of their energy relative to the interesting photons. Because my work focussed also on the part of the spectrum dominated by the atomic background, this algorithm proved to be not the best choice.
From the simulations it is possible to obtain interesting statistics about how many photons are generated by atomic processes. The expectation is, in general, to see all Poisson distributions, so the following fits have been performed with one even if, with very large values of λ, the Poisson and the Gaussian distribution are very similar.

Generated photon number After the atomic background has been normalized on the incoming beam energy distribution, the λ value for the distribution is 352.2. This number is larger than the one reported in [Sch15], which was 340 photons per event. This discrepancy can depend from the broadly larger energies considered here than in [Sch15] –the reasons for this are given in the main body of this text.

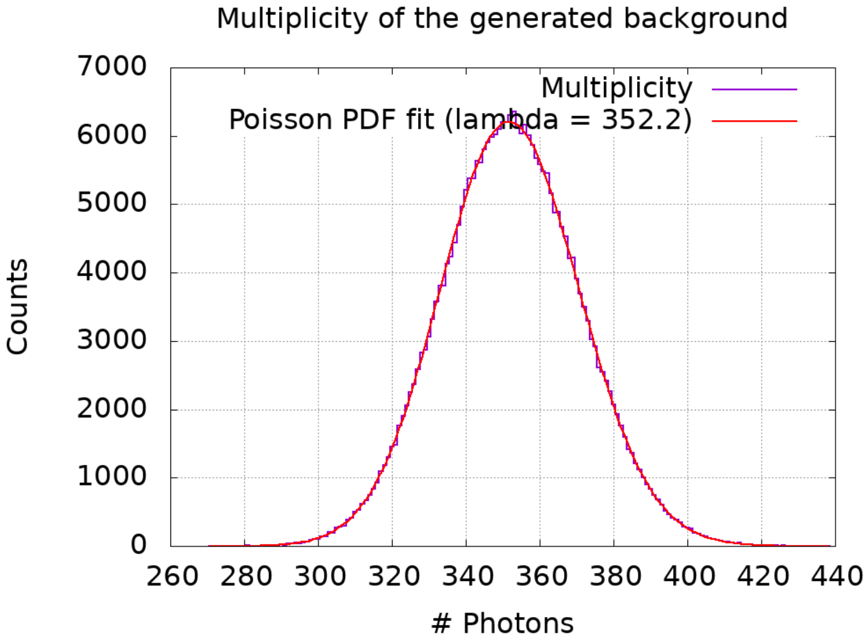

Figure B.1: This is the distribution of the number of photons *generated*.

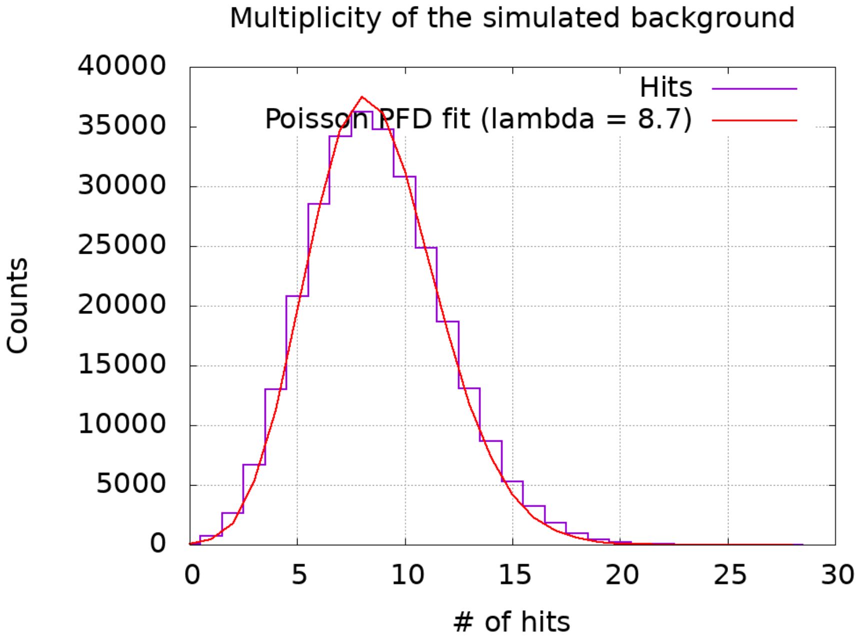

Figure B.2: This is the distribution of the number of hits per event in the Crystal Ball. Despite the very strong reduction of the atomic background, there is still significant activity in the detector generated by these processes.

Number of hits in the detector The vast majority of the photons generated by atomic processes are stopped in the shielding surrounding the target –that device was designed to do so, so this is reassuring. Nevertheless, some of those photons make it through and they are detected. The distribution for the hit multiplicity, so *before* clustering, has a λ value of 8.7, which in turn means that there is a considerable activity in the detector also just considering the remnants of the atomic background.

Number of clusters As already explained, one photon does not necessarily mean just one hit in a granular detector like the Crystal Ball and, indeed, running the clustering algorithm on the dataset causes the λ value of the multiplicity distribution to go down from 8.7 to 5.9, which also points towards slightly larger energy deposits.

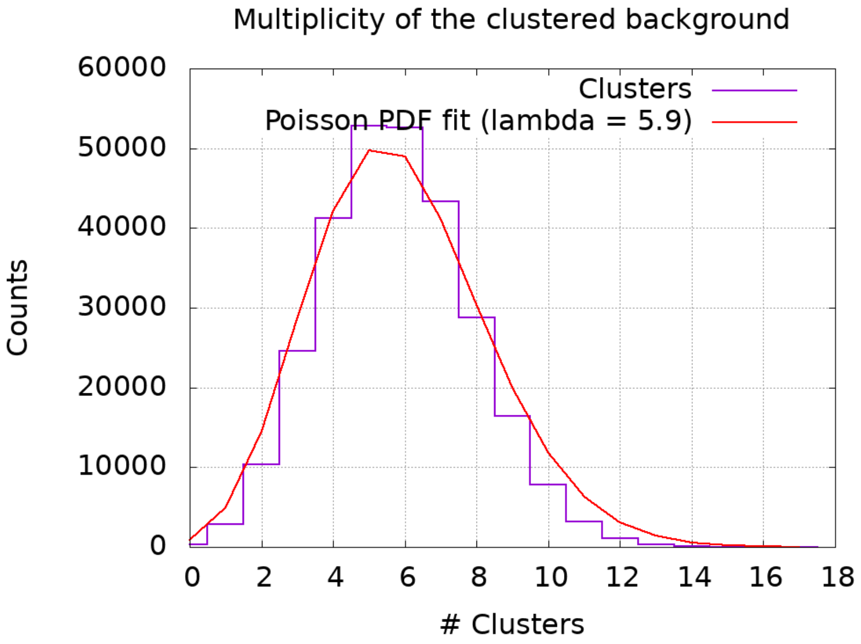

Figure B.3: This is the distribution of cluster multiplicity for the atomic background.

This number of photons turn out to be enough to decrease the resolution of the spectrum and add an exponential tail towards the *higher* energies to the peaks, an effect that is more pronounced the higher the neighbour order n is.

This happens because some background photons may be in one of the neighbour rings and are then summed up, shifting the energy of the cluster.

B.4 "Beading"

The major limitation of the nearest neighbour algorithm is the sum on the entire ring of neighbouring crystals, which isn't necessary if we assume that the photon doesn't splatter most of the times.

The mitigation I developed is to consider only the largest energy deposit on the first neighbour ring of the current deposit to expand the cluster. A. Horvat also suggested to decide how many steps this should continue before closing the cluster based on the energy of the candidate centroid.

The so-called "beading" algorithm works as follows:

For each event,

1. order the energy deposits from the largest to the smallest in a list;
2. pick the largest one: this will be the centroid, point at it;
3. look around the first ring of neighbours of the pointed deposit: pick the largest energy deposit *in the neighbourhood ring of crystals*;
4. add it to the cluster and remove it from the list;
5. point at the newly found crystal;
6. repeat from 3 until appropriate[1];
7. repeat from 2 until all deposits have a cluster;

And then sum everything in each cluster.

B.4.1 Number of iterations

The number of interaction with the detectors' crystals depends on the energy of the incoming photons. This fact had been originally investigated in [Lin13]. Because with the tools I already developed for the rest of the work it was very easy, I replicated the simulations, obtaining the same results for 100 kiloevents, as shown in figure 2.3.

Based on these simulation, it has been possible to calculate the best number of iterations the algorithm should run on an event by event base. Observing how the 90% quantile of the multiplicity distribution evolves as the energy increases, it is not too much of a stretch to fit the points with a root function with the appropriate index and use this to estimate a safe number of iterations. This relationship is shown in figure 2.5.

B.4.2 Advantages of the beading algorithm

The major advantage of this algorithm compared to the nearest neighbour described above is that it takes into consideration the non splattering nature of the interaction. For every iteration, in fact, just the most energetic photon is added to the cluster ignoring all the others that may be found at the same order of neighbourhood. If this is reminiscent of tracking, it is not a coincidence, although it should be noted that it is *not* really tracking: we'd need a better time resolution and also to take into consideration time information as well.

---

[1] See the chapter "Calculations" for the explanation of what "appropriate" means.

This results in cleaner clusters and better energy resolution, especially compared with a nearest-neighbour algorithm set at order 2, the previous "standard". The comparison of the two methods can be seen in figure 2.6.
As a consequence of this cleanliness, it is possible to ditch the arbitrary cut at 300 keV on all crystals, used previously [Sch15][1].

B.4.3 Disadvantages of this algorithm

Misidentification is greatly reduced but by no means completely eradicated. Also, the higher the energy, the more questionable the "non splattering hypothesis" becomes. Fortunately, in this work, I'm concentrating on a relatively low energy part of the spectrum, thus this limitation will not constitute a large problem.

---

[1] Before the Doppler correction.

Appendix C

Thresholds of the Crystal Ball

These are the thresholds retrieved from the data. Every line contains the information for three crystals: their index precedes the threshold in keV. For some crystals the threshold is not reported: this means that the crystal is either absent or it's not counting, thus making it impossible to estimate a threshold.

C 1	103.3 keV	C 2	106.2 keV	C 3	133.3 keV
C 4	129.0 keV	C 5	104.8 keV	C 6	87.2 keV
C 7	94.6 keV	C 8	88.5 keV	C 9	106.5 keV
C 10	128.7 keV	C 11	151.0 keV	C 12	152.9 keV
C 13	145.4 keV	C 14	128.3 keV	C 15	107.1 keV
C 16	90.1 keV	C 17	78.1 keV	C 18	77.9 keV
C 19	77.7 keV	C 20	81.7 keV	C 21	95.8 keV
C 22	114.2 keV	C 23	136.5 keV	C 24	189.5 keV
C 25	229.4 keV	C 26	211.7 keV	C 27	187.3 keV
C 28	139.6 keV	C 29	119.0 keV	C 30	94.5 keV
C 31	77.4 keV	C 32	71.6 keV	C 33	70.5 keV
C 34	70.9 keV	C 35	71.2 keV	C 36	74.2 keV
C 37	86.2 keV	C 38	104.6 keV	C 39	134.9 keV
C 40	162.3 keV	C 41	300.1 keV	C 42	277.9 keV
C 43	288.7 keV	C 44	165.8 keV	C 45	136.6 keV
C 46	104.7 keV	C 47	87.9 keV	C 48	77.3 keV
C 49	64.0 keV	C 50	66.7 keV	C 51	65.5 keV
C 52	66.6 keV	C 53	71.4 keV	C 54	79.1 keV
C 55	96.3 keV	C 56	121.9 keV	C 57	141.6 keV
C 58	211.3 keV	C 59	259.2 keV	C 60	353.9 keV
C 61	380.9 keV	C 62	356.1 keV	C 63	260.5 keV
C 64	210.9 keV	C 65	136.5 keV	C 66	117.9 keV
C 67	95.2 keV	C 68	80.7 keV	C 69	72.2 keV
C 70	77.1 keV	C 71	61.1 keV	C 72	64.2 keV
C 73	63.2 keV	C 74	64.8 keV	C 75	77.6 keV
C 76	103.8 keV	C 77	0.0 keV	C 78	141.6 keV
C 79	153.4 keV	C 80	291.4 keV	C 81	0.0 keV

C 82	0.0 keV	C 83	66.3 keV	C 84	77.6 keV
C 85	59.1 keV	C 86	105.2 keV	C 87	131.9 keV
C 88	170.2 keV	C 89	296.1 keV	C 90	364.4 keV
C 91	371.7 keV	C 92	361.4 keV	C 93	259.9 keV
C 94	214.6 keV	C 95	152.3 keV	C 96	117.7 keV
C 97	95.3 keV	C 98	81.4 keV	C 99	73.3 keV
C 100	67.3 keV	C 101	0.0 keV	C 102	64.2 keV
C 103	0.0 keV	C 104	67.6 keV	C 105	71.2 keV
C 106	79.4 keV	C 107	90.5 keV	C 108	125.7 keV
C 109	155.8 keV	C 110	212.6 keV	C 111	264.0 keV
C 112	293.3 keV	C 113	283.7 keV	C 114	298.2 keV
C 115	184.1 keV	C 116	136.3 keV	C 117	106.4 keV
C 118	86.1 keV	C 119	75.6 keV	C 120	66.7 keV
C 121	67.4 keV	C 122	65.8 keV	C 123	76.5 keV
C 124	85.5 keV	C 125	106.1 keV	C 126	136.7 keV
C 127	185.8 keV	C 128	209.1 keV	C 129	210.8 keV
C 130	248.3 keV	C 131	210.0 keV	C 132	156.8 keV
C 133	119.4 keV	C 134	100.9 keV	C 135	80.2 keV
C 136	44.9 keV	C 137	79.1 keV	C 138	70.9 keV
C 139	70.8 keV	C 140	80.2 keV	C 141	95.6 keV
C 142	118.4 keV	C 143	156.8 keV	C 144	166.4 keV
C 145	166.8 keV	C 146	166.4 keV	C 147	129.4 keV
C 148	104.8 keV	C 149	90.2 keV	C 150	78.2 keV
C 151	78.7 keV	C 152	77.8 keV	C 153	89.2 keV
C 154	106.1 keV	C 155	128.6 keV	C 156	130.7 keV
C 157	130.8 keV	C 158	106.1 keV	C 159	88.9 keV
C 160	89.1 keV	C 161	105.3 keV	C 162	105.1 keV

Appendix D

R3BRoot

R3BRoot is a library, based on CERN's ROOT, which is aimed at facilitating the analysis and simulation of everything about R^3B: on top of ROOT's classes, it offers detector geometries and "digitisation" instruments for realistic simulations, as well as tools for detector calibration and on-the-fly data visualization. It also provides some scripts[1] as examples for the various tasks the library can be used for.

The interest of this work in R3BRoot lies solely in its simulation assistance; besides, actually using R3BRoot as a library lead to the discovery of a number of bugs that were not immediately apparent due to ROOT's unique way of dealing with linking executables.

D.1 FairSoft and FairRoot

R3BRoot depends from another library, FairRoot, and a software suite called FairSoft.

D.1.1 FairSoft

FairSoft is a collection of libraries that are necessary or handy for the functionalities developed in the ROOT specializations used by GSI/FAIR collaborations, such as FairRoot and R3BRoot. Its scope is very wide, partly forcibly so because of the variety of the UNIX-like operating system landscape and the libraries bundled therein, partly because some libraries don't do an excellent job at compatibility between versions or, simply, the ROOT specializations may rely on a functionality of some library that may disappear in a later version.

As of the version used by this work, this software suite can offer:

- CMAKE
- Google's Test Framework
- GNU Scientific Library, "the gsl"

---

[1] In ROOT jargon they are called "macros", but it is a misnomer in this case: a *macro-instruction* is a programming statement that is later expanded in many other instructions, such as a preprocessor directive can be; a ROOT "macro" is in effect a whole program written in a subset of standard C++ that is later interpreted or just-in-time (JIT) compiled into an executable –they are equivalent to omitting the `main()` function from a program body and possibly some library initialization statements; effectively: scripts.

- ICU library
- C++-BOOST
- Pythia, version 6 and 8
- HepMC
- Xerces
- GLU graphic library
- GEANT, versions 3.21 and 4 (usually close to the latest minor)
- CERN's ROOT
- G4Py
- Pluto
- VGM
- Millipede
- ZeroMQ
- Protocol Buffers (ProtoBuf)
- Flatbuffers
- MessagePack
- Nanomsg

Describing what each of these libraries do is way beyond the scope of this Thesis; suffices to say that it is a very large collection of software that needs to be compiled from source –some optimization may be obtained if the machine uses has a particularly exotic architecture. In the case of this work, though, only the libraries that weren't provided by the operating system's repository were installed, to save time and disk space. The necessary modifications to the installer scripts were minor and have not been submitted for review to the software maintainers.

D.1.2 FairRoot

FairRoot is a library developed in-house at GSI which functions as a common base for all the collaborations' specific libraries. In particular, it provides mechanisms to execute the simulation and set the Monte Carlo engine without too much hassle, it provides the base classes for active and passive detectors and the base classes for storing the output of the simulation. Finally, it provides read and write interfaces.

R3BRoot is coded upon FairRoot.

Appendix E

`sbkg`

The name `sbkg` stands for "simulate (the) background", although the program is a fully fledged simulator for R^{3}B detectors and, also, some additional ones that have been added in the scope of other projects I followed, on the side of this work. This program utilizes the libraries I described in the previous appendix in order to perform the simulation, but skips some pre-settings of the Monte Carlo engine provided by R3BRoot which were, at the time, rather opaque and created some issues[1].

E.1 Simulation setup

The user can setup the simulation via the command line and with a configuration file.
At the command line there are several options to turn on and off the magnetic filed, the magnet itself[2] and each detector.
The configuration file also allows to directly set more aspects of the simulation, such as the various processes that have to be taken into account by the Monte Carlo engine and, also, it's easier to repeat the simulations with the same settings, given that everything is determined by the configuration file.

E.2 R3BRoot extensions

As mentioned before, for this work it has been necessary to extend R3BRoot in order to include the correct and dutifully detailed geometry of the target chamber, target wheel and most importantly the shielding that is supposed to reduce the atomic background. Alongside to this, I extended R3BRoot also by adding two "mock" tracking detectors, whose geometry can be specified at construction and whose main point was to provide positional information of passing

---

[1] Stray, unphysical protons created in the magnet and not stopped due to some (necessary) simplification of the magnet's inner geometry: for instance, the coils of the new magnet, GLAD, are not represented in the simulation because nothing of interest is supposed to hit them and show up in the detectors, but if the Monte Carlo engine transports a particle there, it will not be stopped because that region is filled with just air in the virtual world.

[2] The magnetic field and the magnet's bulk are two completely different objects in FairRoot and GEANT; although baffling at first, this is a sound technical choice, if anything because it provides more flexibility to the simulation.

particles and stop them, if needed.

E.2.1 Improved target geometry

Although R3BRoot did contain the geometries of the target and the target chamber, for some reason they were not detailed enough and, more importantly, they didn't include the target wheel and the shielding around the target. The geometries used in this work have been handed over by Dr. D. Rossi. Initially, I put them in the same directory tree as the rest of the R3BRoot code and operated on my own branch of the revision control system. This approach, though valid while being maintained, would not have aged well, therefore I chose to transfer them in one of the directories I used for the software developed during the course of this and other works and would be "grafted" onto a stock R3BRoot.

E.2.2 Tracking detectors

In the course of P. Müller Bachelor Thesis work, relating to an experimental proposal for the investigation of the dipole response of Helium 6 [6He] and other drip-line nuclei, emerged the need to retrieve the position of the particles during the simulation to track their movement.
Because of how the Monte Carlo engine is successively wrapped in several classes in Fair- and R3BRoot, obtaining and saving the information directly was not a trivial task and it turned out to be easier to create a detector that could be placed at will in the simulation, with an appropriate extension, and then record the points of interactions. To achieve this, I developed the two "mock" tracking detectors `rattleplane` and `stopperplane`, which respectively produce a position information when a particle passes through and produce the same data while extinguishing the particle.
To control this point of interaction, these detector can also be specified with one of the materials available in R3BRoot and, also, are able to deliver the momentum and energy loss of the particle at the interaction sites. This latter feature was not of immediate use, but it was very simple to develop and, once included, it gave the two detectors the ability of being used as prototypes of time of flight walls in later simulations.

Atmosphere At the end of the day, though, a more thorough tracking performance for the proposal could be achieved by turning the whole world of the simulation into sort of a detector, by changing the filling material to air[1]. This is usually avoided because of the large amount of compute time spent on letting the particles interact with the air and the completely negligible energy loss, but this feature was very useful for a thorough tracking, in a much more practical

---

[1] In the version of the software I used, the default was vacuum.

way than specifying tens of `rattleplane` detectors –although the run time of the simulation was affected.

After the simulation, the points were collected by a program that produced a script for a CAD software[1] for visualization.

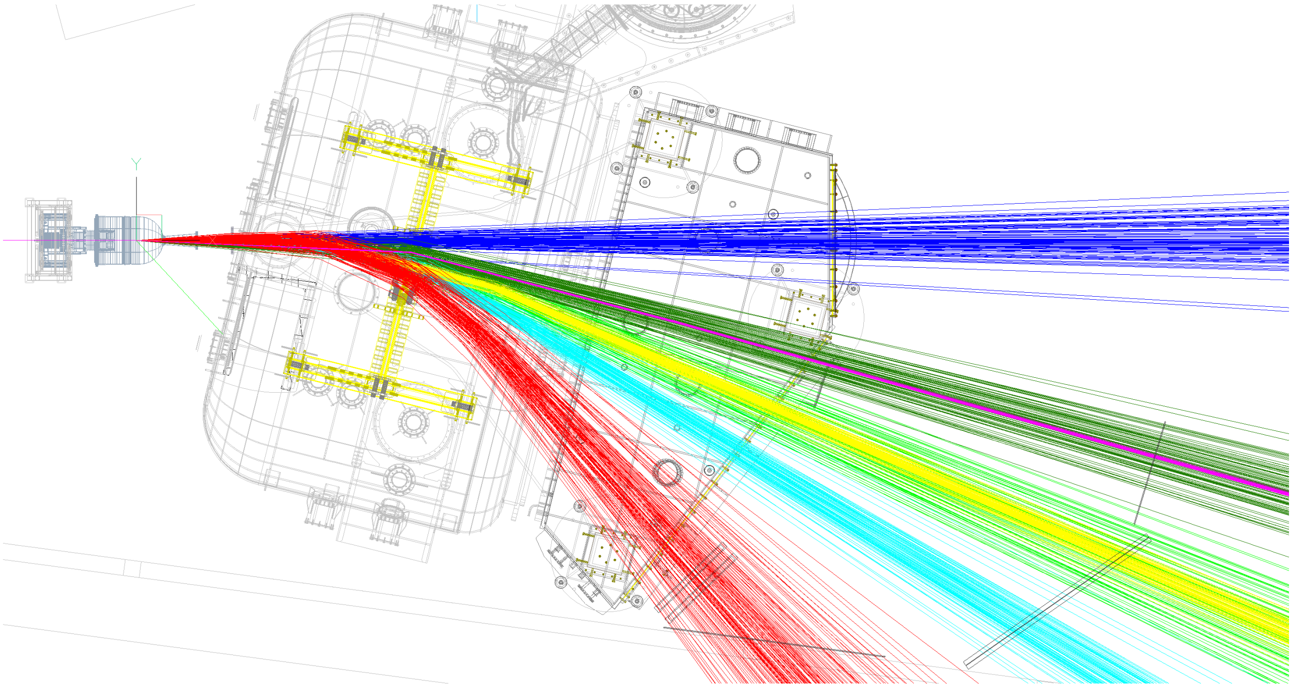

Figure E.1: Different particle species travelling through the R^{3}B experimental setup (Phase-0) for a proposed ^{8}He experiment. The tracks are extracted by letting them interact with the air in the cave and then recording all the coordinate of the interactions. The various colours denote different particle species: neutrons are in blue, protons in red, α particles are in yellow and, following the same path (they have the same rigidity), ^{2}H ions are in bright green; light blue denotes ^{3}He nuclei, ^{3}H nuclei are coloured in dark green and, following the same path the non reacted beam is depicted in fuchsia.

These two detectors have also been placed in an independent directory tree from the stock R3BRoot and are installed later, after applying a patch to the R3BRoot code (which is expected to be portable for a long time, since it only adds two detector indices to an enumerative data structure).

---

[1] Brycsys' BrycsCAD, which is one of the rare programs of this kind to be fully compatible with GNU+Linux operating environments and, also, offer a complete features and user support.

Appendix F

`abkg`

The name `abkg` stands for ”atomic background” and the program is aimed at calculating just that.
The program has been developed in the ’80, originally, and in Fortran, by R. Holzman at GSI and later modified by Prof. H. Scheit[1] in 2001 –as the leading comments in the source code state.
The program `abkg` is able to calculate a number of processes that happen in the target. As written in the main body of this thesis, these processes are:

- Primary bremsstrahlung
- Secondary electron bremsstrahlung
- Radiative electron capture
- Target X-rays
- Isotropic gamma

These processes are turned on and off with a bit array; in what follows, there’s a little explanation of what they are. Going into the details of how `abkg` calculates the cross sections is beyond the scope of this work: please read the code of the program instead [ABKG].

Primary bremsstrahlung This part of the atomic background is due to the low energy Coulomb scattering of the projectiles (which are completely ionized when they enter the target) with the nuclei of the target, in this case ^{132}Sn entering ^{208}Pb. This interaction causes the projectile to lose kinetic energy and, thus, experience a negative acceleration: because it is charged, the deceleration causes the projectile to radiate. According to [Sor05], a number of different approaches have been tried to theoretically describe this process in classical, semi-classical and quantum mechanical terms for relativistic heavy ions interacting with matter.
In the end, the William-Weizsäcker model, also based on the exchange of virtual radiation[2], proved to be the closest to measurements. In this picture, the expected virtual radiation has a nearly flat spectrum until a cutoff energy is reached: before this, the scattering of virtual

---

[1] Who is also part of the work group where this work have been performed.

[2] This is also one of the competing models used to describe Coulomb excitation, but it has been superseded by Bertulani and Baur’s model in that case at least.

photons is classical and is understood to happen between photons at once on rigid particles. After the cutoff, set by the wavelength of the photons reducing under the nuclear radius[1], the scattering happens on a single photon basis but also the cross section becomes negligible in favour of other processes, such as pair creation.

As the reader might have already noticed by this point, the underlying process that is used to explain the bremsstrahlung is very similar to the one that will lead to Coulomb excitation: in this picture, the process is indeed a continuum but when the energy of the virtual photons is high enough the projectile can be excited and, thus, the process is no longer "background" as such but it is interesting physics for this work. In principle, `abkg` only considers background photons below 3 MeV, well below the first excited state of ^{132}Sn, thus the bremsstrahlung is a completely elastic process.

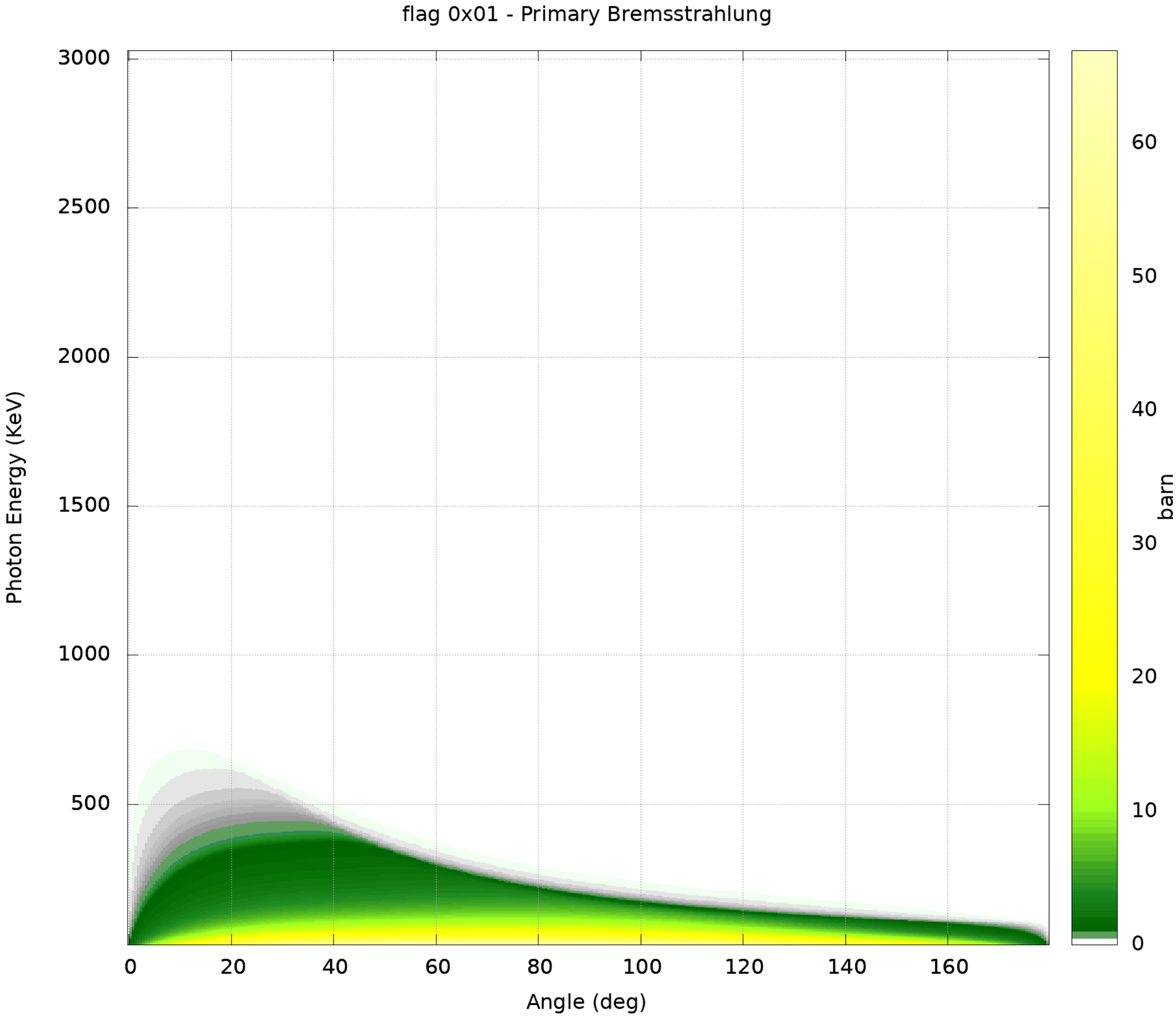

Figure F.1: The calculated doubly differential cross section $\frac{d^2\sigma}{\partial\theta\partial E}$ calculated by ABKG for the primary bremsstrahlung (PB).

---

[1] In [Sor05], the minimum impact parameter is used: in this case, the threshold wavelength is the sum of the two atomic radii.

Secondary electron bremsstrahlung The passage of very fast, heavy and positively charged particles through a material will drag away electrons from their atoms and accelerate them through the material. These electrons, known as secondary electrons, then, will also experience the very well known radiative deceleration and mostly be stopped in the target (some may escape, but they will be stopped by the shielding around the target and have very unlikely to reach the detector).

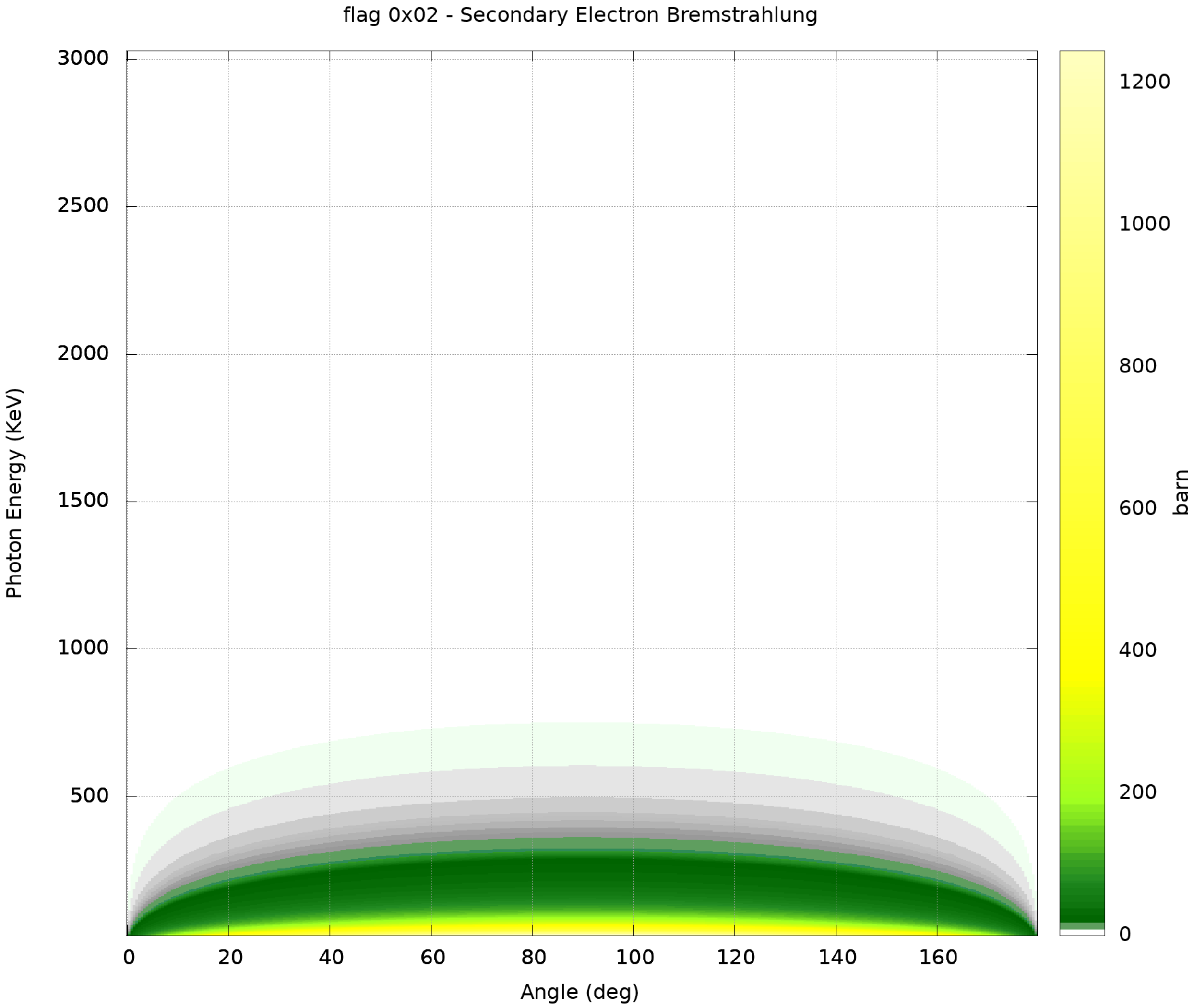

Figure F.2: The calculated doubly differential cross section $\frac{d^2\sigma}{\partial\theta\partial E}$ calculated by ABKG for the secondary electron bremsstrahlung (SEB).

Relativistic electron capture When an ion flies through matter, it can happen that an electron is captured in its electric field and, by falling in the ion's potential well, emits a photon. An exhaustive review of the theory behind this process, or at least for the electrons captured in the K-shells, can be found in [Gla97]. An important characteristic of the atom involved is individuated by the article in the Compton profile; this defined as the momentum distribution of electrons in the scattering medium [SaUm16]. The program `abkg` calculates this background separately for captures in the K-shells and the L-shells[1], and to do requires the Compton Profile of the target to be specified in the configuration file[2] for the target material.

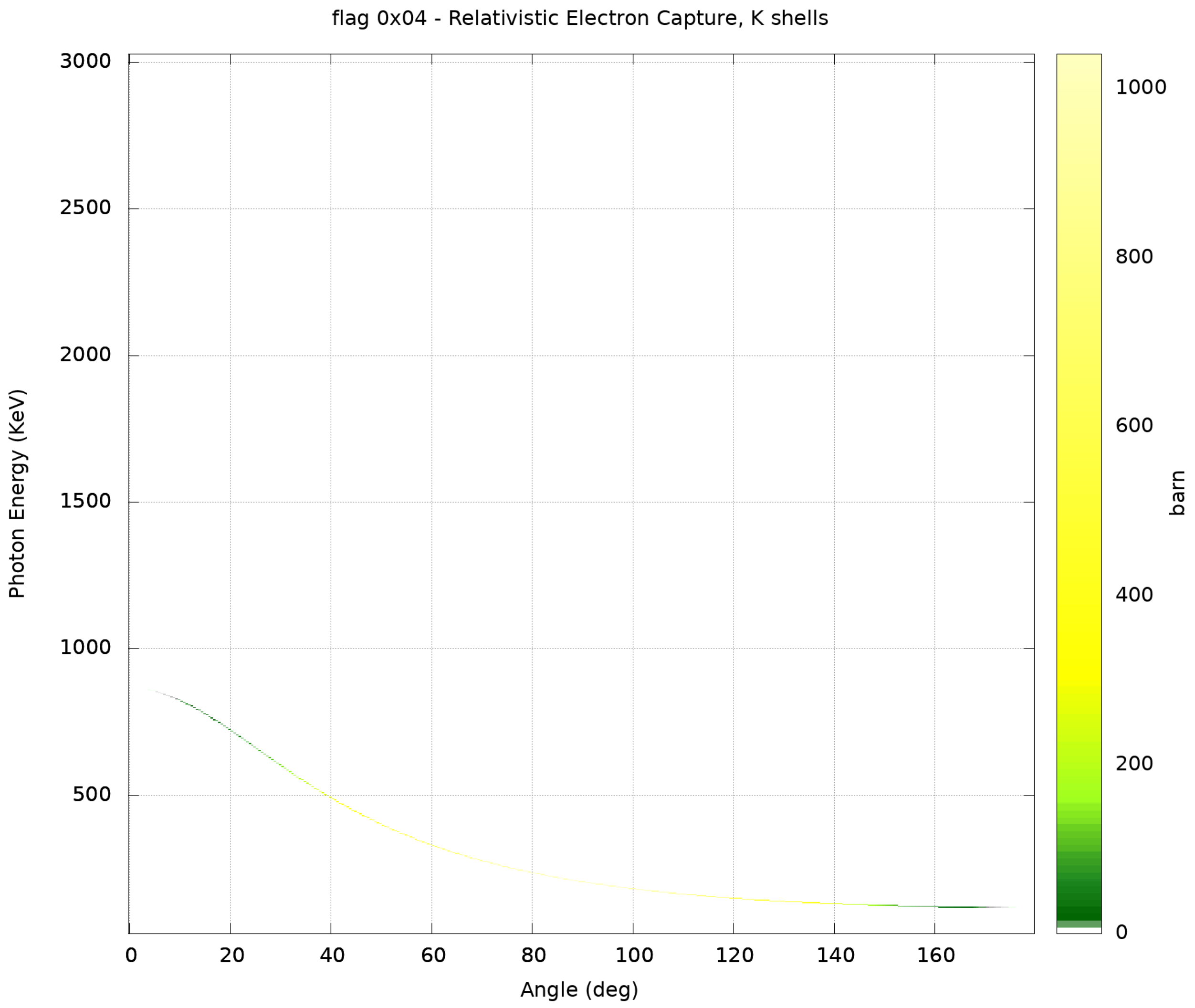

Figure F.3: The calculated doubly differential cross section $\frac{d^2\sigma}{\partial\theta\partial E}$ calculated by ABKG for the relativistic electron capture on the K-shell (REC-K).

---

[1] Following the IUPAC X-Ray notation, K- and L-shells indicate the innermost atomic shells, corresponding to the principal quantum number $n = 1, 2$ –thus the ones with a larger binding energy and the source for most energetic photons.

[2] Or at the prompt. The program will read in a predictable pattern from the standard input which, on UNIX-like systems, can be easily redirected to a file.

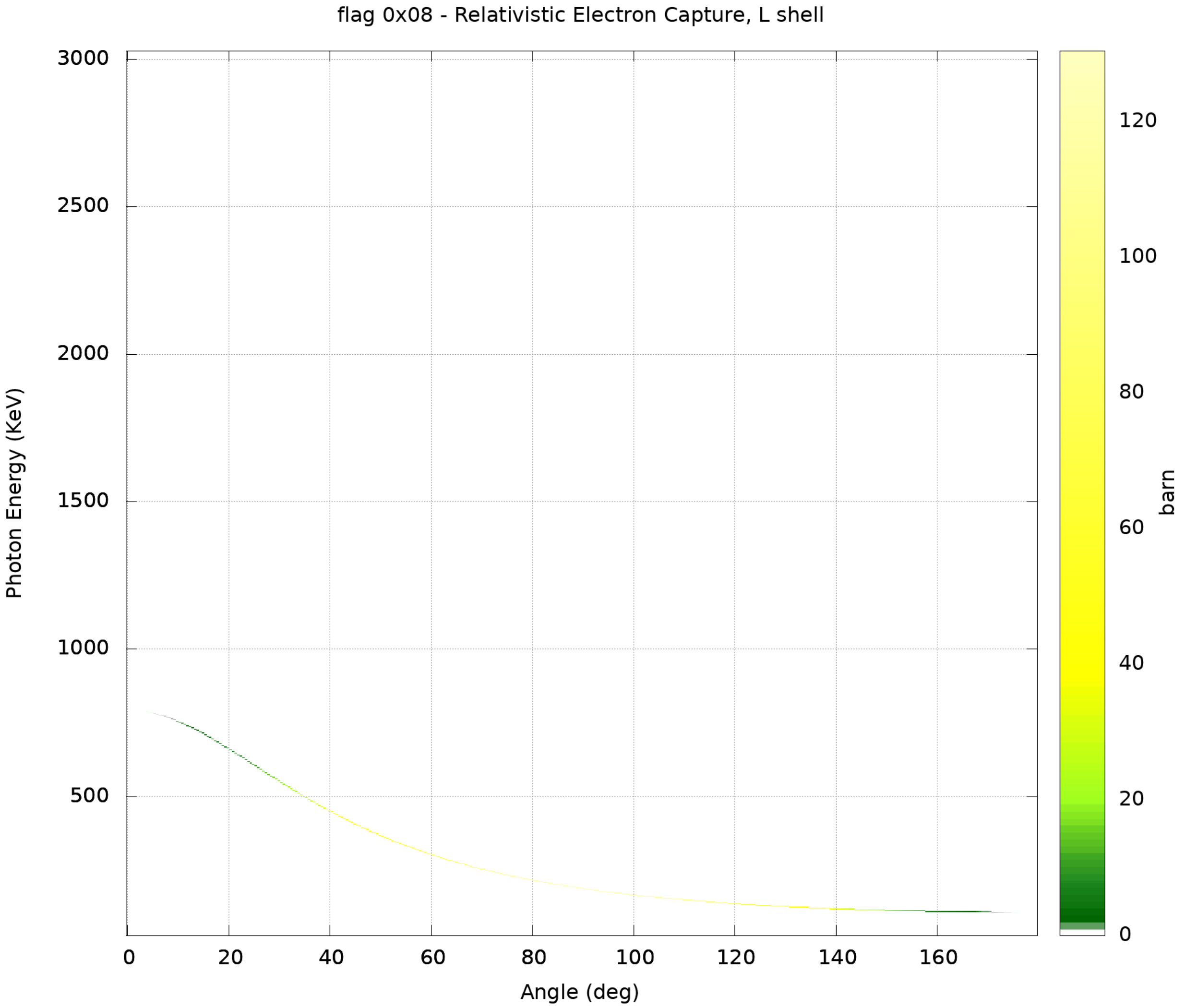

Figure F.4: The calculated doubly differential cross section $\frac{d^2\sigma}{\partial\theta\partial E}$ calculated by ABKG for the relativistic electron capture for the L-shell (REC-L).

It is worth noting that this process is the only one that has a Doppler shift in the direction of the beam, since the photons are emitted by the ions. This fundamental characteristic is taken into account by ABKG.

Target X-rays This is also a familiar process, in this case mediated by heavy ions flying through the material instead of the more usual energetic electron striking a metal plate. These characteristic X-rays are relatively high energy photons emitted by the electrons form the target's atoms which decay onto the innermost shells, left vacant either by displacement of electrons that were previously there (and now are emitting secondary bremsstrahlung somewhere else).

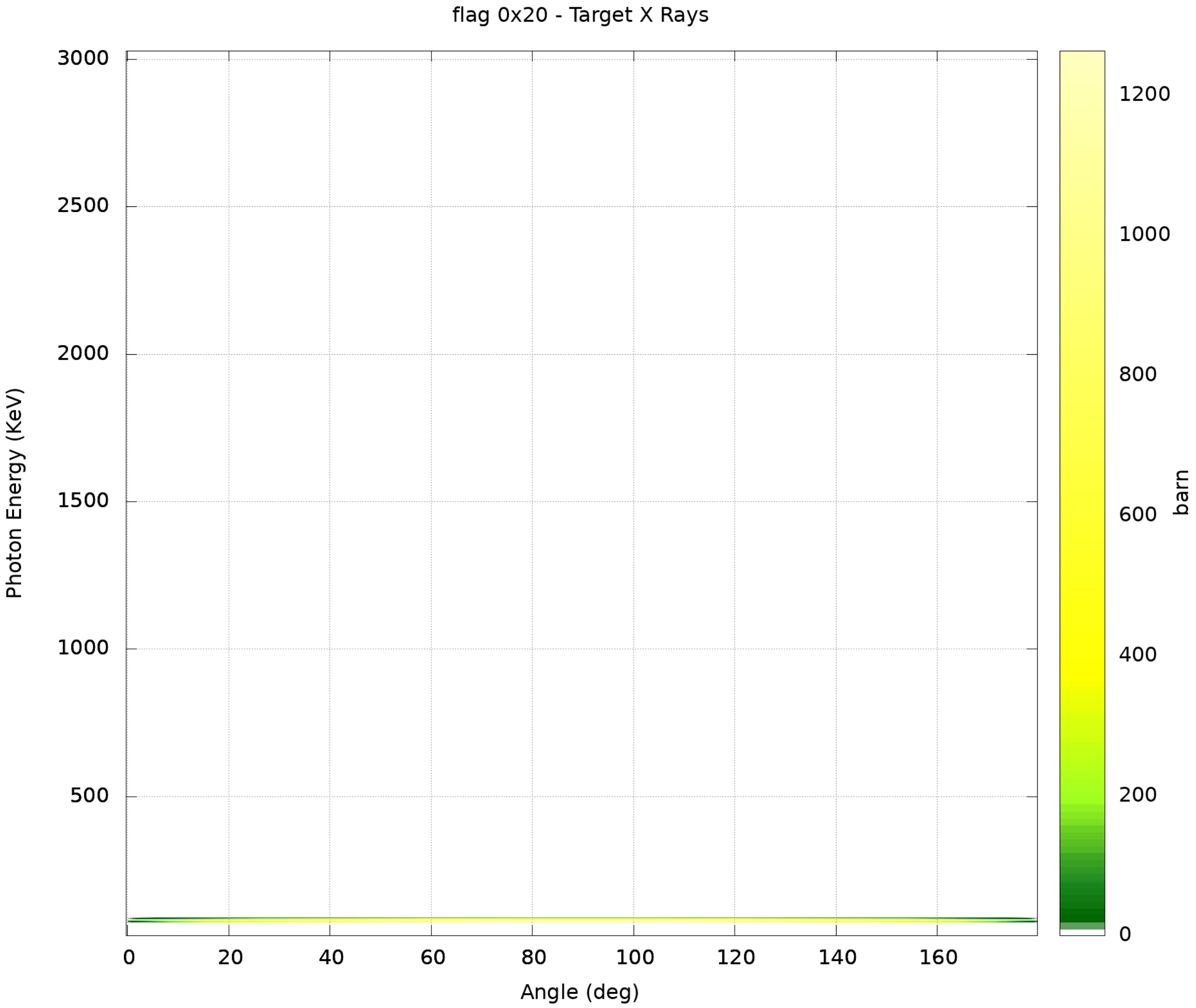

Figure F.5: The doubly differential cross section $\frac{d^2\sigma}{\partial\theta\partial E}$ calculated by ABKG for the target X-Ray emission.

As one may notice from the plot in figure F.5, this process contributes a very large amount to the background but it does so only below 200 keV. Because in general in that region the further contributions of the background are enormous and, also, some crystals of the Crystal Ball have an higher threshold, this part of the background effectively should not contribute to the analysis presented in this work. Nevertheless, it is included in what `abkg` calculates.

F.1 Atomic background spectrum breakup

Now that the doubly differential cross section distributions are known, how do they look when they are passed through the transport engine?

Primary bremsstrahlung Despite the adjective in the very name of this process, it turns out to be not the dominant source of atomic background for the experimental condition of S412

–at least, according to `abkg`. This process, as can be seen in figure F.1, is not symmetrical and offers an increased cross section in the forward half of the Crystal Ball.

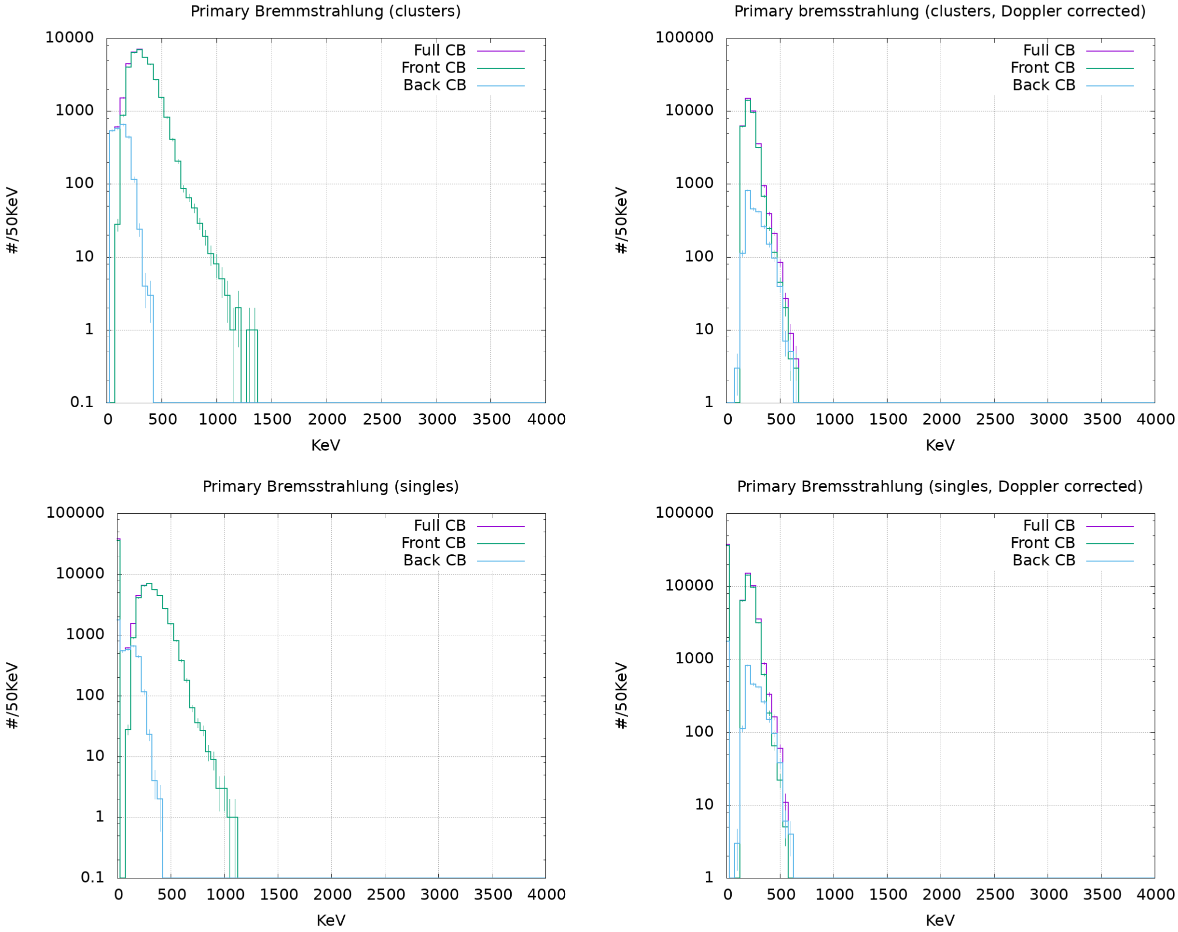

Figure F.6: The spectra resulting from the simulation of the Primary bremsstrahlung, as calculated by `abkg`.

Secondary electron bremsstrahlung Despite the adjective (again), this is the dominant contribution to the atomic background, by two orders of magnitude. This contribution is completely isotropic, as shown in figure F.2 and at rest in the laboratory's frame of reference, as can be seen by how the sample behaves under the Doppler correction.

An interesting feature missing, which should already have been apparent to the reader, is the absence of the "hump" at very low energies. This comes from other contributions, depicted below.

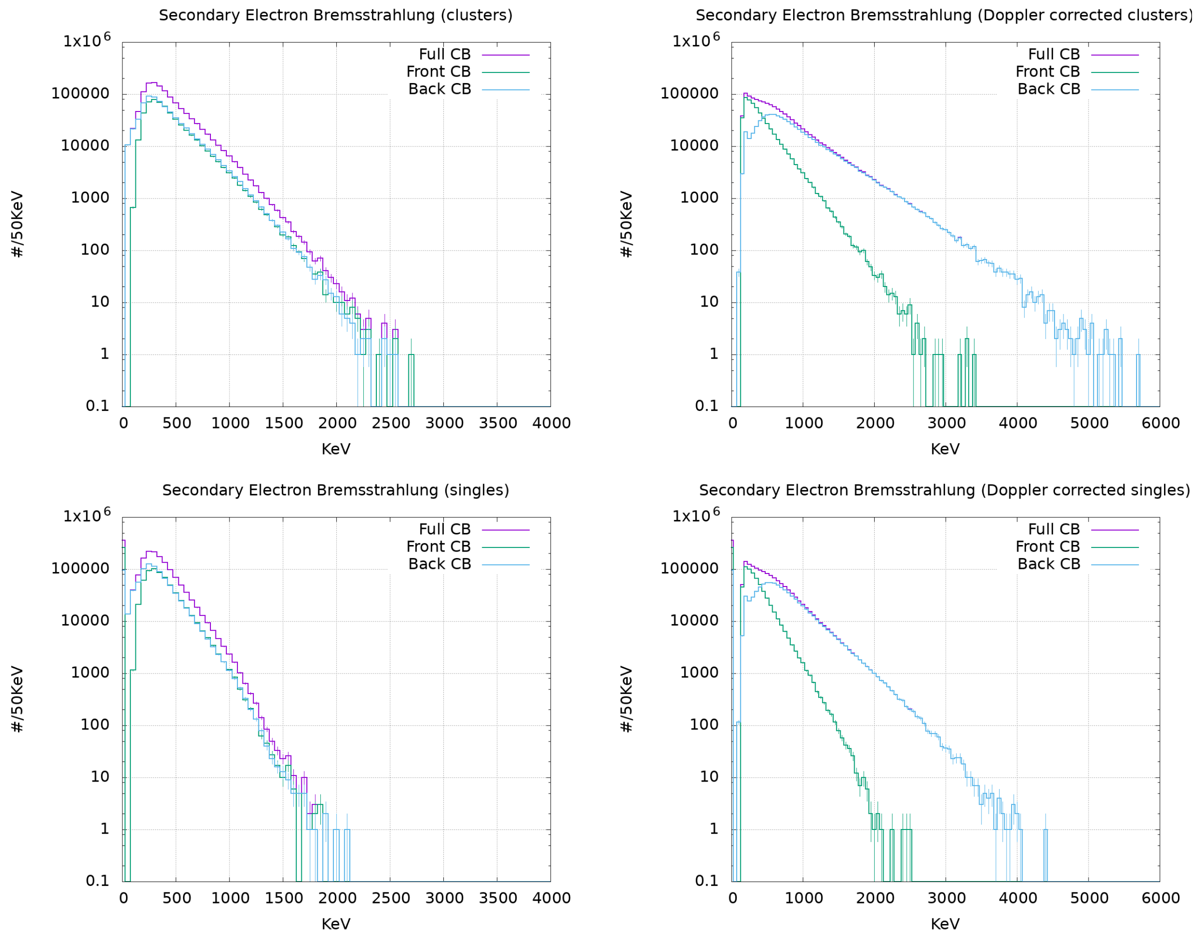

Figure F.7: The spectra resulting from the simulation of the Secondaty electron bremsstrahlung, as calculated by `abkg`. Notice the behavior under the Doppler correction, indicating a source at rest in the laboratory, and the absence of the characteristic very low energy peak and hump.

Relativistic electron capture The relativistic electron capture, both for K and L shells, looks to be the second process by contribution. In figures F.3 and F.4 it is shown a very marked angular dependence and a very very narrow energy distribution. These features are consistent with a process that *is* Doppler shifted and fairly monochromatic –as in: one definite energy for K- and L-shells, but different ones. This is to be expected, since electrons are "falling" onto the same energy level (of the projectile, not the target) from a quasi free state, by comparison.

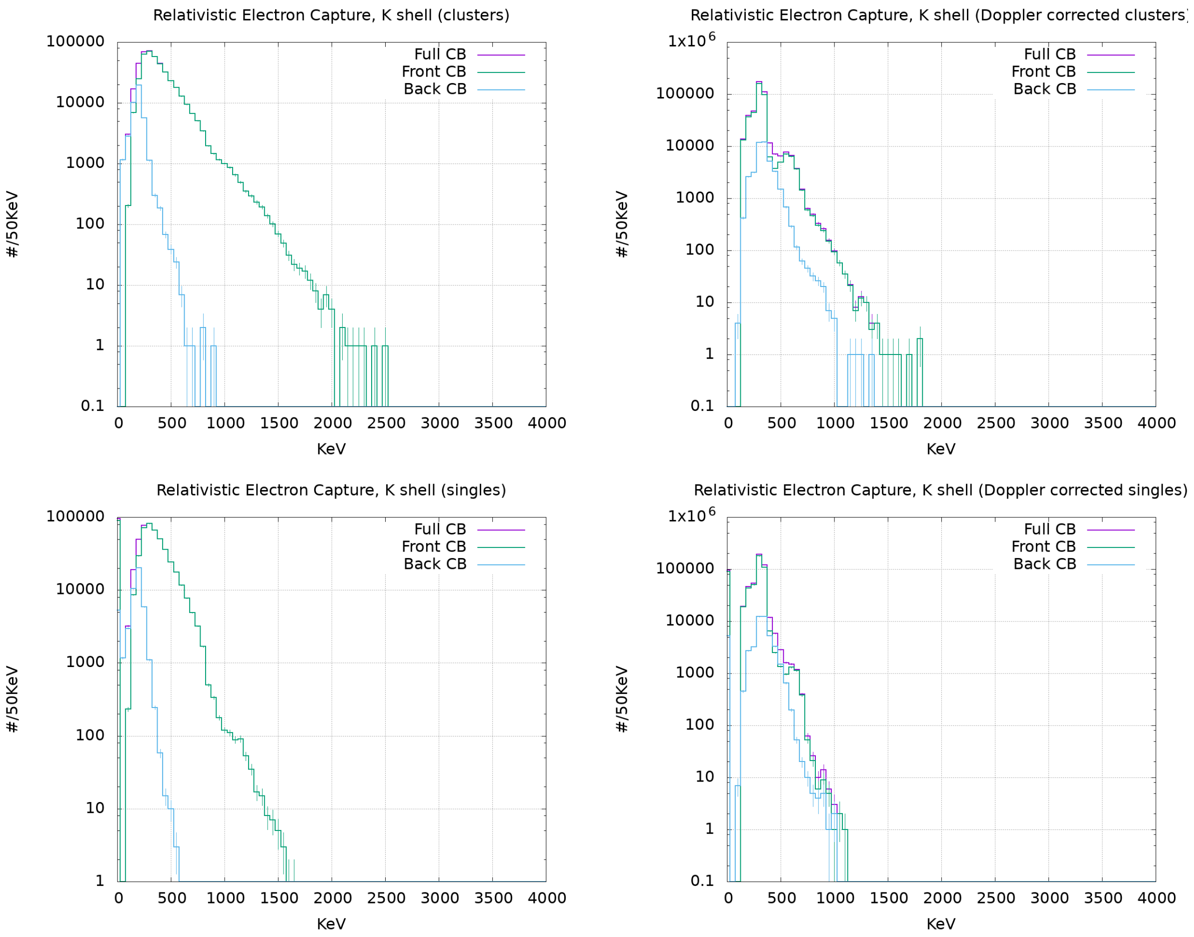

Figure F.8: The spectra resulting from the simulation of the relativistic electron caption on the K shell, as calculated by `abkg`. Notice that the spectrum acquires a structure, with a discernible peak (at least in the front of the CB), under the Doppler correction, indicating a process which is in motion relative to the laboratory.

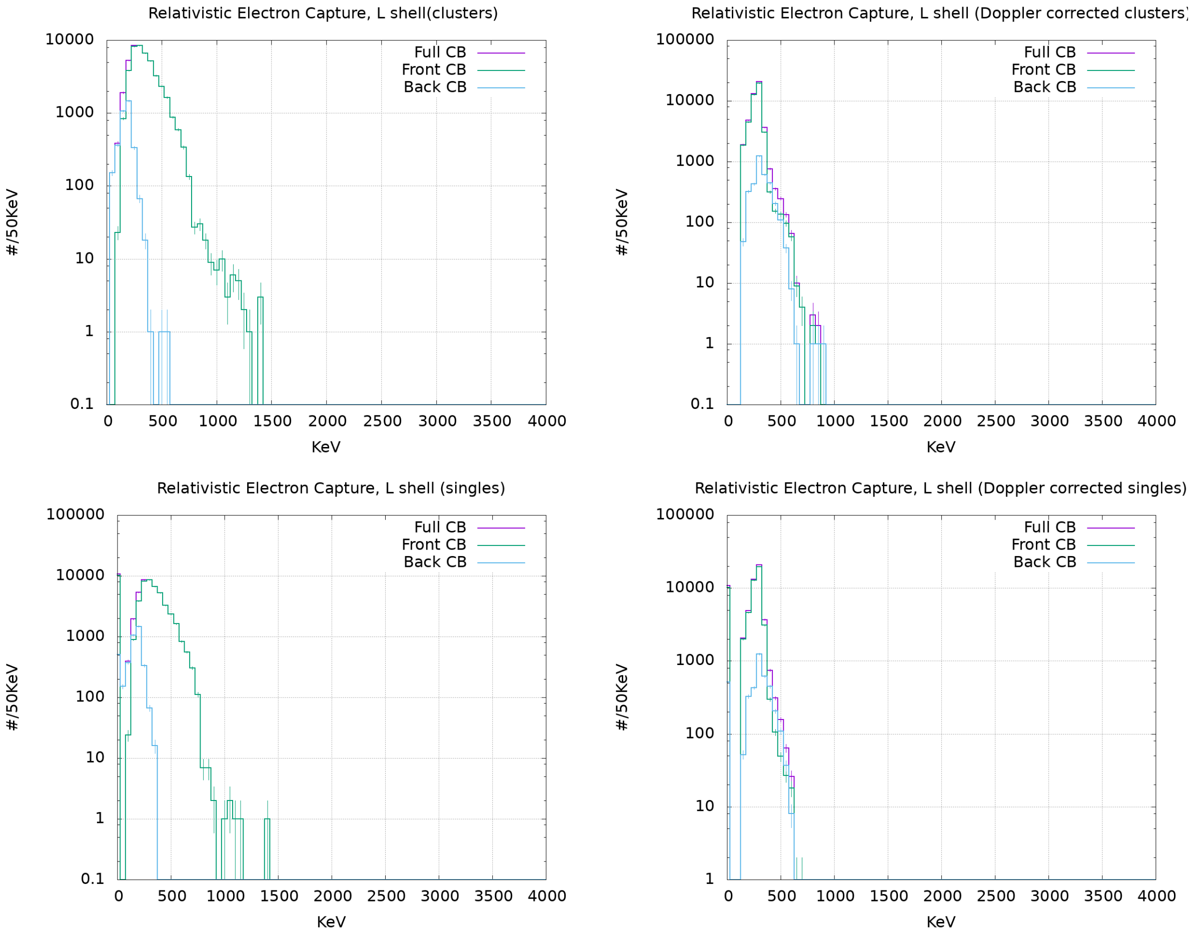

Figure F.9: The spectra resulting from the simulation of the relativistic electron caption on the K-shell, as calculated by `abkg`. Notice that the spectrum acquires a structure, with a discernible peak (at least in the front of the CB), under the Doppler correction, indicating a process which is in motion relative to the laboratory. Compared with the K-shell relativistic electron capture, this process is lower in energy, as it should be expected.

These processes are very likely to be the source of the ”peak and hump” visible in the atomic background simulation, but not really in the data. This might suggest that the cross section for these processes are slightly overestimated. At the end of the day, no particular action has been taken to scale or remove this contribution because, in the region affected, the atomic background is so dominant that hopes to see events above the sensitivity are very scarce anyway.

Target X-rays This is a rather minor, low energy contribution to the atomic background and, of course, it is at rest in the laboratory frame of reference.

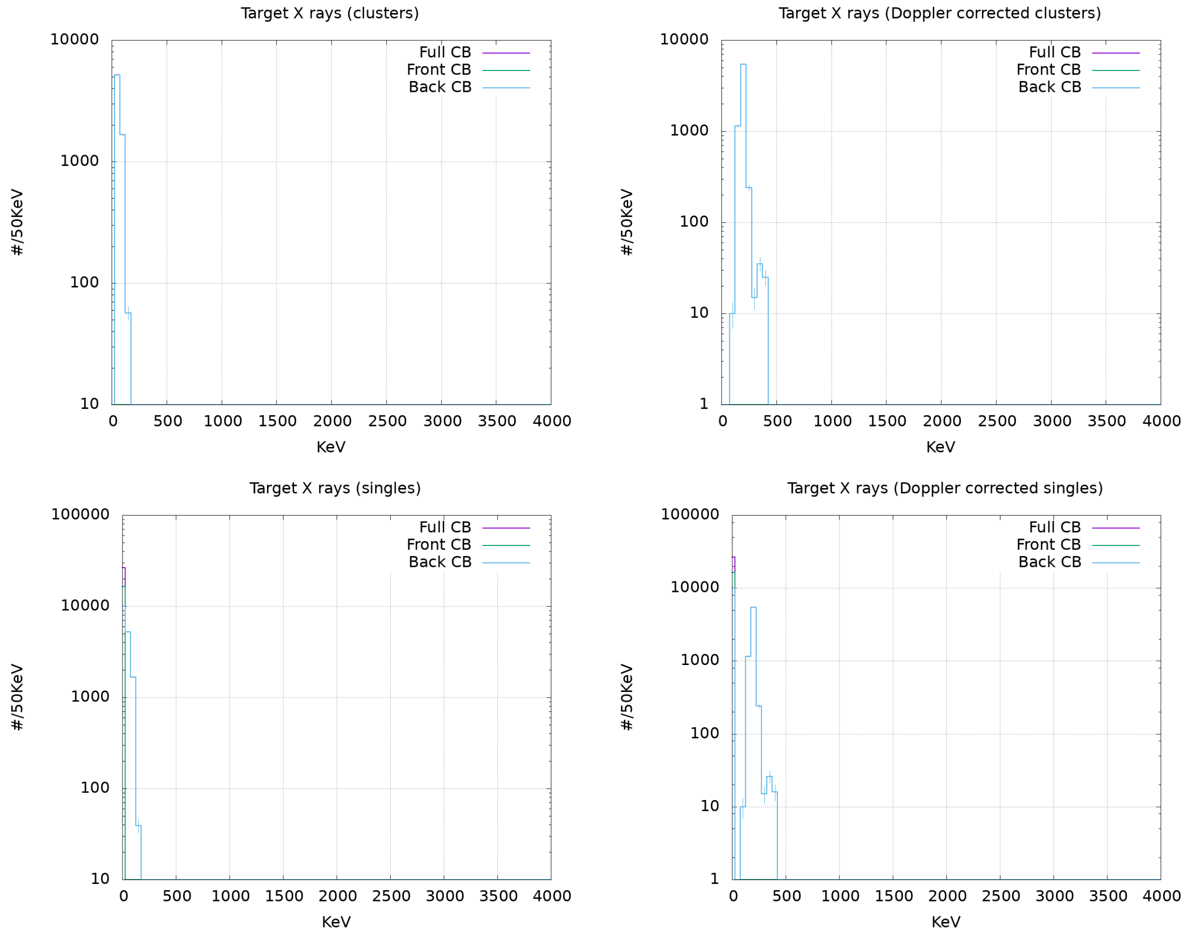

Figure F.10: The spectra resulting from the simulation of the target X-rays, as calculated by `abkg`.

Appendix G

Trigger flags and Tpat

Not every process will show up in all detectors observing the experiment: if, for example, a reaction that doesn't produce neutrons happens, it is reasonable to expect that the quantity of energy deposited in the neutron detector, in the time window when a neutron is expected to arrive in it, will be modest and, in general, very distinctly lower than when a neutron actually interacts with it. With this knowledge, the trigger for the neutron detector is set and the DAQ will check it and record it if there have been other triggers.

By observing the so-called trigger pattern, it may be then possible to impose a first selection on the events: this is why the various triggers are saved together with the detector data in the event structure, under the name `Tpat`, as a 16 long bit array. Each experiment, depending on how the DAQ is set for it, will have a different ordering of the bits and those bit, thus, will have different meanings. The following schema is relative to the S412 experiment upon which this work developed:

```
         MODULE IN SLOT 20:

 1 Min Bias          * 0 0 0 0     0 0 0 0  0 0 0 0  0 0 0 0  0 0 0 0
                     * 0 0 0 1     0 0 0 0  0 0 0 0  0 0 0 0  0 0 0 1

 2 Min Bias!PileUp   * 0 0 0 0     0 0 0 0  0 0 0 0  0 0 0 0  0 0 0 0
                     * 0 0 1 1     0 0 0 0  0 0 0 0  0 0 0 0  0 0 0 1

 3 Fragment          * 0 0 0 0     0 0 0 0  0 0 0 0  0 0 0 0  0 0 0 0
                     * 0 0 0 1     0 0 0 0  0 0 0 0  0 0 0 0  0 0 1 1

 4 Neutron           * 0 0 0 0     0 0 0 0  0 0 0 0  0 0 0 0  0 0 0 0
                     * 0 0 0 1     0 0 0 0  0 0 0 0  0 0 1 0  0 0 1 1

 5 Fragment+XBsumF   * 0 0 0 0     0 0 0 0  0 0 0 0  0 0 0 0  0 0 0 0
                     * 0 0 0 1     0 0 0 0  0 0 1 0  0 0 0 0  0 0 1 1

 6 Fragment+XBsum    * 0 0 0 0     0 0 0 0  0 0 0 0  0 0 0 0  0 0 0 0
                     * 0 0 0 1     0 0 0 0  0 0 0 0  1 0 0 0  0 0 1 1
```

```
7 Fragment+XBor    * 0 0 0 0    0 0 0 0  0 0 0 0  0 0 0 0  0 0 0 0
                   * 0 0 0 1    0 0 0 0  0 1 0 0  0 0 0 0  0 0 1 1

8 PIX              * 0 0 0 0    0 0 0 0  0 0 0 0  0 0 0 0  0 0 0 0
                   * 0 0 0 1    0 0 0 0  0 0 0 1  0 0 0 0  0 0 0 1
[...]

         MODULE IN SLOT 21:

9 LAND Cosm        * 0 0 0 1    0 0 0 0  0 0 0 0  0 0 0 0  0 0 0 1
                   * 0 0 0 0    0 0 0 0  0 0 0 0  0 1 0 0  0 0 0 0

10 TFW Cosm        * 0 0 0 1    0 0 0 0  0 0 0 0  0 0 0 0  0 0 0 1
                   * 0 0 0 0    0 0 0 0  0 0 0 0  0 0 0 1  0 0 0 0

11 NTF Cosm        * 0 0 0 1    0 0 0 0  0 0 0 0  0 0 0 0  0 0 0 1
                   * 0 0 0 0    0 0 0 0  0 0 0 0  0 0 0 0  0 1 0 0

12 XB Cosm         * 0 0 0 1    0 0 0 0  0 0 0 0  0 0 0 0  0 0 0 1
                   * 0 0 0 0    0 0 0 0  0 1 0 0  0 0 0 0  0 0 0 0

13 XB Sum          * 0 0 0 1    0 0 0 0  0 0 0 0  0 0 0 0  0 0 0 1
                   * 0 0 0 0    0 0 0 0  0 0 0 0  1 0 0 0  0 0 0 0

14 Pixel           * 0 0 0 1    0 0 0 0  0 0 0 0  0 0 0 0  0 0 0 1
                   * 0 0 0 0    0 0 0 0  0 0 0 1  0 0 0 0  0 0 0 0

15 Not-in-use      * 0 0 0 0    0 0 0 0  0 0 0 0  0 0 0 0  0 0 0 0
                   * 0 0 0 0    0 0 0 0  0 0 0 0  0 0 0 0  0 0 0 0

16 Not-in-use      * 0 0 0 0    0 0 0 0  0 0 0 0  0 0 0 0  0 0 0 0
                   * 0 0 0 0    0 0 0 0  0 0 0 0  0 0 0 0  0 0 0 0
```

The rather lengthy listing shown above is an explanation of how trigger conditions sets and with which bit. The first line is the result for an "anticoincidence condition", which is to say that the particular trigger condition did not show up and thus the trigger flag is not set. The second line is the "coincidence condition": the trigger showed up, was not to be downscaled and the bits of the Tpat are set.

The reader may have already noticed that there are more than 16 bits in the words shown

above: the first 4 ones are auxiliary bits and are not recorded in the event structure –they are for the DAQ consumption only, and they would not help in selecting events, as it should be apparent by looking at how they are set through the various conditions.
some of the trigger are also not used during the spill[1] but between the spills and are useful for calibration, because during that time the detectors will see cosmic rays.
To select one or more trigger conditions, a bitmask is applied to the `Tpat` and the match is examined. In the toolkit used for this work, the program that performs this operation is `xb_trigger_siv` and the type of match required can be specified at the command line.

---

[1] The GSI does not provide a continuous beam but the ions are extracted in bunches of a set length in time; the time during which the ions arrive is called "spill".

List of Figures

List of Tables

Bibliography

[6He] Dipole response of the drip-line nuclei ^{6}He and ^{22,24}O, T. Aumann, (not pubblicly available).

[ABKG] Program, computes photon background from "atomic" processes in RHICs, R. Holzmann, H. Scheit.

[Abr12] Measurement of the Neutron Radius of ^{208}Pb through Parity Violation in Electron Scattering, Abrahamyan et. al., DOI: 10.1103/PhysRevLett.108.112502

[Ben89] Single nucleon removal in relativistic nuclear collisions, C. J. Benesh, B. C. Cook and J. P. Vary, DOI: 10.1103/PhysRevC.40.1198

[Ber70] Photoneutron Cross Section for ^{138}Ba and ^{14}Na, B. L. Berman, S. C. Flutz, J. T. Caldwell, M. A. Kelly and S. S. Dietrich, DOI: 10.1103/PyseRevC.2.2318

[Ber85] Relativistic Coulomb Collisions and the Virtual Radiation Spectrum, C.A. Bertulani and G. Baur.

[Bet53] Experimental Nuclear Physics, H. Bethe and J. Ashkin, J. Wiley, 1953, p. 253

[BlEl91] A large area detector for high-energy neutrons, The Land Collaboration, Nuclear Instruments and Methods in Physics Research A314 (1992) 136-154

[BoNg81] Selfconsistent description of the static nuclear dipole polarizability, O. Bohigas, Nguyen van Giai and D. Vautherin, DOI: 10.1016/0370-2693(81)91040-6

[Bor95] Systematiscge Untersuchungen zur Coulombanregung der Zwei-Phononen-Dipolriesenresonanz in ^{208}Pb, K. Boretzky, PhD Thesis.

[Califa] CALIFA, a Dedicated Calorimeter for the R3B/FAIR, D. Cortina-Gil et. al., DOI: 10.1016/j.nds.2014.07.017

[GEANT3.21] GEANT3.21 documentation, public URL: https://web.archive.org/web/20060820150419/ht
[Visible at the Web Archive – The Waybavk Machine].

[Cub98] A large-area scintillating fibre detector for relativistic heavy ions, J. Cub, G. Stengel, A. Grünschloß, K. Boretzky, T. Aumann et. al., DOI: 10.1016/S0168-9002(97)01078-4

[FAIRweb] The FAIR accelerator web page: https://www.gsi.de/en/researchaccelerators/fair.htm

[Gei91] The GSI projectile fragment separator (FRS): a versatile magnetic system for relativistic heavy ions, H. Geissel et. al., [...]

[Gla97] Radiative electron capture by relativistic heavy ions, J. T. Glass, J. F. McCann, D. S. F. Crothers and K. Momberger, DOI: 10.1098/rspa.1997.0022

[Gsi Nachrichten 97] Relativistic Beams of Exotic Nuclei - A Powerful Tool for Nuclear Structure Physics, GSI-Nachrichten 3/1997 (URL: https:www-win.gsi.defrsintroductionsuemmerer_gsinachrichten_3_97_13-e.pdf)

[Hab79] A proposal for a crystal-ball detector system, Lawrence Berkeley Laboratory, 1979.

[HaKr15] Dipole polarizability of ^{120}Sn and nuclear energy density functionals, T. Hashimoto, A. M. Krumbholtz et. al., DOI: 10.1103/PhysRevC.92.031305

[Har01] Giant resonances: fundamental high-frequency modes of nuclear excitation, M. N. Harakeh and A. v. d. Woude, ISBN-10: 0198517355

[Hor01] Neutron Star Structure and the Neutron Radius", C. J. Horowitz and J. Piekarewicz. DOI: 10.1103/PhysRevLett.86.5647

[Hor19] Evolution of the Dipole Response for Neutron-Rich Tin Isotopes ^{124}Sn to ^{132}Sn, to be published.

[IAEAMar07] Nuclear Data Sheets 108,1583 (2007), M. J. Martin, IAEA.

[Jon06] H. Jonasson, The DAQ always runs, Licentiate thesis.

[Kir18] RAINIER: A simulation tool for distributions of excited nuclear states and cascade fluctuations, L. E. Kirsch, L. A. Bernstein, DOI: 10.1016/j.nima.2018.02.096

[KrAk04] Neutron-skin thickness in neutron-rich isotopes, A. Krasznahorkay et. al., Nuclear Physics A731 (2004) 224-234

[Krane87] Introductory Nuclear Physics, K. S. Krane, ISBN-13: 978-0471805533

[Kuh25] Über die Gesamtstärke der von einem Zustande ausgehende Absorptionlinie, W. Kuhn, DOI: 10.1007/BF01328322

[Lat07] Nautron star observations: Prognosis for equation of state constraints, J. M. Lattimer and M. Prakash, DOI: 10.1016/j.physrep.2007.02.003

[Lin13] S. Lindberg, Optimised Use of Detector Systems for Relativistic Radioactive Beams, Master thesis.

[Lin18] S. Lindberg, Exciting Neutron-rich Nuclei, PhD thesis.

[Lip88] Sum rules and giant resonances in nuclei, E. Lipparini and S. Stringari, DOI: 10.1016/0370-1573(89)90029-X

[Mah09] Position reconstruction in large-area scintillating fibre detectors, K. Mahata, H.T. Johansson, S. Paschalis, H. Simon, T. Aumann, DOI: 10.1016/j.nima.2009.07.012

[Met82] The Darmstadt-Heidelberg-Crystal-Ball, V. Metag et. al., Proc. Geiger Memorial Meeting, October 1982.

[Nor90] Electric quadrupole excitations in the interactions of ^{89}Y with relativistic nuclei, J.W. Norbury, DOI: 10.1103/PhysRevC.41.372

[Octave] https://www.gnu.org/software/octave/

[PlagTRK] R. Plag tracker documetation: http://ralfplag.de/tracker/

[R3BRoot] GSI's R3BRoot documentation for the current version found at: https://www.r3broot.gsi.de/documentation

[RaBa05] Coulomb excitation and transfer reaction with rare neutron-rich isotopes, D. C. Radford, C. Baktash et. al., DOI: 10.1016/j.nuclphysa.2005.02.040

[Rei10] Information content of a new observable: The case of the nuclear neutron skin, P.-G. Reinhard and W.Nazarewicz, DOI: 10.1104/PhysRevC.81.051303

[Rei25] Über die Zahl der Disperzionelektronen, die einem stationären Zustande zugeordnet sind, F. Reiche, W. Thomas, DOI: 10.1007/BF01328494

[RM13] Electric dipole polarizability in ^{208}Pb: Insights from the droplet model, X. Roca-Maza, M. Brenna, G. Colò et. al., DOI: 10.1103/PhysRevC.88.024316

[RoBr13] Electric dipole polarizability in ^{208}Pb: Insights from the droplet model, X. Roca-Maza et. al., DOI: 10.1103/PhysRevC.88.024316

[Ros10] D. Rossi, Investigation of the Dipole Response of Nickel Isotopes in the Presence of a High-Frequency Electromagnetic Field, PhD thesis.

[ROOT] Cern's ROOT analysis framework. Documentation for the current version found at: https://root.cern.ch/documentation

[SaUm16] A novel approach to normalize Compton profiles of pure incoherent scatterers, B. M. Sankarshan and T. K. Umesh, DOI: 10.1209/0295-5075/113/27004

[Sch15] P. Schrock, The electric dipole response of 132Sn, PhD thesis.

[Sch17] F. Schindler, Total reaction, charge-changing, and neutron-removal cross sections of the heavy, neutron-rich nuclei 124Sn, 128Sn, 132Sn, and 134Sn measured with large acceptance at R3B, PhD thesis.

[Sor05] Pair production and bremsstrahlung contributions to the stopping of relativistic heavy ions, A. H. Sørensen, DOI: 10.1016/j.nimb.2004.12.009

[Ste05] Isospin asymmetry in nuclei and neutron stars, A. Steiner et. al. DOI: 10.1016/j.physrep.2005.02.004

[Tho25] Über die Zahl der Dispersionelektronen, die einem stationären Zustande zugeordnet sind. (Vorläufige Mitteilung), W. Thomas, DOI: 10.1007/BF01558908

[Sto05] Table of Nuclear Dipole and Electric Quadrupole Moments, N. J. Stone, DOI: 10.1016/j.adt.2005.04.001

[Ton86] Nuclear Matter Saturation Density: From Finite Nuclei to Infinite Matter, F. Tondeur, D. Berdichevsky and M. Farine, Zitshrift für Physik A - Atomic Nuclei 325, 405-413 (1986)

[WaCe12] Nuclear Symmetry Energy and Neutron Skin Thickness, M. Warda et. al. DOI: 10.5506/APhysPolB.43.209

[Wam11] Quasi-Free-Scattering and One-Proton-Removal Reactions with the Proton-Dripline Nucleus ^{1}7Ne at Relativistic Beam Energies, Dr. F. Wamers, PhD Thesis.

[War69] The role of isospin in electromagnetic transitions, E. K. Warburton and J. Weneser, Isospin in Nuclear Physics, D. H. Wilkinson, North-Holland Publishing Company - Amsterdam, 1969

[Wei34] Ausstrahlung bei Stößen sehr schneller Elektronen, C. F. v. Weizsäker, DOI: 10.1007/BF01333110

[Wil34] Feature of the High Energy Particles of Penetrating Radiation and. Status of Ionization and Radiation Formulae, E. J. Williams, DOI: 10.1103/PhysRev.45.729

Acknowledgements

Of course, this thesis and everything that happened during the time I took to do the data analysis and write it down would not have existed without Prof. Dr. Thomas Aumann and Priv-Doz. Dr. Heiko Scheit, whose support and guidance has been awesome and of incomparable value. For this opportunity, trust, support and fundamentally patience while waiting for me to wade through the ocean of atomic background to deliver viable results, my gratitude will always go to them.

Also, a very special thank you to my mentor Dr. Dominic Rossi for the guidance, opinions and tips which have been fundamental to set up this work; and to Prof. Dr. Joachim Enders, who agreed to be the second supervisor for this work.

Many thanks to my colleagues Sonja Stork, Ashton Falduto and Christopher Lehr, who had to put up with me for good three and a half years while I was doing this and, as if that was not enough, they were also so kind to proofread sections of this thesis –a special mention goes to Andrea Horvat, who was patient enough to have endless conversations about every technical aspect of the experiment, much of the theory behind it and also allowed me to not reinvent the wheel when it was not necessary to do so.

Another very special thank you must go to Dr. Dmytro Symochko, who was able to provide the γ-cascades upon which the last part of this work is based and are the foundation to the results achieved. Not only that, but he was also able to deliver the data to me when he had very little time to do so. Legend.

As with every PhD work, what was the main project and thus all I wrote about in this thesis is not all that happened: I was also fortunate enough to work for and at the very first R^{3}B experiments at GSI and RIKEN; this is another aspect of this work for which I am especially grateful to Prof. Dr. Aumann and all the R^{3}B collaboration. Also, in particular, I have been involved with the construction and operation of the NeuLAND detector: thank you very much to Dr. Konstanze Boretzky and Dr. Igor Gasparich for letting me do so. And a big thanks also to Dr. Hans Toshihide Törnqvist for the very lengthy conversations about the superficial and inner workings of the DAQ system.

Last but not least, I'd like to thank my wife Evelyn Schlegl who read through over a hundred and fifty pages of nuclear physics despite having a background in health economics to make sure the language made a minimum amount of sense.

I shall close on a general note: data analysis in physics is easier said than done –and read. What turned in the not exceedingly knotted story above was a lot less linear and a lot less obvious while it was happening and, of course, at no point before ”the number” rolled out the last Octave script it was at all clear that this endeavour would end in a definite result.
This will not come as a surprise to anybody who did scientific research, but may, for some reason, to some reader of this text. But this was the fun of it and also the ultimate reason why some human beings do research. A fact that was brilliantly worded by an awesome mathematician and human being:

“life isn't supposed to be easy”

–Maryam Mirzakhani

Whenever you have the choice, go for the steepest, most tortuous and less marked path you can: you may not arrive quickly, or at all, but it will be worth it.

Academic CV

Name: Lorenzo Zanetti
Address: Oberstr. 5 in 64297 Darmstadt
Date of Birth: 8th of April, 1989
Place of Birth: Milan, Italy
Citizenship: Italian

Schooling

1993-1995	Scuola Materna Statale Italo Calvino - Milano (Kindergarten)
1995-2000	Scuola Elementare Statale Francesco Crispi - Milano (Ground school)
2000-2003	Scuola Media inferiore Statale Quindino di Vona - Milano (Middle school)
2003-2008	Liceo Scientifico Statale Alessandro Volta - Milano (High school)

University

2008-2013	Università Statale di Milano, Bicocca.	Bachelor of Science in Physics.
March 26th, 2013	Bachelor thesis:	Development of a trigger based on the optimum filter in the time domain.
	Supervisor:	Prof. Dr. Oliviero Cremonesi
2013-2016	Università Statale di Milano, Bicocca.	Master's Degree in Particle Physics.
March 22nd, 2016	Master thesis:	The nonlinear behavior of the MKIDs resonators.
	Supervisor:	Prof. Dr. Angelo Nucciotti
Since 2016	PhD student at the Technical University of Darmstadt.	
	Supervisor:	Prof. Dr. Thomas Aumann

Erklärung des Verfassers

Hiermit versichere ich, die vorliegende Dissertation ohne Hilfe Dritter nur mit den angegebenen Quellen und Hilfsmitteln angefertigt zu haben. Alle Stellen, die aus Quellen entnommen wurden, sind als solche kenntlich gemacht. Ich habe bisher noch keinen Promotionsversuch unternommen und diese Arbeit hat in gleicher oder ähnlicher Form noch keiner Prüfungsbehörde vorgelegen.

Darmstadt, 19.11.2019 (Lorenzo Zanetti)